

# **Aging and Direct Recycling of Cathode Active Materials in Commercial Li-ion Cell**

Submitted in partial fulfillment of the requirements for the

degree of

Doctor of Philosophy in

Materials Science and Engineering

Han Wang

B.S., Materials Science and Engineering, Sichuan University

M.S., Materials Science and Engineering, Carnegie Mellon University

Carnegie Mellon University  
Pittsburgh, PA

August, 2020

# Acknowledgements

2020 is a tough year for the people around the world because of the COVID-19. 2020 is also a special year for me because I get my PhD degree and start a new journal in my life. I want to thank everyone I meet in my life who shape me into who I want to be.

I would like to start by expressing my most sincere gratitude to my advisor, Prof Jay Whitacre. The past five years working with you is the most valuable time for me so far. Thank you for coaching me to be a researcher with independent and creative thinking. Thank you for broadening my horizon and deepening my understanding of the battery world. I would not be able to achieve what I have achieved without all your support not just in research but also in life. I deeply appreciate all the effort and time that you spent on me. I would love to keep the mentorship and friendship beyond the graduate study.

I would also like to thank my committee members, Prof Pistorius, Prof Rohrer, and Dr. Pesaran. Thank you all for the time, feedback and guidance on my overview and thesis. I also want to thank my RPE committee members, Prof Salvador and Prof Jayan for suggestions on my research development.

I am very grateful to have all the labmates in Whitacre's group over the five years. Alex, I am so lucky to have you as my first labmate. Thank you for answering my countless "next question" and helping me get familiar with the lab in the first place. Sneha, Jared, Sarah, Sipei, Sven, Katrina, and many others, thank you all for the support on the research and all the entertainment to make my PhD time better.

Lastly, I would like to express my gratitude to my family. To my parents, thank you for providing with the chance to chasing my dream abroad and supporting every decision I have made. Thank you for everything you have done for me. To my girlfriend, thank you for standing with me along the way through PhD to encourage me and to comfort me. Life would be much harder without you.

This work cannot be done without the support from Carnegie Mellon University, Wilton E. Scott Institute and Richard King Mellon Foundation Presidential Fellowship in Energy II.

# Abstract

Recycling of Lithium-ion battery cathode materials has become increasingly important due to the limited amount of resources of raw materials and the environmental and the economic benefit. Recently, a new process, direct recycling, has been gradually developed with less energy and cost input. For this process, the aged cathode materials directly react with a Lithium source under certain thermal process to refunctionalize the aged cathode. The process is also appealing in cases where there is a large amount of similar cathode materials in use, such as electric vehicles.

In reality, Li-ion batteries go through many materials changes as they are charged and discharged. As a result of aging mechanism that can occur under different cycling conditions at different regions of the cell, aged cathode materials can differ in both bulk properties<sup>1</sup>, such as residual Li content level, as well as surface properties, such as solid-state interface (SEI) and surface reconstruction layer. Because these differences exist in aged cathode materials, there is a likely inconsistency of recycled product unless these effects are understood and corrected.

As such, the two primary objectives of this work are:

1. Investigate relationship between the cycling conditions of 18650 Li-ion batteries and the state and consistency of the  $\text{Li}(\text{Ni}_x\text{Co}_y\text{Al}_z)\text{O}_2$  ( $x+y+z=1$ ) (NCA) materials in them after aging.
2. Investigate the relationships between aged NCA materials properties, and recycling processes, and the resulting products.

To achieve the 1<sup>st</sup> objective, commercial 18650 cells were cycled under 4 different conditions.

Full cell cycling data and post-mortem analysis of both electrode materials reveal that aged NCA



materials show different properties after being tested under different cell cycling conditions. Moreover, inhomogeneity in electrode properties was observed and analyzed under certain cell cycling condition. Therefore, the differences in aged NCA materials properties, including the level of residual Li content, SEI thickness, surface reconstruction layer and etc, result from not only the cycling condition of the cell but also the inhomogeneous aging within one cell.

To achieve the 2<sup>nd</sup> objective, solid-state recycling process parameters, including Lithium source, reactants ratio, calcination temperature, calcination time, graphite contamination content and etc, were investigated in order to understand the relationship between the aged NCA materials properties and process parameters. Optimized process steps were created to deal with difference in some of aged NCA materials properties based on the fundamental understanding of the relithiation steps.

# Table of Contents

<b>Acknowledgements.....</b>	<b>II</b>
<b>Abstract.....</b>	<b>IV</b>
<b>Table of Contents.....</b>	<b>VI</b>
<b>Table of Figures.....</b>	<b>XII</b>
<b>Table of Tables.....</b>	<b>XX</b>
<b>Chapter 1. Introduction.....</b>	<b>1</b>
1.1 Motivation .....	1
1.2 Objectives .....	3
1.2.1 Cell and cathode aging part.....	3
1.2.2 Cathode direct recycling part.....	3
<b>Chapter 2. Background.....</b>	<b>4</b>
2.1 Cell aging part .....	4
2.1.1 Lithium ion battery working mechanism.....	4
2.1.2 Lithium ion battery aging mechanism .....	5
2.1.3 Lithium ion battery aging under different cycling conditions.....	8
2.2 Cathode recycling part.....	10
2.2.1 Current Li-ion production and recycling .....	10
2.2.2 Current cathode recycling methods.....	11
2.2.3 Direct recycling reaction type.....	16
2.2.4 Reaction parameters effect in solid-state reaction.....	17
2.2.5 Properties of aged cathode active material related to recycling.....	19

<b>Chapter 3. Experimental.....</b>	<b>22</b>
3.1 Overview .....	22
3.2 Aged cell and electrode materials acquired .....	22
3.2.1 Cell Aging Methodology .....	22
3.2.2 Aged electrodes acquirement .....	23
3.3 Cathode active materials recycling process .....	24
3.3.1 Solid-state method .....	24
3.3.2 Hydrothermal process .....	24
3.4 Physical property characterization.....	25
3.4.1 X-ray Diffraction (XRD) .....	25
3.4.2 Scanning Electron Microscopy (SEM) .....	25
3.4.3 X-ray Photoelectron Spectroscopy (XPS) .....	25
3.4.4 Thermal Gravimetric Analysis (TGA) .....	26
3.5 Electrochemical performance characterization .....	26
3.5.1 Fabrication of cathode .....	26
3.5.2 Coin cell assembly.....	26
3.5.3 Galvanostatic Cycling with Potential Limit (GCPL) .....	27
3.5.4 Cyclic Voltammetry (CV) .....	27
<b>Chapter 4. Capacity Degradation in Commercial Li-ion Battery Cells: The</b>	
<b>Effects of Charge Protocol and Temperature.....</b>	<b>28</b>
4.1 Overview .....	28
4.2 Experimental.....	29
4.2.1 Reference cycles .....	29

4.2.2 Electrochemical Impedance Spectroscopy (EIS) .....	29
4.2.3 Anode Morphology Characterization.....	31
4.2.4 Chemical Composition Characterization.....	31
4.3 Result .....	31
4.3.1 18650 cells cycling and aging .....	31
4.3.2 Electrochemical characterization of harvested electrodes .....	36
4.3.3 Morphology and surface chemistry characterization of harvested anode.....	37
4.4 Discussion.....	39
4.5 Conclusion .....	44
<b>Chapter 5. Aging level and inhomogeneity of cathode linked to 18650</b>	
<b>Li-ion cell in long-term cycling .....</b>	<b>46</b>
5.1 Overview .....	46
5.2 Experimental.....	47
5.3 Result .....	47
5.4 Discussion.....	55
5.4.1 Cathode aging in full cell under different cycling conditions .....	55
5.4.2 Inhomogeneity in cathode aging in full cell .....	59
5.5 Conclusion.....	63
<b>Chapter 6. Towards Practical Application of Direct Relithiation of Aged</b>	
<b>Cathode: Effect of Process Variables and Contaminant .....</b>	<b>65</b>
6.1 Overview .....	65
6.2 Experimental .....	66

6.2.1 Direct recycling process via solid-state method.....	66
6.2.2 Sample Naming .....	67
6.2.3 Characterization.....	68
6.3 Result.....	68
6.4 Discussion.....	75
6.4.1 Effect of lithium source.....	75
6.4.2 Effect of graphite content .....	76
6.4.3 Effect of molar ratio of aged cathode active materials to Lithium source.....	78
6.5 Conclusion.....	80
<b>Chapter 7. Effect of properties of aged cathode active materials on recycled product .....</b>	<b>82</b>
7.1 Overview .....	82
7.2 Experimental .....	83
7.2.1 Preparation of materials .....	83
7.2.2 Recycling of prepared NCA materials.....	85
7.2.3 Characterization of materials.....	86
7.3 Result and discussion.....	88
7.3.1 Preparation of materials for recycling .....	88
7.3.2 Effect of difference in SoC.....	90
7.3.3 Effect of surface reconstruction layer .....	97
7.3.4 Effect of SEI.....	100
7.4 Conclusion.....	102

## **Chapter 8. Direct Recycling of Aged LiMn<sub>2</sub>O<sub>4</sub> Cathode Materials used**

<b>in Aqueous Lithium-ion Batteries: Processes and Sensitivities .....</b>	<b>104</b>
8.1 Overview .....	104
8.2 Experimental .....	105
8.2.1 Collecting of aged LMO and fresh LMO.....	105
8.2.2 Creating aged LMO with different SoC.....	106
8.2.3 Recycling of aged LMO through solid-state reaction method.....	106
8.2.4 Recycling of aged LMO through hydrothermal reaction method.....	107
8.2.5 Materials property characterization.....	107
8.2.6 Electrochemical characterization.....	107
8.3 Result .....	107
8.3.1 TGA.....	108
8.3.2 SEM.....	109
8.3.3 XRD.....	109
8.3.4 Electrochemical Results.....	110
8.4 Discussion .....	114
8.4.1 Comparison between solid-state method and hydrothermal method.....	119
8.4.2 Results from the solid-state reaction method.....	119
8.4.3 Results from hydrothermal reaction method.....	121
8.4.4 Aged LMO with different SoC .....	122
8.5 Conclusion.....	123
<b>Chapter 9. and Future Work .....</b>	<b>126</b>

<b>Disclaimer .....</b>	<b>128</b>
<b>References .....</b>	<b>130</b>

# Table of Figures

**Figure 2-1.** Working mechanism of Li-ion battery during charge and discharge. **(Page 5)**

**Figure 2-2.** SEI composition on the anode surface. **(Page 6)**

**Figure 2-3.** Overview on basic ageing mechanisms of cathode materials. **(Page 7)**

**Figure 2-4.** A schematic of the proposed parasitic side reactions occurring in a full cell and in a pouch bag only containing charged positive electrode and electrolyte. **(Page 8)**

**Figure 2-5.** Schematic of constant current and constant voltage charge. **(Page 9)**

**Figure 2-6.** Schematic of pyrometallurgical recycling process. **(Page 12)**

**Figure 2-7.** Process of preparation for hydrometallurgical recycling. **(Page 13)**

**Figure 2-8.** Process of synthesis of precursors of cathode from hydrometallurgical recycling. **(Page 14)**

**Figure 2-9.** Process of direct recycling. **(Page 15)**

**Figure 2-10.** TGA of NCA cathode at different SOC. **(Page 19)**

**Figure 2-11.** SEM and HREM images of sample F1 (a, c) and W2 (b, d) after storing in air for 30 days. **(Page 20)**

**Figure 2-12.** Schematic of SEI on NCM active materials surface. **(Page 21)**

**Figure 4-1.** Schematic of how the hybrid cells were prepared from the 18650 batteries in order to separately collect EIS data of the anode and cathode of the 18650 batteries. **(Page 30)**

**Figure 4-2.** The data for 18650 battery cells cycling under four different conditions. (a) Long-term cycling data of the 18650 cells. (b) Charge-discharge cycles at 25 °C with a 2 A current in between 2.5 V and 4.2 V after finishing 1000 cycles (c) Discharge curves of the reference cycle with 0.02 C rate at 25 °C for the cells after finishing 1000 cycles under different conditions. **(Page 32)**



**Figure 4-3.** Long-term cycling data of the 18650 cells under CC and CCCV conditions at both 25°C and 60°C. The current at CC step is 1A. **(Page 33)**

**Figure 4-4.** The black line is for the [CC, 25 °C] 18650 cell; the red line is for the [CC, 60 °C] 18650 cell; the green line is for the (CC-CV, 25 °C) 18650 cell and the blue line is for the (CC-CV, 60 °C) 18650 cell. “Stage 1” and “Stage 2” are labeled for the convenience of result discussion. (a) Average voltage during charge process with IR correction, (b) Energy efficiency, (c) Coulombic efficiency, and (d) IR resistance VS cycle number. **(Page 35)**

**Figure 4-5.** (a) EIS of the graphite/Li coin cell with the anodes extracted from either a pristine 18650 cell, the [CC, 25 °C] cell or the [CC, 60 °C] cell. (b) EIS of the NCA/Li coin cell with the cathodes extracted from either a pristine 18650 cell, the [CC, 25 °C] cell or the [CC, 25 °C] cell. **(Page 36)**

**Figure 4-6.** SEM and FIB cross sectional images of the anode extracted from (a)(d)(g) a pristine cell, (b)(e)(h) the [CC, 60 °C] cell after 1000 cycles, (c)(f)(i) the [CC, 25 °C] cell after 1000 cycles. (g), (h) and (i) are zoomed-in image at surface of (d), (e) and (f) respectively. **(Page 37)**

**Figure 4-7.** (a) FT-IR of the anode and (b) XPS C 1s spectra of the anode extracted from a pristine cell, the [CC, 60 °C] cell and the [CC, 25 °C] cell. **(Page 39)**

**Figure 4-8.** A schematic of the proposed formation of the SEI on the anode surface in 18650 batteries at 25 °C and 60 °C under CC charge condition. This figure is modified based on the figure from the reference. **(Page 42)**

**Figure 5-1.** In-situ thermal measurement of 18650 cell during long-term cycling. **(Page 47)**

**Figure 5-2.** 18650 cell long-term cycling performance under different conditions with repeat. For CC charge step, 2A current was used with 4.2V voltage cut-off. For CV step, the voltage was

held at 4.2V with a current cut-off at 59mA. For discharge step, 2A current was used with 2.5V voltage cut-off. **(Page 48)**

**Figure 5-3.** (a) Schematic diagram of the electrode extracting process and naming of electrode based on location; image of cathode and anode extracted from pristine cell (b,g), [CC, 25°C] cell (c,h), [CC, 60°C] cell (d,i), [CCCV, 25°C] cell (e,j) and [CCCV, 60°C] cell (f,k) after 1000 cycles. **(Page 49)**

**Figure 5-4.** Images of cathode and anode extracted from [CC, 25°C] cell (a,e) after 1000 cycles. The yellow rectangles indicate the location for SEM images. SEM image of the cathode (b-d) and the anode (f-h) under different magnification. The yellow circle indicate the locations where the SEM images with higher magnification are done. **(Page 50)**

**Figure 5-5.** The SEM image of cathode (a-d) and of anode (f-h) extracted from pristine 18650 cell and [CC, 60°C], [CCCV, 25°C] and [CCCV, 60°C] cells after 1000 cycles. **(Page 51)**

**Figure 5-6.** FIB image of cathode from (a) pristine cell, (b) [CC, 25°C] cell and (c) [CCCV, 60°C] cell after 1000 cycles. **(Page 51)**

**Figure 5-7.** (a) X-ray diffraction pattern comparison between cathode extracted from pristine, CC, 25°C], [CC, 60°C], [CCCV, 25°C] and [CCCV, 60°C] cells after 1000 cycles. (b-c) Zoomed-in peak (003) and (104) from (a). The blue dots indicate peaks of Si for calibration. **(Page 52)**

**Figure 5-8.** XPS O 1s spectra of the cathode from pristine, [CC, 60°C], [CCCV, 25°C] and [CCCV, 60°C] cells and [CC, 25°C] cell at both the side and center after 1000 cycles. **(Page 53)**

**Figure 5-9.** The reference cycle of re-fabricated cathode from different 18650 cells after long-term cycling. For reference cycle, the coin cell is cycled at 0.1C rate for both charge and discharge with 2.5 V and 4.2 V voltage cut-off. For each sample, 3 coin cells were made (shown by different color). For each cell, 3 reference cycles were done (a). cathode from pristine cell; (b)

cathode at side location from [CC, 25°C] cell; (c) cathode at center location from [CC, 25°C] cell; (d) cathode from [CC, 60°C] cell; (e) cathode from [CCCV, 25°C] cell and (f) cathode from [CCCV, 60°C] cell. **(Page 54)**

**Figure 5-10.** The reference cycle of anode extracted from different 18650 cells after cycling. For reference cycle, the coin cell is cycled at 0.1C rate for both charge and discharge with 0.01V and 1.5 V voltage cut-off. **(Page 56)**

**Figure 5-11.** EIS of cathode extracted from 18650 cells after 3 reference cycles in coin cell. **(Page 57)**

**Figure 5-12.** Temperature difference of [CC, 25°C] cell between center and positive/negative points along with the corresponding voltage profile during cycling. **(Page 60)**

**Figure 5-13.** Cross sectional schematic of inhomogeneous aging in the electrodes from [CC, 25°C] cell. The figure on the left shows the growth of the secondary layer on the anode surface in different stages while the figure on the right shows the pressure changes in both direction and size suggested by the arrows. The Y-axes is along the radial direction and the Z-axes is along the axial direction. The arrow of the pressure is along the Y-axes. Stage 1 is before the long-term cycling, stage 2 is during long-term cycling and stage 3 is after long-term cycling. **(Page 62)**

**Figure 6-1.** XRD patterns of (a) fresh NCA, (b) aged NCA, (c-d) R-NCA after 1<sup>st</sup> and 2<sup>nd</sup> calcination, (e-f) R-NCA\_Li<sub>2</sub>CO<sub>3</sub> after after 1<sup>st</sup> and 2<sup>nd</sup> calcination. The black dash lines stand for peaks location of Li<sub>2</sub>CO<sub>3</sub> and the orange dash lines stand for peaks location of Li<sub>4</sub>AlO<sub>5</sub>. **(Page 69)**

**Figure 6-2.** XRD patterns of (a-b) R-NCA\_3% graphite after 1<sup>st</sup> and 2<sup>nd</sup> calcination and (c-d) R-NCA\_6% graphite after 1<sup>st</sup> and 2<sup>nd</sup> calcination. The black dash lines stand for peaks location of Li<sub>2</sub>CO<sub>3</sub> and the orange dash lines stand for peaks location of Li<sub>4</sub>AlO<sub>5</sub>. **(Page 70)**

**Figure 6-3.** XRD patterns of (a-b) R-NCA\_0.5:1 ratio after 1<sup>st</sup> and 2<sup>nd</sup> calcination, (c-d) R-NCA\_2:1 ratio after 1<sup>st</sup> and 2<sup>nd</sup> calcination and (e-f) R-NCA\_3:1 ratio after 1<sup>st</sup> and 2<sup>nd</sup> calcination. The black dash lines stand for peaks location of Li<sub>2</sub>CO<sub>3</sub> and the orange dash lines stand for peaks location of Li<sub>4</sub>AlO<sub>5</sub>. **(Page 71)**

**Figure 6-4.** XPS spectra of O 1s, F 1s and Ni 2p for (a) fresh cathode, (b) aged cathode, (c) R-NCA, (d) R-NCA\_Li<sub>2</sub>CO<sub>3</sub>, (e) R-NCA\_3% graphite, (f) R-NCA\_6% graphite, (g) R-NCA\_3:1 ratio, (h) R-NCA\_2:1 ratio and (i) R-NCA\_0.5:1 ratio. In O 1s spectra, the red dashed and dot lines sit on 530.67 eV and 528.31 eV separately. In F 1s spectra, the blue dashed and dot lines sit on 687.71 eV and 684.74 eV separately. In Ni 2p spectra, the green line sits on 855.42 eV. The etch time per step is 40s. **(Page 73)**

**Figure 6-5.** Comparison of the reference cycle of (a) fresh cathode, (b) aged cathode, (c) R-NCA, (d) R-NCA\_Li<sub>2</sub>CO<sub>3</sub>, (e) R-NCA\_3% graphite, (f) R-NCA\_6% graphite, (h) R-NCA\_0.5:1 ratio, (h) R-NCA\_3:1 ratio and (i) R-NCA\_2:1 ratio. For reference cycle, the coin cell is cycled at 0.1C rate for both charge and discharge with 2.5 V and 4.2 V voltage cut-off. **(Page 74)**

**Figure 7-1.** XRD of NCA<sub>P</sub> and chemically delithated NCA materials, NCA<sub>HSOC</sub> and NCA<sub>LSOC</sub>. (003) and (104) peaks from NCA materials are suggested. The blue dot is for Silicon (111) peak location which is used as reference point. **(Page 88)**

**Figure 7-2.** XRD of NCA<sub>P</sub> (black) and R-NCA<sub>HSOC</sub> (blue) and R-NCA<sub>LSOC</sub> (red) after 1<sup>st</sup> and 2<sup>nd</sup> sinter treatment. (003) and (104) peaks from NCA materials are suggested. The blue dot is for Silicon (111) peak location which is used as the reference position for all the samples. **(Page 89)**

**Figure 7-3.** TGA of NCA<sub>HSOC</sub>, NCA<sub>LSOC</sub>, and NCA<sub>P</sub> with LiOH with 1:1 molar ratio from 120 °C to 700°C with heating rate 5 °C/min under O<sub>2</sub> flow. The mass after holding at 120°C for 20min is

used as 1 for mass ratio calculation. During the holding step, the  $\text{H}_2\text{O}$  in  $\text{LiOH}\cdot\text{H}_2\text{O}$  is gone.

**(Page 89)**

**Figure 7-4.** Mass differential curve with respect to temperature for samples ( $\text{NCA}_{\text{HSoC}}$ ,  $\text{NCA}_{\text{LSoC}}$  and  $\text{NCA}_{\text{HSoC}}$  with  $\text{LiOH}\cdot\text{H}_2\text{O}$  with 1 to 1 molar ratio) from 120 °C to 500 °C. The heating rate is 5 °C/min. **(Page 91)**

**Figure 7-5.** XPS O1s and C1s spectrums of samples, (a-b)  $\text{NCA}_{\text{HSoC}}$ , (c-d,g-h)  $\text{R-NCA}_{\text{HSoC}}$ , with/without wash step after 2<sup>nd</sup> sinter process and (e-f, i-j)  $\text{R-NCA}_{\text{LSoC}}$  with/without wash step after 2<sup>nd</sup> sinter process. The black line is recorded data. The blue dashed lines are peaks deconvolution. The red line is for simulated peaks based on deconvoluted peaks. **(Page 94)**

**Figure 7-6.** TEM image of  $\text{R-NCA}_{\text{LSoC}}$  without(b) wash step after 2<sup>nd</sup> sinter process. **(Page 95)**

**Figure 7-7.** Electrochemical test of 4 samples in coin cells,  $\text{R-NCA}_{\text{HSoC}}$  with/without wash step after 2<sup>nd</sup> sinter process and  $\text{R-NCA}_{\text{LSoC}}$  with/without wash step after 2<sup>nd</sup> sinter process. For each sample, three coin cells were tested, indicated by three colors. For each coin cell, it was cycled in between 2.5V and 4.2V with a 0.2c rate for 4 cycles. **(Page 96)**

**Figure 7-8.** XRD of samples (a)  $\text{NCA}_{\text{HSoC}_350\text{oC}}$ ,  $\text{R-NCA}_{\text{HSoC}_350\text{oC}}$  with different 2<sup>nd</sup> sinter time (12h and 24h) and (b)  $\text{NCA}_{\text{HSoC}_650\text{oC}}$ ,  $\text{R-NCA}_{\text{HSoC}_650\text{oC}}$  with different 2<sup>nd</sup> sinter time (12h and 24h). **(Page 99)**

**Figure 7-9.** Electrochemical test of 6 samples in coin cells,  $\text{NCA}_{\text{HSoC}_350\text{oC}}$ ,  $\text{R-NCA}_{\text{HSoC}_350\text{oC}}$  with different 2<sup>nd</sup> sinter time (12h and 24h) and (b)  $\text{NCA}_{\text{HSoC}_650\text{oC}}$ ,  $\text{R-NCA}_{\text{HSoC}_650\text{oC}}$  with different 2<sup>nd</sup> sinter time (12h and 24h). For each sample, three coin cells were tested, indicated by three colors. For each coin cell, it was cycled in between 2.5V and 4.2V with a 0.2c rate for 4 cycles. **(Page 100)**

**Figure 7-10.** XPS O1s, P2p and F1s spectrums of NCA<sub>HSoC\_electrolyte\_14d</sub> (a, c, e) and R-NCA<sub>HSoC\_electrolyte\_14d</sub> (b, d, f). The black line is recorded data. The blue dashed lines are peaks deconvolution. The red line is for simulated peaks based on deconvoluted peaks. **(Page 101)**

**Figure 7-11.** Electrochemical test of 2 samples in coin cells, NCA<sub>HSoC\_electrolyte\_14d</sub> (a) and R-NCA<sub>HSoC\_electrolyte\_14d</sub> (b). For each sample, three coin cells were tested, indicated by three colors. For each coin cell, it was cycled in between 2.5V and 4.2V with 0.2c rate for 4 cycles. **(Page 102)**

**Figure 8-1.** SEM images of a) aged LMO, b) LMO-SS recycled from aged Li<sub>0.7</sub>Mn<sub>2</sub>O<sub>4</sub> with washing in between two-step of heat treatments, c) LMO-HT(1:1, 165°C, 24hr) recycled from aged Li<sub>0.7</sub>Mn<sub>2</sub>O<sub>4</sub>, d) LMO-HT(10:1, 165°C, 24hr) recycled from aged Li<sub>0.7</sub>Mn<sub>2</sub>O<sub>4</sub>. **(Page 110)**

**Figure 8-2.** X-ray diffraction patterns of a) fresh LMO, b) aged LMO, c) aged Li<sub>0.7</sub>Mn<sub>2</sub>O<sub>4</sub>, d) aged Li<sub>0.5</sub>Mn<sub>2</sub>O<sub>4</sub> and e) aged Li<sub>0.3</sub>Mn<sub>2</sub>O<sub>4</sub>. **(Page 111)**

**Figure 8-3.** X-ray diffraction patterns of a) fresh LMO, b) LMO-SS recycled from aged Li<sub>0.3</sub>Mn<sub>2</sub>O<sub>4</sub> without washing between two steps of heat-treatments, LMO-SS recycled with washing between two steps of heat-treatments from c) aged LMO, d) aged Li<sub>0.7</sub>Mn<sub>2</sub>O<sub>4</sub> and e) aged Li<sub>0.3</sub>Mn<sub>2</sub>O<sub>4</sub>. **(Page 112)**

**Figure 8-4.** X-ray diffraction patterns of a) fresh LMO, b) LMO-HT(1:1, 165°C, 24hrs) recycled from aged Li<sub>0.7</sub>Mn<sub>2</sub>O<sub>4</sub>, c) LMO-HT(1:1, 165°C, 24hrs) recycled from aged Li<sub>0.3</sub>Mn<sub>2</sub>O<sub>4</sub>. **(Page 122)**

**Figure 8-5.** X-ray diffraction patterns of a) LMO-HT recycled from aged Li<sub>0.7</sub>Mn<sub>2</sub>O<sub>4</sub> through different hydrothermal recycling conditions, b) and c) simulation of impure peaks for LMO-HT samples in (a). Small blue dots are originally data points and solid lines are simulation line. ▲ and ● indicate impure peaks. **(Page 113)**

**Figure 8-6.** OCV of fresh LMO and aged LMO with different SoC using electrochemical titration. The black dot is OCV point. **(Page 114)**

**Figure 8-7.** OCV of fresh LMO and intermediate product of LMO-SS from aged LMO with different SoC. The black dot is OCV point. **(Page 115)**

**Figure 8-8.** Cyclic voltammetry comparison between fresh LMO, aged LMO, intermediate product and final recycled product LMO-SS with washing between two steps of heat-treatments from a) aged  $\text{Li}_{0.3}\text{Mn}_2\text{O}_4$ , b) aged  $\text{Li}_{0.7}\text{Mn}_2\text{O}_4$ , c) aged  $\text{LiMn}_2\text{O}_4$ , d) aged  $\text{Li}_{0.3}\text{Mn}_2\text{O}_4$  without the wash in between two steps of heat-treatments. **(Page 116)**

**Figure 8-9.** Cyclic voltammetry comparison between fresh LMO, aged LMO and LMO-HT(1:1, 165°C, 24hrs) from a) aged  $\text{Li}_{0.7}\text{Mn}_2\text{O}_4$  and b) aged  $\text{Li}_{0.3}\text{Mn}_2\text{O}_4$ . **(Page 117)**

**Figure 8-10.** Comparison of a) cathode charge-discharge curve of 2<sup>nd</sup> cycle with +0.24 V to +0.57 V at a C/6 rate and b) discharge capacity vs cycle number for the first 10 cycles of fresh LMO, aged LMO, LMO-SS with washing in between two steps of heat-treatments from aged  $\text{Li}_{0.7}\text{Mn}_2\text{O}_4$  and LMO-HT(1:1, 165°C, 24hr) from aged  $\text{Li}_{0.7}\text{Mn}_2\text{O}_4$ . **(Page 118)**

# Table of Tables

**Table 3-1.** Cell Test Condition and Naming. (**Page 23**)

**Table 4-1.** Atomic% at Anode Surface by EDX from Different Cells. (**Page 39**)

**Table 5-1.** Equivalent circuit model and impedance parameters based on the model. (**Page 57**)

**Table 6-1.** Calculated value for c-axis based on the Si peak correction. (**Page 72**)

**Table 7-1.** Naming of samples in this chapter. (**Page 84**)

**Table 7-2.** Calculation of lattice parameter c. (**Page 90**)

**Table 8-1.** Outline for Sample Name. (**Page 105**)

**Table 8-2.** Mass Ratio of LMO Active Materials in Products. (**Page 109**)

**Table 8-3.** Second oxidation peak intensity ratio in CV of LMO-HT to fresh LMO. (**Page 118**)



# Chapter 1. Introduction

## 1.1 Motivation

Major economies like US, EU, China are investing heavily in electrifying the automotive industry. The adoption of electric vehicles has created a huge demand for lithium-ion battery cells, and the forecasted annual production of lithium-ion battery in 2020 is 40 GWh, which translates to over  $2 \times 10^5$  tonnes of cathode materials per year.<sup>2-3</sup> Lithium-ion batteries contain high-value and energy-intensive cathode active materials including nickel and cobalt, which makes them valuable for recycling from both economic benefit and energy-saving point of views. Also, Lithium-ion batteries contain organic electrolytes, which contaminate the environment if not properly dealt with.<sup>4</sup> From resource, energy, and environment aspects, it is necessary to recycle used Lithium-ion batteries, especially the cathode materials.

The current two dominant cathode recycling approaches are based on pyrometallurgical and hydrometallurgical processes.<sup>5-6</sup> The former method suffers from large energy input and low yield of recycling in term of mass while the latter method suffers from heavy usage of solvent and complex wet-chemistry processes, making the recycled product based on these processes less environmental-friendly and economically competitive.<sup>7</sup> To overcome the drawback of current industrial recycling processes, researchers have started to explore recycling cathode active materials through a direct recycling process.<sup>8-12</sup> The idea of the direct recycling process is to directly treat aged cathode materials with a Lithium source under certain reaction conditions, such as solid-state reaction or hydrothermal reaction, to regain the lost capacity of aged cathode active materials. The main goal is to avoid the costly breakdown and subsequent reproduction of

cathode active materials so that the initial energy embodied during the production of cathode materials can be saved. Compared with current industrial recycling processes, the advantages of this approach are<sup>8</sup>: [1] it could save overall processing energy by avoiding higher temperature to break down and then re-use the elemental constituents of the cathode active materials. [2] The initial embodied energy of the cathode active materials is preserved. [3] It avoids complex chemical processes and caustic chemicals if done using some of the more appealing process pathways.

However, there are still gaps between conceptual demonstration and practical application of this process and we think one of the keys to success lies in understanding and overcoming the variance in the aged cathode active materials. In the real world, aged batteries go through different types of usage conditions before they are retired. The different types of usage conditions will result in differences in aging mechanisms inside the batteries, resulting in inhomogeneous properties of the aged cathode materials.<sup>13-15</sup> The difference in the properties of cathode materials, including lithium content,<sup>16</sup> solid-electrolyte interface (SEI) <sup>17-19</sup> phase thermal stability,<sup>20-23</sup> and etc, impact on how the aged cathode active materials reacts with lithium sources during any direct recycling process, therefore affecting the electrochemical performance of directly recycled product.

As such, it is necessary to investigate the relationship among the usage conditions of the cell, properties of aged cathode materials and the process parameters of the direct recycling, from perspectives of materials science, electrochemistry, and battery engineering. The result would

give a guidance to how to deal with differently aged cathode active materials and how to get the directly recycled product with consistent quality in the real work application.

## 1.2 Objectives

### 1.2.1 Cell and cathode aging

- Investigate the relationship between the commonly used cycling conditions and aging models of the full cell
- Investigate the relationship between the commonly used cycling conditions and properties of aged cathode materials

### 1.2.2 Cathode active materials direct recycling

- Investigate the effect of solid-state recycling method parameters on recycled cathode materials
- Investigate the effect of hydrothermal recycling parameters on recycled cathode materials
- Investigate the effect of differences in aged cathode properties on recycled cathode materials

# Chapter 2. Background

## 2.1 Cell aging

### 2.1.1 Lithium-ion battery function

Lithium-ion batteries are devices that store and convert electrical energy and chemical energy. They are composed of five parts: anode, cathode, separator, electrolyte, and electric circuit, as shown in Figure 2-1. The separator acts as a physical barrier to prevent electron transfer inside the battery. The electrolyte, which is normally composed of organic solvent with lithium-ion salt dissolved in, such as  $\text{LiPF}_6$ . The electrolyte is ionically conductive but electronically insulating. The electric path is composed of current collector and external wires, which enables electrons to move between anode and cathode through an external circuit. The anode is commonly composed of graphite (electrochemical active materials), binder and conductive fillers, such as carbon black, and the cathode is commonly composed of lithium-contained ceramic oxide (electrochemical active materials), such as  $\text{LiCoO}_2$ ,  $\text{LiMnO}_2$ ,  $\text{LiFePO}_4$ , and  $\text{LiNi}_x\text{Co}_y\text{Al}_z\text{O}_2$  ( $x+y+z=1$ ), binder and conductive fillers. During discharge, the thermodynamic driving force causes the  $\text{Li}^+$  to move from anode to cathode through internal of the battery via electrolyte while the electrons move along the external circuit from anode to cathode. The electron and  $\text{Li}^+$  from anode meet at cathode in the end. During the charge process, the movement of both electron and  $\text{Li}^+$  is reversed.

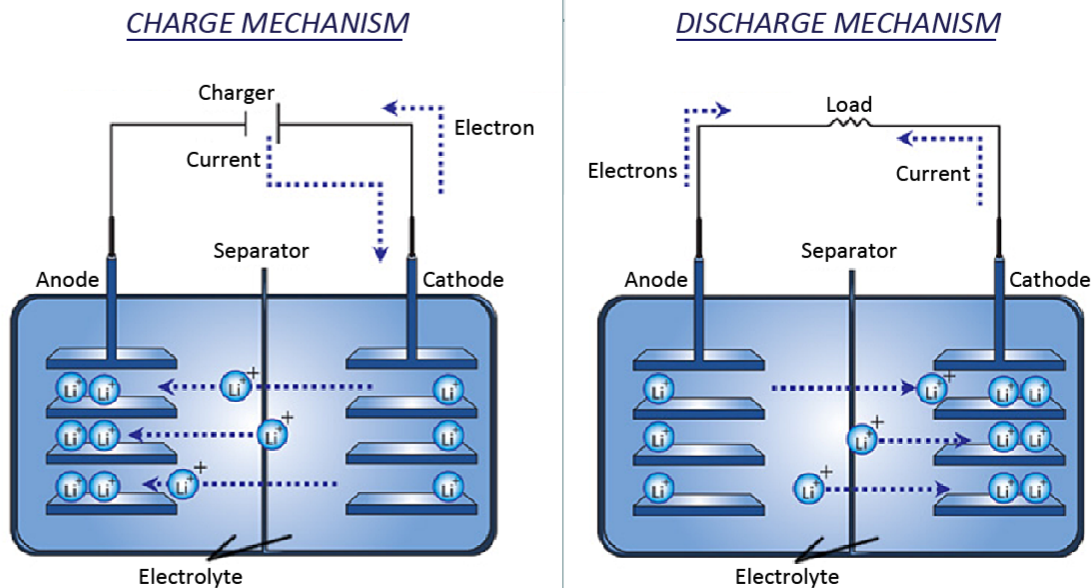


**Figure 2-1.** Working mechanism of Li-ion battery during charge and discharge.<sup>24</sup>

### 2.1.2 Lithium-ion battery aging mechanism

The aging mechanisms of Li-ion batteries have been summarized in a number of review papers.<sup>25-26</sup> Historically, the observed effects of aging are attributed to and/or associated with primarily one part of the battery, such as the cathode, anode, separator and, current collector.

#### 2.1.2.1 Anode

For the anode (graphite), the main aging mechanism are the growth of SEI(solid-electrolyte interface) and Li plating.<sup>25, 27</sup> Standard non-aqueous electrolyte Lithium-ion batteries operate across a voltage range that, at times, surpasses the thermodynamic stability limit of the organic solvents used in the electrolyte. This results in various species decomposing and coating the surface of the electrodes, a process commonly called SEI formation. The composition of the SEI depends on the cell conditions, such as the electrolyte composition and the electrochemical parameters used in the first formation cycle of the battery. An example is shown in Figure 2-2.<sup>28</sup>

The accumulation of SEI correlates to an irreversible capacity loss for the battery for two

reasons: (1) lithium ions are consumed during SEI formation and (2) electrode pores are blocked, creating a less porous and more resistive path for lithium ion transport.<sup>29-30</sup>

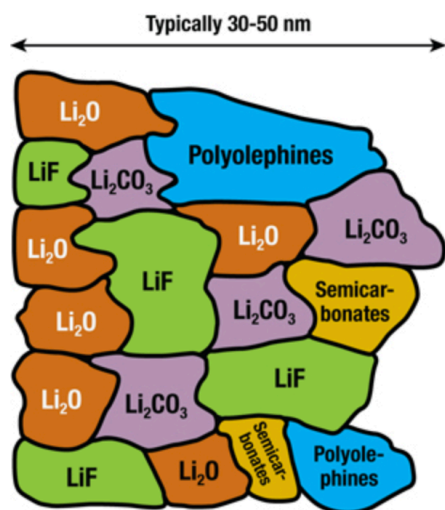


**Figure 2-2.** SEI composition on the anode surface.<sup>28</sup>

As for Li plating, thermodynamically the insertion voltage of lithium ions for graphite anode is less negative ( $\sim 100$  mV) than the Li plating voltage. However, under certain circumstances, kinetic driving forces dominate, creating Li plating on the anode surface. There are several cycling factors that could lead to Li plating in the cell: increasing charge rate, decreasing temperature and increasing SoC (state of charge) of cell.<sup>31-33</sup> SoC means level of charge of an electric battery relative to its capacity. Based on the previous publications regarding Li plating, it is more likely to happen at a temperature lower than room temperature<sup>15</sup> or, more often, lower than  $0^\circ\text{C}$ .<sup>15,34</sup> It is also more likely to happen at C rate higher than 1C. (C rate is defined as the discharge current divided by the theoretical current draw under which the battery would deliver its nominal rated capacity in one hour. A 2C discharge rate would deliver the battery's rated capacity in 0.5 hour)<sup>35-36</sup>

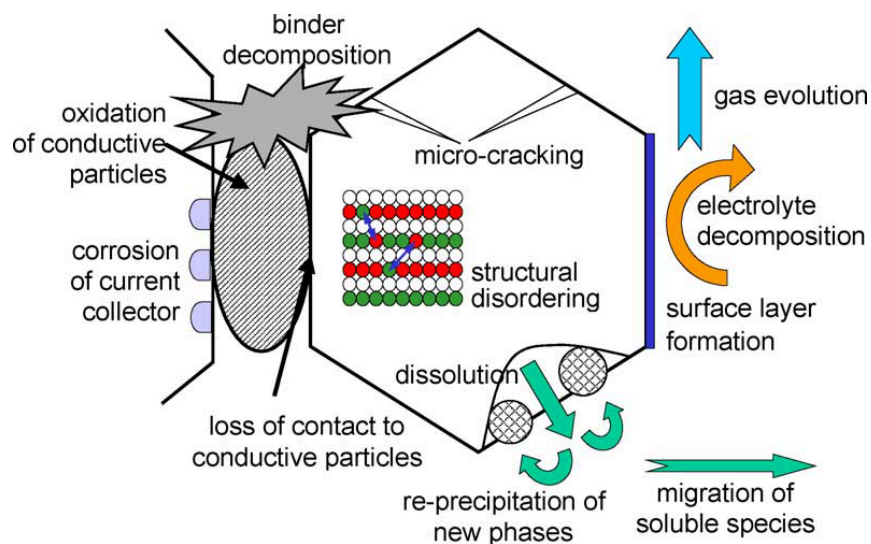


**Figure 2-3.** Overview on basic ageing mechanisms of cathode materials.<sup>30</sup>

### 2.1.2.2 Cathode

For the cathode, the aging mechanisms are illustrated in Figure 2-3,<sup>30</sup> which can be divided into two categories: electrochemically inactive component and active materials. For inactive component, binder decomposition and corrosion of current collector cause increasing impedance, leading to capacity loss of cathode. For electrochemical active materials, structural disordering, surface reconstruction, metal dissolution, and SEI formation can lead to capacity loss of cathode. These effects do not occur separately and cannot be discussed independently from each other. The dominant aging mechanism is decided by cathode composition and cycling/storage conditions.

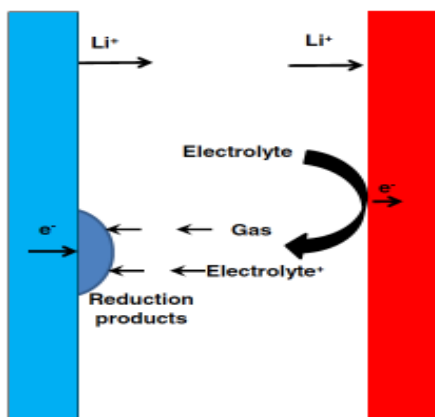


**Figure 2-4.** A schematic of the proposed parasitic side reactions occurring in a full cell and in a pouch bag only containing charged positive electrode and electrolyte. The negative electrode in the pouch cell schematic (left side) is colored blue, while the positive electrode in the pouch cell and pouch bag schematics is colored red.<sup>37</sup>

#### 2.1.2.3 Anode/cathode interaction

More recently published evidence shows that interaction or “crosstalk” between the anode and cathode as mediated by the electrolyte exists in full Li-ion batteries, as shown in Figure 2-4 and that these complex interactions result in a significant negative impact on the long-term performance of Li-ion batteries.<sup>37-49</sup> This anode/cathode interaction can be divided into categories including (1) the dissolution of metal ions from the cathode that migrate to the anode surface, catalyzing SEI formation on the anode<sup>38, 42, 46-48</sup>, and (2) electrolyte decomposition products generated at the largely delithiated cathode/electrolyte interface that diffuse/migrate to the anode surface, which can also result in precipitate/SEI formation.<sup>37, 39, 41, 43-44</sup> Some reports suggest that these interactions are accelerated by high voltages at the cathode/electrolyte interface and are also strongly influenced by the temperature of the battery.<sup>37-38, 40</sup>

#### 2.1.3 Lithium-ion battery aging under different cycling conditions



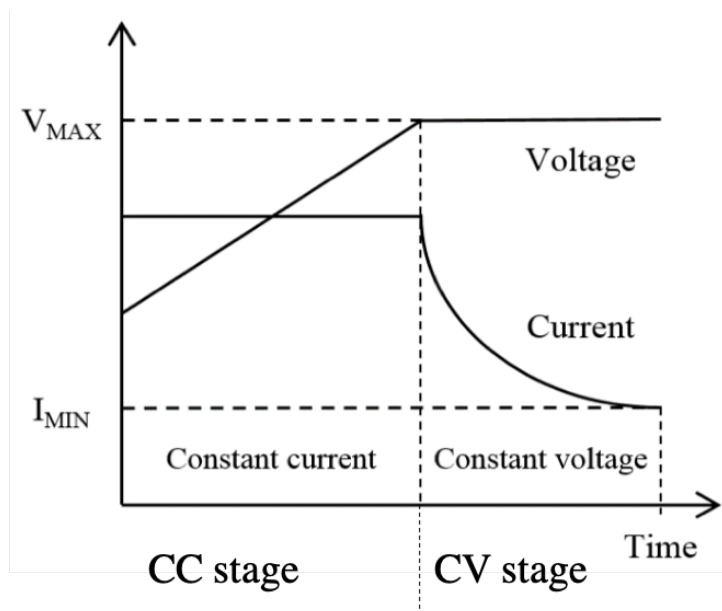


**Figure 2-5.** Schematic of constant current and constant voltage charge. The image is modified based on the source from <https://www.ti.com/lit/ds/symlink/bq2057.pdf>.

Charge protocol affects the time-average voltage experienced at the cathode, therefore it affects the aged cathode properties at the end of cycling.<sup>13-15</sup> For constant current charge protocol, the constant current is applied to the battery until the voltage cut-off is reached (Figure 2-5). For constant voltage protocol, the battery is held at a certain voltage while the charge current gradually decreases (Figure 2-5). The constant current (CC) (or the closely related constant power) charge protocol is used in different applications, for example in electric vehicles where charging on the order of 2 hours or less is desired, or in general when a constant potential current taper (current drop while the voltage remains) can't be carried out for time reasons. In some cases, a higher specific current is used, which results in a larger polarization experienced at the cathode. Because of electrode polarization effects, the time-averaged voltage experienced by the cathode material during the charging process can be higher. The increasing time-averaged voltage on the cathode structure would then lead to more electrolyte decomposition at the

cathode/electrolyte interface. In the constant current and constant voltage (CC-CV) charge protocol, which is more commonly used in cases where there is ample time to completely charge cells, a dwell at a maximum specified potential is maintained while the current is allowed to decrease through a current taper. During this process, electrode polarization will decrease as a result of the decreasing current. It is also commonly observed that higher temperatures ( $>25\text{ }^{\circ}\text{C}$ ) induce faster electrolyte decomposition at the electrode/electrolyte interface or in the bulk electrolyte due to thermally enhanced reaction kinetics.<sup>37-38</sup>

## 2.2 Cathode Recycling

### 2.2.1 Current Li-ion production and recycling

As the global market for lithium-ion batteries expands to further service electric vehicles and stationary energy storage installations, the demand for functional ceramic oxide cathode materials used in these batteries increases. Meanwhile, the present usage of raw materials for producing these cathode materials is not proven to be sustainable, while up to 95% of the cathode materials from aged lithium-ion batteries have been disposed in landfills instead of being recycled.<sup>50</sup> Some materials used are also relatively scarce: cobalt is used in most cathodes in the commercial lithium-ion batteries, and Sverdrup's model has predicted that cobalt raw materials will run out after some time in the next century, while spot price has increased several hundred percent from 2010.<sup>51</sup> Furthermore, Life cycle analysis (LCA) has revealed that<sup>52</sup> “materials production” was the main contributor to  $\text{CO}_2$  emission and energy costs when making cathode material; a significant amount of energy is utilized for mining scarce materials and high-temperature process required for making cathode materials. To obtain 1 ton of lithium, we need to handle 250 tons of mineral or 750 tons of brine compared with 28 tons of used batteries. A

report from Argonne National Lab<sup>4</sup> shows the recycling of automotive Li-ion batteries to supply materials is a long-term strategy. The benefit that the recycling would provide, includes moderating virgin material prices, reducing costs and other impacts of disposal, reducing reliance on imported materials, and reduced energy use and emissions in EV battery production. These benefits would emerge after 15-20 years from now. However, it is necessary to prepare the technology path before the market comes.

### 2.2.2 Current cathode recycling methods

The industrial recycling processes typically used to recycle cathode materials can be divided into the hydrometallurgical process and the pyrometallurgical process. As briefly discussed in chapter 1, each has advantages including the type of element being recycled and adaptability to elemental variation.<sup>5</sup> However, the two methods are considered to be complex and energy-consuming due to their breakdown-and-repurposing approach.<sup>6-7</sup> Also, the price of cathode materials recycled from current industrial recycling processes is not economically competitive with cathodes produced from raw materials. Thus, the development of the direct recycling process development is necessary. Currently, the development of direct recycling process is at pilot scale.



### 2.2.2.2 Hydrometallurgical recycling process

The flowsheet of the general preparation process for the hydrometallurgical recycling is shown in Figure 2-7.<sup>53</sup> The purpose of the preparation process is to separate electrode active powders from current collectors and other parts of the battery. After the cathode is collected, the cathode is leached using the acid solution. Then, the metal ions can precipitate out in form of salt when changing the pH of the solution and the product would be the metal salt, as suggested by Figure 2-8.<sup>54</sup> The formed precursor can then be calcinated to produce recycled cathode. The advantage of this recycling process is that the purity of the recycled product is high and is less energy-intensive than pyrometallurgical recycling process since no high temperature melting down process is required. However, the problem is that the process requires a lot of chemicals, such as acid, solvent for leaching, separation, and precipitation. Because of them, this process brings a lot of secondary contaminations to the environment.

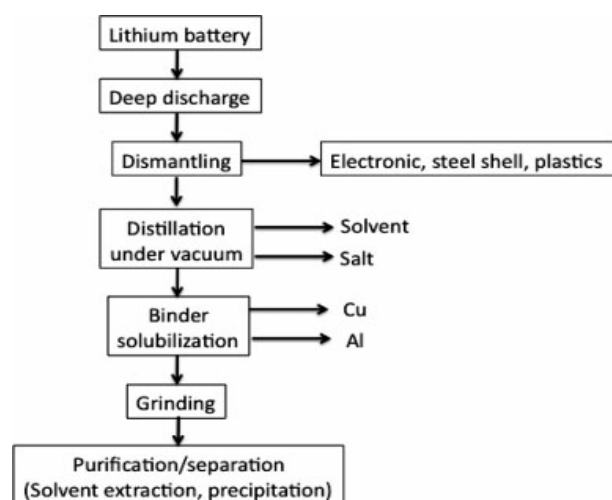


**Figure 2-7.** Process of preparation for hydrometallurgical recycling.<sup>53</sup>

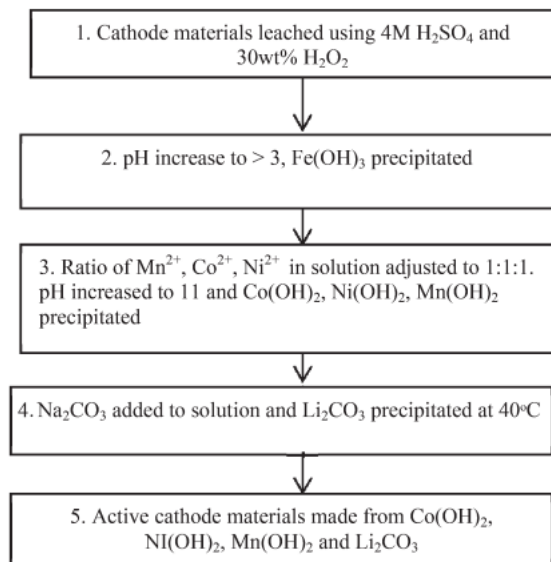


**Figure 2-8.** Process of precipitation of metal ions from hydrometallurgical recycling.<sup>54</sup>

### 2.2.2.3 Direct recycling method

The general process of direct recycling is shown in Figure 2-9. The preparation process before cathode powder collecting is similar to the hydrometallurgical recycling process. After that, the aged cathode powder goes through relithiation process by reacting with lithium sources, such as LiOH or Li<sub>2</sub>CO<sub>3</sub>. The key difference between the above-mentioned recycling processes and the direct recycling process is that instead of recycling basic elements as with pyrometallurgical process or recycling compounds as with hydrometallurgical process from the cathode materials, direct recycling process enables us to retain the structure of the cathode materials while regenerating the cathode materials by reacting them directly with the lithium source. By doing so, the initial energy that is embodied in the cathode materials can be saved and chemicals,

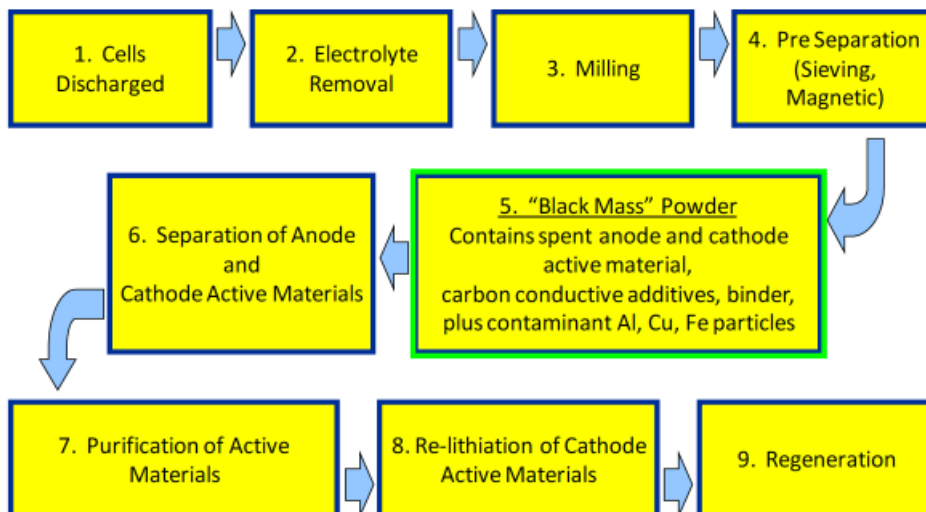


**Figure 2-9.** Process of direct recycling. Image retrieved from <http://www.farasis.com/>.

solvent, and high-temperature melting-down treatment can be avoided. The viability of direct recycling has been proved. Ganter et al. demonstrated refunctionalization of  $\text{LiFePO}_4$  (LFP) from commercial cells, that were cycled to an end-of-life state, by chemical lithiation process.<sup>8</sup> Aged LFP electrode was added into lithium iodide (LiI) solution for 20 hours. The recycled LFP regained the original capacity of 150--155 mAh/g. They also demonstrated that the  $\text{LiFePO}_4$  refunctionalization process through chemical lithiation, decreased the embodied energy by 50% compared to cathode production from virgin materials.<sup>8</sup> Kim et al. designed a single synthetic step using hydrothermal method in a concentrated LiOH solution at 200°C where aged LCO electrode including active materials LCO, carbon black, binder and Al current collector were all put into autoclave without any scraping procedures.<sup>17</sup> Although the renovated electrode materials had some electrochemically inactive impurities, the renovated  $\text{LiCoO}_2$  phase exhibited the first discharge capacity of 144.0 mAh/g and the discharge capacity retention of 92.2% after 40 cycles.<sup>55</sup> Yang Shi et al showed by using two steps of relithiation processes, aged  $\text{Li}_x\text{Ni}_{0.5}\text{Mn}_{0.3}\text{Co}_{0.2}\text{O}_2$  (NMC) is relithiated and return to its full capacity as fresh NMC.

Hydrothermal and solid-state process were used as the first relithiation process in two papers following by the second annealing process at high temperature.

### 2.2.3 Direct Recycling Reaction Type

For direct recycling reaction, there are generally two steps. The first step is to relithiate the aged cathode active materials, which means putting  $\text{Li}^+$  back into the structure and obtaining a stoichiometry similar to fresh cathode active materials. This step is necessary for two aspects reasons. Firstly, it provides the Li source needed for the aged cathode active materials to regain capacity. Secondly, the phase stability of cathode active materials normally decreases with a lower level of lithium in the structure. So the  $\text{Li}^+$  that is put into the structure during the first step helps stabilize the phase during the second calcination process. The second step is to treat the aged cathode active material at high temperature (700~800 °C) to increase the crystallinity.

#### 2.2.3.1 Solid-state reaction

The solid-state reaction is a very common method for preparation of solids from the mixture of solid materials through high-temperature treatment. To have better solid-solid interaction, mixtures are normally mechanically milled to have uniform mixing and contact before sintering. To form a new phase, atoms in one phase need to move out to accommodate with atoms from the other phase, which will take lots of energy. Also, the diffusion coefficient for atoms in solid is low compared with that in liquids and gases. High temperature is necessary to overcome these two problems. However, the solid-state reaction usually results in large particle size and impurity in the product, which is due to agglomeration of particle and improper mixing process at high temperature. In our case, the solid-state reaction is between aged cathode active materials and



lithium source. The problem with the solid-state reaction used in the first step is that the temperature is normally above 300°C to activate the relithiation reaction. But at this temperature, the phase change reaction or decomposition reaction of cathode active materials already starts, resulting in the less pure product in the end.

#### 2.2.3.2 Hydrothermal reaction

The term hydrothermal synthesis refers to any heterogeneous reaction in the presence of aqueous solvents or mineralizers under high pressure and temperature conditions to dissolve and recrystallize materials that are relatively insoluble under ordinary conditions. The hydrothermal reaction can be applied during the first relithiation process since activation energy for relithiation during the hydrothermal reaction is lower compared with solid-state reaction, therefore reducing the side reactions, such as cathode active materials decomposition.

#### 2.2.4 Reaction parameters effect in solid-state reaction

To deal with the large amount of aged cathode materials, a continuous process is of the essence when it comes to large-scale application. Hydrothermal reaction, though having less side reactions, can be only be processed from batch to batch, which lowers the rate of production. In contrast, the solid-state reaction can be processed continuously. Moreover, the current production line of cathode active materials, such as  $\text{LiNi}_x\text{Co}_y\text{Al}_z\text{O}_2$  (NCA) and  $\text{LiNi}_x\text{Co}_y\text{Mn}_z\text{O}_2$  (NCM), is based on solid-state reaction so that the current production line is more compatible with solid-state approach than hydrothermal one. The above-mentioned two reasons explain why we are going to focus on solid-state enabled recycling process mainly. For solid-state reaction, there are couple of factors in the process should be considered.

Firstly, a typical lithium source, such as  $\text{Li}_2\text{CO}_3$  or  $\text{LiOH}$ , is mixed with aged cathode materials during relithiation process. The cost of the Lithium source is a major contributor to the total of cost of recycled cathode product. In the recent years, the price of  $\text{Li}_2\text{CO}_3$  get closer and still lower than  $\text{LiOH}$ , mainly due to the large production of NCM based cathode. The current price  $\text{Li}_2\text{CO}_3$  and  $\text{LiOH}$  are 7.25\$/kg and 9.5 \$/kg, as of July 12, 2020. Using  $\text{Li}_2\text{CO}_3$  as the lithium source would greatly reduce cost when compared to  $\text{LiOH}$  because  $\text{LiOH}$  is more sensitive to air and has high requirement of process equipment. Moreover, the minimum amount of lithium source needed to fully recycle aged cathode materials per kg is also important to reduce the cost.

Secondly, one of the major obstacles that are faced by recycling of aged cathode materials is the separation of anode powder from cathode powder during the powder collection process. Currently, there are four types of separation methods,<sup>56-57</sup> including thermal method (burning), physical separation method (solvent separation), chemical method (acid etching) and physicochemical method (froth flotation). The chemical method involves a dissolution of cathode materials in corrosive acids leaving anode particles. The end product of chemical method can't be further used for the direct recycled process. For other three methods, the cathode powder is left and can be further processed using the relithiation reaction. However, the best separation efficiency is around 90% at pilot scale and increasing the efficiency is still hard. So, it may be not be cost-effective to separate cathode to anode powder completely at a large scale. Therefore, it is necessary to investigate what would be the effect of weight percentage of the anode (graphite commonly) in collected cathode powder on the recycled cathode performance.

## 2.2.5 Properties of aged cathode active material related to recycling

The properties of aged cathode active materials are closely related to how to directly recycle them and the recycled product performance. Here, we are going to talk about 3 specific properties that are relatively more important.

### 2.2.5.1 level of lithiation

During battery cycling, the proportion of cyclable lithium-ions gradually decreases due to the formation of SEI on both anode and cathode. So at the end of cycling, Lithium content in aged cathode active materials, such as  $\text{Li}_a(\text{Ni}_x\text{Co}_y\text{Al}_z)\text{O}_2$  ( $0 < a < 1$ ,  $x+y+z$  is close to 1), is less than the stoichiometry of fresh cathode,  $\text{Li}(\text{Ni}_x\text{Co}_y\text{Al}_z)\text{O}_2$  ( $x+y+z = 1$ ). For cathode active materials, it is the general trend that the thermal stability of cathode active materials decreased with less Li content, as shown in Figure 2-10,<sup>58</sup> which means the decomposition reaction during relithiation process is closely related to the level of lithiation. Therefore, the end product of the relithiation process is greatly affected by the level of lithiation of reactants.

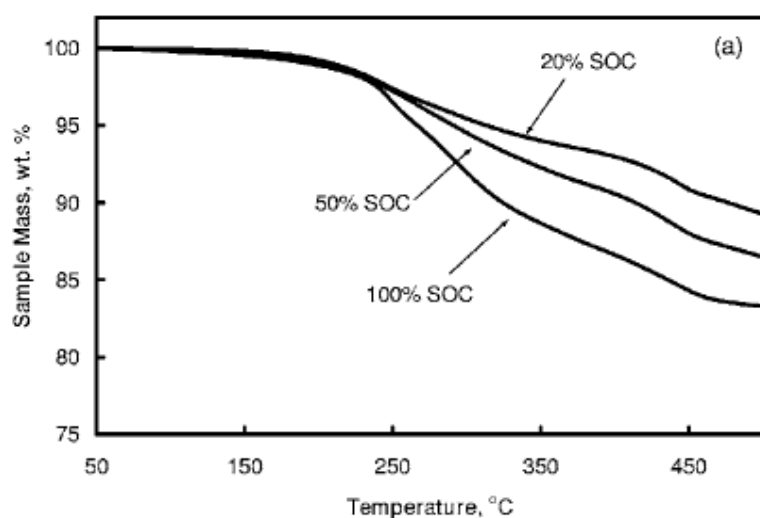


**Figure 2-10.** TGA of NCA cathode at different SOC<sup>58</sup>

### 2.2.5.2 Reconstructed surface layer

The crystal structure of the cathode surface layer also affects the recycled product. Layered-structure cathode materials, such as  $\text{Li}(\text{Ni}_x\text{Co}_y\text{Al}_z)\text{O}_2$  and  $\text{Li}(\text{Ni}_x\text{Co}_y\text{Mn}_z)\text{O}_2$  materials, experience the change of crystal structure into rock salt structure on the surface layer during cycling.<sup>20-23</sup> As shown in Figure 2-11 d,<sup>19</sup> the FFT pattern shows that after cycling, the surface layer, which sits in between the out-most amorphous layer and bulk structure, has a different structure from the bulk structure. This layer is electrochemical resistant and causes decreased capacity. During recycling, the reaction to change rock salt structure back into layer structure is not a thermodynamically favorable reaction.<sup>59</sup> Therefore, the surface layer with the rock salt structure would have an effect on the final recycled product.

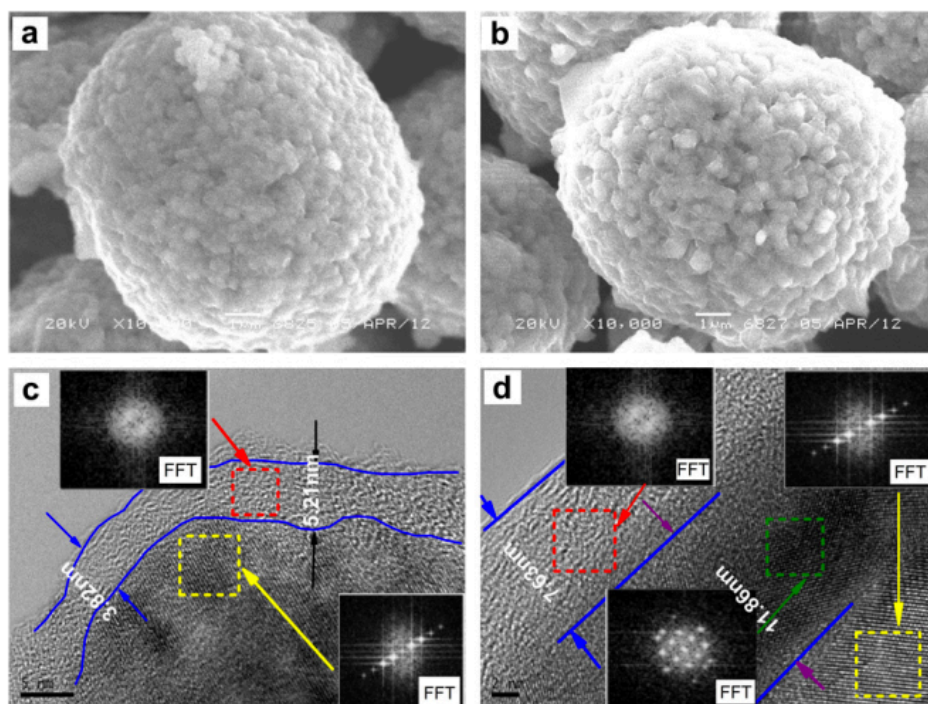


**Figure 2-11.** SEM and HREM images of sample F1 (a, c) and W2 (b, d) after storing in air for 30 days.<sup>19</sup>

### 2.2.5.3 SEI at cathode/electrolyte interface

SEI on the cathode particle surface is another factor that could affect the recycled product. The SEI is formed when the cathode is exposed to electrolyte during cycling. The SEI is attached to the surface of the particle so firmly that some of it is still seen on the particle surface via TEM even after intense washing process of cathode<sup>17-19</sup>, as shown in Figure 2-11 (c). The exact composition of SEI is still under debate and varies based on the chemistry of cathode active materials. For NCM cathode, the composition of SEI is shown in Figure 2-12.<sup>60</sup> The SEI left on the surface of aged cathode particle could influence the contact between lithium source reactant and aged cathode active materials during the recycling process, which leads to different recycling reaction efficiency. Also, the SEI layer is electrochemical resistant and would decrease capacity if not dealt with during the recycling process.

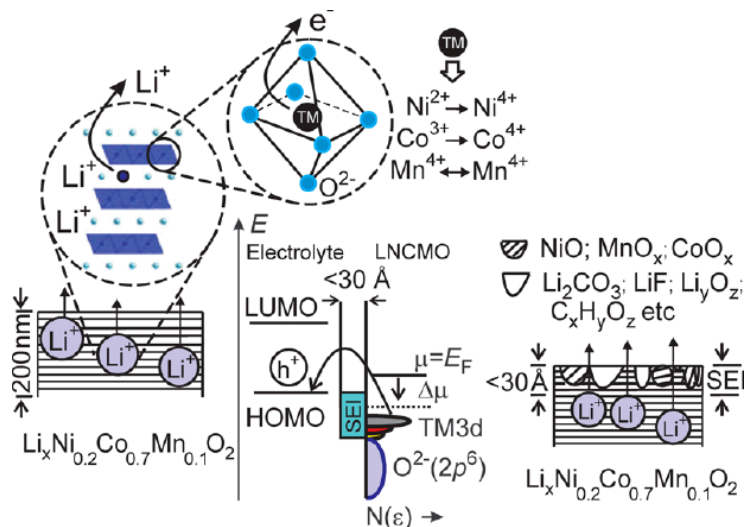


**Figure 2-12.** Schematic of SEI on NCM active materials surface<sup>60</sup>

# Chapter 3. Experimental Methods

## 3.1 Overview

This chapter gives a brief overview of the general way of acquiring the aged Li-ion cell and aged cathode active materials, the relithiation process via the solid-state method and the hydrothermal method. Furthermore, a brief overview of characterization techniques used in our study will be given. Physical properties are determined by characterization techniques such as X-ray Diffraction (XRD), Scanning Electron Microscopy (SEM), X-ray Photoelectron Spectroscopy (XPS), and Thermal Gravimetric Analysis (TGA). The electrochemical functionalities of materials are characterized by electrochemical methods such as Cyclic Voltammetry (CV), Galvanostatic Cycling with Potential Limits (GCPL) and Electrochemical Impedance Spectroscopy (EIS). The general electrode preparation process for the electrochemical test will also be given. The experimental method for work presented in subsequent chapters was as described in this chapter, unless indicated otherwise.

## 3.2 Aged cell and electrode materials acquired

### 3.2.1 Cell Aging Methodology

All the 18650 cells used in the document were Panasonic NCR 18650A cells unless otherwise mentioned. The cathode was  $\text{LiNi}_x\text{Co}_y\text{Al}_z\text{O}_2$  and the anode was graphite materials. According to the manufacturing specification of the cell, the typical capacity is 3070 mAh and the suggested charge temperature range is 0-45°C. The tests were conducted on a Land Battery System CT2001A. The cells were tested as described in the matrix offered in Table 1.

<b>Table 3-1. Cell Test Condition and Naming</b>		
<b>Cycling Protocol</b>	<b>Cycling Temperature</b>	
	25 °C	60 °C
Charge: constant-current Discharge: constant current	CC, 25 °C	CC, 60 °C
Charge: constant-current and constant-voltage Discharge: constant current	CC-CV, 25 °C	CC-CV, 60 °C

The cycling conditions of the CC charge protocol were a 2 A current (around 0.64 C rate based on a nominal capacity of the cell) for the charge and discharge processes with a 2.5 V to 4.2 V voltage cut-off. The cycling conditions of the CC-CV charge protocol were (1) a 2 A constant charge current to 4.2 V, followed by (2) a 4.2 V constant voltage step with a 59 mA current cut-off and (3) a discharge current of 2 A with a 2.5 V cut-off. There was no rest step between charge and discharge for both cycling protocols. The batteries were cycled 1000 times, with a total test time of approximately 1 to 3 months. Although cells would likely be replaced when losing more than 20% of initial capacity in practical application, we elected to continue cycling even after losing 20% capacity in order to more completely age the electrodes. There were at least four cells tested under each cycling condition to verify repeatability.

### 3.2.2 Aged electrodes acquirement

After the 18650 cells finished 1000 cycles, the cells were fully discharged with 50mA current to 2.5V before the tear-down process. The cells were then transferred into glove-box for tear-down. The tear-down was done carefully to avoid the internal shorting, especially during shell opening. During the tear-down process, a tube cutter was first used to cut the caps on both ends off and then Dremel was used to cut the shell along the edge. After tear-down, both cathode and anode were collected and manually rinsed with Diethyl carbonate (DEC) for 5 min to get rid of

electrolyte. Then both electrodes were stored in glove-box for further analysis. The more detailed preparation process of anode and cathode will be given in the corresponding chapters.

### 3.3 Cathode active materials recycling process

#### 3.3.1 Solid-state approach

Generally, the solid-state relithiation process was composed of two calcination steps. Before the first calcination, aged cathode powder was mixed with a lithium source with a certain ratio using mortar & pestle for 20 min. The mass for the mixture powder was around 200 mg. Then under O<sub>2</sub> flow with flow rate 60 sccm, the mixture was heated at 480°C for 3h with the rate of 10°C/min for heat-up and cool-down. After the first calcination step, the mixture was taken out and re-mixed using mortar & pestle for 20 min. Then under O<sub>2</sub> flow rate 60 sccm, the mixture was heated at 730°C for 12h with the rate of 10°C/min for heat-up and cool-down. Other process parameters, including reactant type and reactant ratio, will be described in corresponding chapters.

#### 3.3.2 Hydrothermal approach

The mass of aged cathode materials used was around 400mg. The mass of Lithium source was weighted out based on the reactant ratio. In short, a lithium source was added into 50 mL DI water and stirred for 30 min for full dissolution. Then aged cathode materials were added the solution and were stirred for 1 hour. The solution mixture was then transferred into a Teflon-lined stainless-steel autoclave. The autoclave was sealed and heated at a certain temperature for a certain time. After the reaction was finished, the product was washed with DI water for 3 times and dried at 80°C under vacuum overnight.



### 3.4 Physical property characterization

#### 3.4.1 X-ray diffraction (XRD)

XRD is generally used for the analysis of structure and level of lithiation of cathode active materials. The to-be-tested powder was mixed with 10 wt% Si polycrystalline powder (99% purity) using mortar & pestle for 10min. Then X-ray diffraction (XRD) patterns of samples were characterized on a PANalytical X'pert diffractometer with a Cu K $\alpha$  radiation with a scan range from 15—70° 2 $\theta$ . The result is further corrected by using Si (111) peak at 28.44° as reference.

#### 3.4.2 Scanning Electron Microscopy(SEM) & Energy Dispersive X-ray Spectroscopy (EDS)

SEM is generally used for morphology. EDS is used for surface layer composition analysis. FIB is used for cross-section image. Platinum sputtering coating was conducted before imaging samples to improve conductivity on the sample surface, which could help avoid surface charging. The thickness of Platinum coating is around 1 nm. The images were taken via Philips XL30 Scanning Electron Microscope with acceleration voltage 10kV and spot size 4 in secondary electron imaging mode. Oxford instruments INCA Electron/Wave Dispersion Spectroscopy (EDS) was also employed to detect elements composition of the samples. The cross-section images were prepared by a focused ion beam (FIB) milling process using a gallium source on an FEI NOVA 600.

#### 3.4.3 X-ray Photoelectron Spectroscopy (XPS)

XPS is generally used for surface chemistry analysis. XPS was performed using an ESCALAB 250Xi X-ray photoelectron spectrometer microprobe, with a 650  $\mu$ m spot size. The X-ray source

was Al K $\alpha$ , which provided photons with 1486.6eV energy. For the etching step, the voltage was 3000kV.

#### 3.4.4 Thermal Gravimetric Analysis (TGA)

TGA is generally used for calculation of cathode active materials mass% and thermal stability of aged cathode materials. Thermo-gravimetric (TG) analysis was carried out on SDT Q600. The mass of samples was around 10 mg for consistency. The procedure was: jump to 120°C, hold for 30 minutes, increase temperature to 750°C with a rate of 10°C/min. The gas flow rate 100 mL/min and the gas was air or N<sub>2</sub>.

### 3.5 Electrochemical performance characterization

#### 3.5.1 Fabrication of cathode

The general cathode fabrication process was as described here unless otherwise mentioned. The cathode active materials, carbon black and Polyvinylidene fluoride (PVDF) powder were weighed with a weight ratio of 9:0.5:0.5 and N-methyl-2-pyrrolidone (NMP) was gradually added to make black slurry. Then the black slurry was screened onto Al foil using a doctor blade and the aluminum foil was transferred into a vacuum oven at 80 °C overnight.

#### 3.5.2 Coin cell assembly

The coin cell assembly process mentioned here is generally for organic-solvent-based system test. For aqueous system, it will be mentioned in detail in the corresponding chapter.

The fabricated cathode described above was punched by puncher with 11 mm diameter and weighted, therefore the mass of cathode active materials could be calculated. The punched

cathode was then paired with Li foil in the 2032 coin cell. The Celgard battery separator and commercial electrolyte (1 M LiPF<sub>6</sub> in 1:1 ethylene carbonate (EC): diethyl carbonate (DEC)) from Sigma were used. Spacer with 0.5mm thickness and wave spring purchased from MTI Corporation were used.

### 3.5.3 Galvanostatic Cycling with Potential Limit (GCPL)

GCPL test involves the study of the potential of the electrode in response to a constant current applied to it. When the potential of the electrode hits the cut-off value, the direction of current is switched. For example, for NCA electrode, we used 2.5V and 4.2V as cut-off voltages when testing a NCA cathode paired with Li chip in the coin cell. GCPL test was commonly used for measurement of the electrochemical capacity of active materials.

### 3.5.4 Cyclic Voltammetry (CV)

CV test involves a type of potentiodynamic electrochemical measurement. The system applies current to the electrode and monitors the voltage of the working electrode with very rapid feedback loop to obtain preset potential sweep rate, when the potential reaches a certain value the current would be inverted. The current at the working electrode is recorded versus voltage.

Three-electrode set-up was used in CV test, including working electrode (electrochemical active materials), reference electrode (Hg/Hg<sub>2</sub>SO<sub>4</sub>) and counter electrode (Pt wire). In this study, CV test was used mostly in the aqueous system and is used for electrochemical capacity and rate capability test. The detailed set-up parameter is described in the corresponding chapter.

# Chapter 4. Capacity Degradation in Commercial Li-ion Battery Cells: The Effects of Charge Protocol and Temperature

## 4.1 Overview

In this chapter, we are going to analyze the long-term cycling data and post-mortem analysis results, which were collected from commercial 18650 Li-ion cells using the potential-limited CC and CC-CV charge protocols at 25 °C and 60 °C. The electrochemical analysis of the full cells under different cycling conditions was performed to explore how the cycling conditions influenced battery performance, especially CC step at 25°C. Further, anode morphology and chemical composition were analyzed to investigate a potential formation mechanism of the thick secondary SEI on the surface. Based on the hypothesis of the thick secondary SEI formation, we propose a theory to explain why the battery with CC charge protocols faded faster at 25 °C than at 60 °C.

### Hypotheses:

- When 18650 cells are cycled at 25°C, the CV step during charge process cause formation of secondary SEI on the anode surface
- When 18650 cells are charged using just CC step, the chemistry and electrochemical resistance of the SEI formed on anode surface is different when cycled under 25 °C and 60 °C.

## 4.2 Experimental

### 4.2.1 Reference cycles

Reference cycle tests for 18650 cell used small current during charge and discharge process to keep the deviation from equilibrium state small so that the real remaining capacity of the system could be measured. The cycling protocol was a 50 mA (1/60 C rate) constant current for both charge and discharge with a 2.5 V and 4.2 V voltage cut-off. It was performed at 25 °C for all batteries after they completed 1000 cycles. The naming of the samples follows the Table 3-1.

### 4.2.2 Electrochemical Impedence Spectroscopy (EIS)

EIS was performed using a Bio-logic 16-channel VMP-3 multi-channel potentiostat/electrochemical impedance spectrometer. All tests were performed at 25 °C. For the EIS of the 18650 cells, measurements were taken after the reference cycle test, when the cells were fully discharged and had rested for 3 hours. The data was collected between 50 kHz and 1 mHz by applying a 20 mA sinusoidal current perturbation. EIS was also performed on the anode and cathode materials in separate coin cells. A schematic of the coin cell preparation is shown in Figure 4-1. Disassembly of the 18650 cells to retrieve the anode/cathode materials and assembly of the coin cells from them was done in a glove-box under Argon gas. To test the graphite anode,

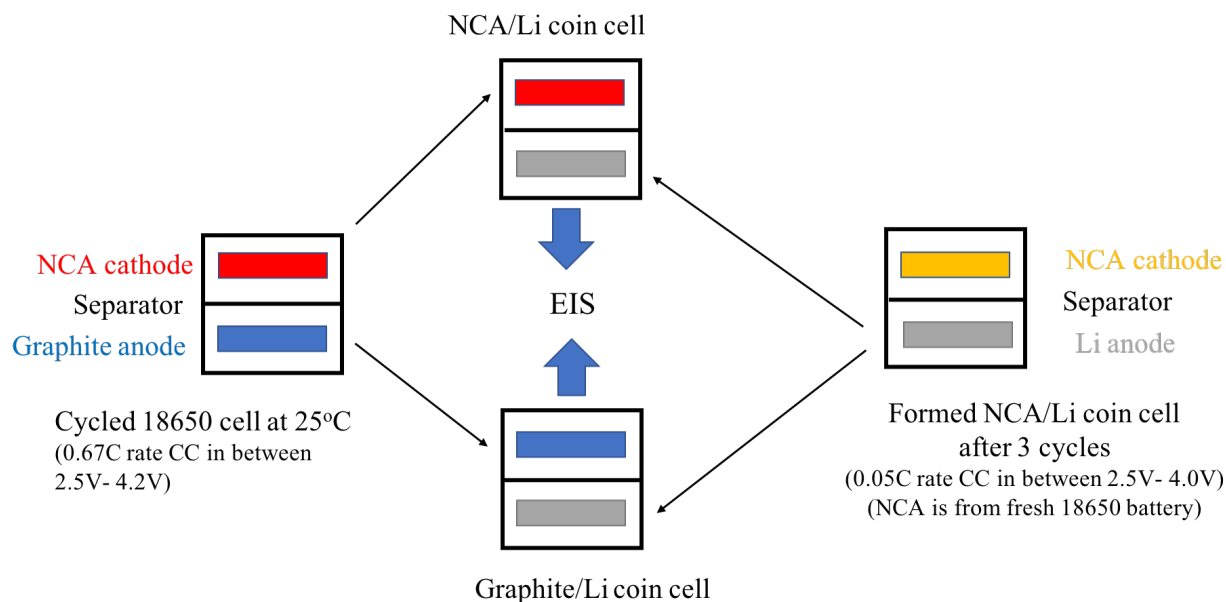


**Figure 4-1.** Schematic of how the hybrid cells were prepared from the 18650 batteries in order to separately collect EIS data of the anode and cathode of the 18650 batteries

a 14mm-diameter graphite anode (blue) was collected from the 18650 cell. This was paired with a 15mm-diameter Li anode (grey), which was collected from a NCA/Li coin cell after 3 slow cycles in order to clean the Li surface. To test the NCA cathode, a 14mm-diameter NCA cathode (red) was collected from the same 18650 cell described above. This was then paired with a separate 15mm-diameter Li anode (grey), collected as before from a different NCA/Li coin cell after 3 slow cycles in order to clean the Li surface. Commercial electrolyte (1 M  $\text{LiPF}_6$  in 1:1 ethylene carbonate (EC): diethyl carbonate (DEC)) was used in both re-assembled coin cells. Both coin cells rested for 3 hours before performing the EIS tests. The EIS for the coin cells was measured between 100 kHz and 50 mHz by applying a  $300 \mu\text{A}$  sinusoidal current perturbation.

#### 4.2.3 Anode morphology characterization

SEM and FIB cross-section were conducted based on the experimental section description in Chapter 3. The samples were kept in an Argon glove-box before being exposed to air for a short time during transfer into the instruments.

#### 4.2.4 Chemical composition characterization

XPS, EDS and FT-IR were conducted to get the chemical information of anode surface with different depth of information. For all the test, multiple areas were analyzed per sample to get average data of the elemental content. The samples were kept in an Argon glovebox before being exposed to the air for a short time during the transfer into the instruments.

### 4.3 Result

First, we will describe all the electrochemical test results of the 18650 cells under different cycling conditions and then address results from the coin cells assembled using harvested electrodes from the 18650 cells. Finally, we will discuss the morphology and chemistry characterization of the anode surface.

#### 4.3.1 18650 cells cycling and aging

Figure 4-2 shows the electrochemical data of 18650 cell under the different specified cycling conditions. These data, shown in Figure 4-2 (a), show two trends. First, the (CC-CV) cells generally show a slower capacity degradation rate than the (CC) cells at both temperatures. Second, the [CC, 25 °C] cell shows a much faster capacity degradation rate than the [CC, 60 °C]

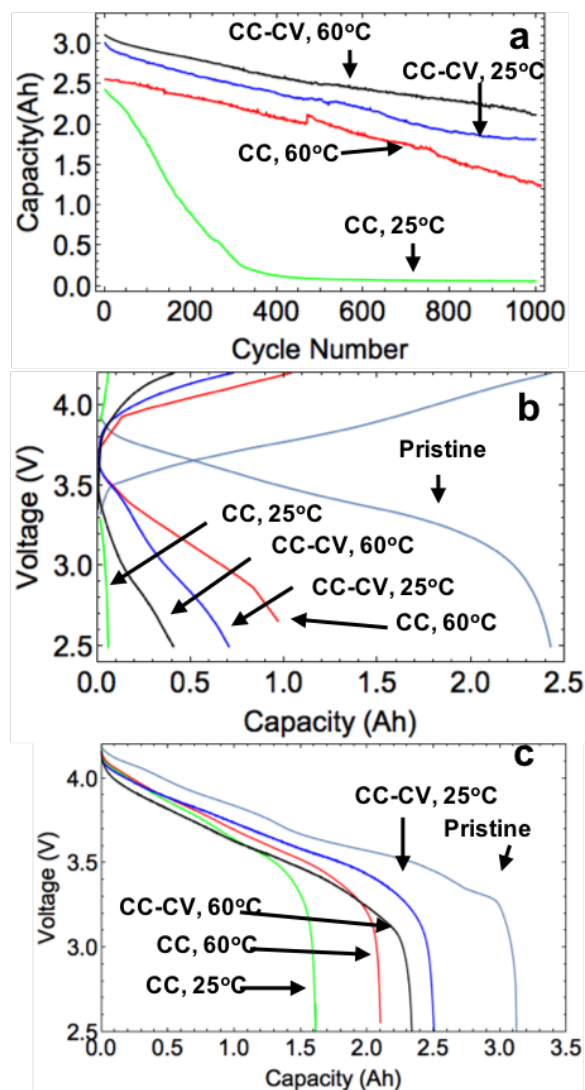


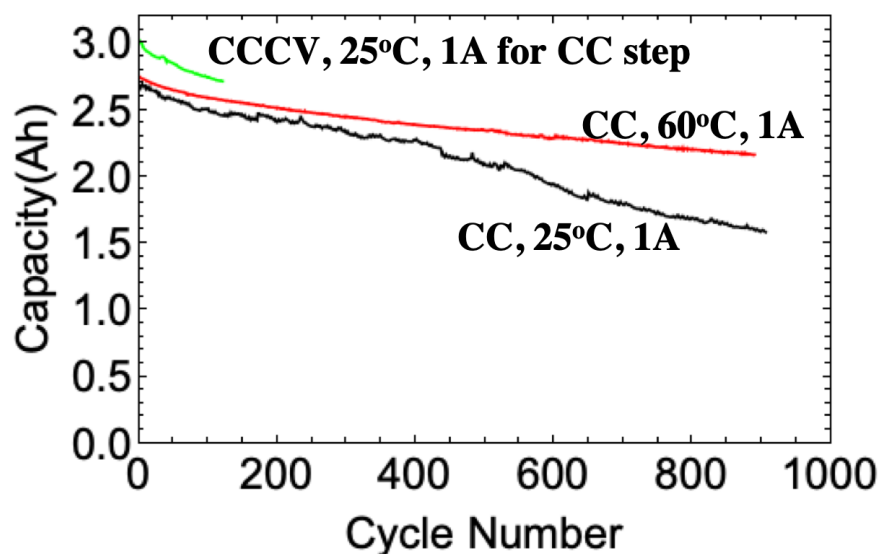
**Figure 4-2.** The data for 18650 battery cells cycling under four different conditions. (a) Long-term cycling data of the 18650 cells. (b) Charge-discharge cycles at 25 °C with a 2 A current in between 2.5 V and 4.2 V after finishing 1000 cycles (c) Discharge curves of the reference cycle with 0.02 C rate at 25 °C for the cells after finishing 1000 cycles under different conditions.

cell. After 1000 cycles, we compare the charge-discharge performance of the [CC, 25 °C] and [CC, 60 °C] batteries at 25°C in Figure 4-2 (b). It shows that under a 2A current and the voltage cut-off conditions, the [CC, 25°C] and [CC, 60°C] cells have 0.05 Ah and 1 Ah discharge capacities, respectively, and that the [CC, 25°C] cell shows larger resistance than the [CC, 60°C]



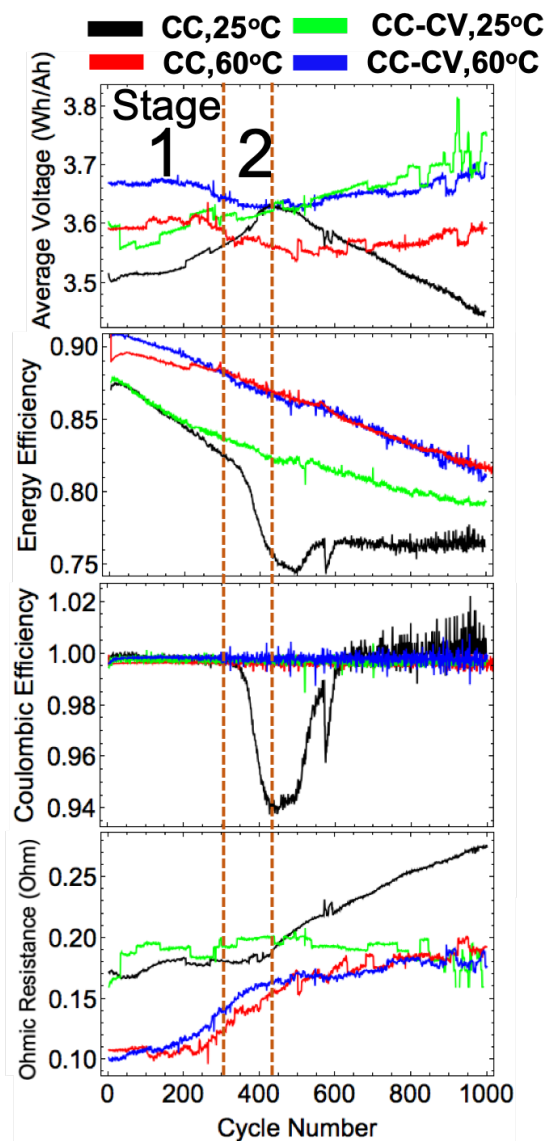
cell. Reference cycle data (discharge only) after 1000 cycles is shown in Figure 1(c). During the reference cycle, a very low current (0.02 C rate) ensures that the over-potential is negligible such that the realized discharge capacity is representative of the true available capacity of the cell system. Figure 4-2 (c) shows that the cells using the CC charge protocol have a lower available capacity at both 25°C and 60°C than their counterparts using the CC-CV charge protocol. Additionally, the batteries cycling at 25°C show lower available capacity than the 60°C cells using both CC and CC-CV protocols.

Figure 4-3 shows that when changing the current of CC step from 2A to 1A, the degradation rate of the cells under all condition improves with compared with the ones with 2A as shown in Figure 4-2. Especially, for the cell under [CC, 25 °C] but with a 1A current for CC step, the degradation rate becomes much better, suggesting the aging mechanism in this case is different than the one with 2A current for CC step.



**Figure 4-3.** Long-term cycling data of the 18650 cells under CC and CCCV conditions at both 25°C and 60°C. The current at CC step is 1A.

Figure 4-4 shows the average voltage with Ohmic resistance correction, Energy efficiency, Coulombic efficiency, and Ohmic resistance of the cells under different cycling conditions. The averaged voltage per cycle is based on the equation that  $V_{average} = \frac{E_{charge}}{Q_{charge}}$ . The Ohmic-resistance -corrected average voltage is calculated by the average voltage minus Ohmic resistance as shown in the equation  $V_{IR\ average} = V_{average} - I * R_{Ohmic\ resistance}$ . The Ohmic-resistance -corrected averaged voltage in the stages labeled in the plot are mainly based on the different results of the [CC, 25 °C] cell. Figure 4-4 (a) shows that the [CC, 25 °C] cell has a large increase in average voltage during Stage 1 and Stage 2, while the cells under the other three conditions show a generally smaller variation in average voltage. Figure 4-4 (b) shows that all of the cells under all the cycling conditions show gradually decreasing EE (energy efficiency) in Stage 1. During Stage 2, the [CC, 25 °C] cell shows a much faster rate of EE decrease than the other three. Figure 4-4 (c) shows that during Stage 1, the cells under all the cycling conditions show high QE (coulombic efficiency), close to 1. However, during Stage 2, the [CC, 25 °C] cell has a dramatically decreasing QE while the cells under the other three conditions maintain a high QE. Figure 4-4 d shows that the [CC, 25 °C] cell shows a small increase of Ohmic resistance during Stage 1 and 2. After Stage 2, the Ohmic resistance increases significantly.



**Figure 4-4.** The black line is for the [CC, 25 °C] 18650 cell; the red line is for the [CC, 60 °C] 18650 cell; the green line is for the (CC-CV, 25 °C) 18650 cell and the blue line is for the (CC-CV, 60 °C) 18650 cell. “Stage 1” and “Stage 2” are labeled for the convenience of result discussion. (a) Average voltage during charge process with Ohmic resistance correction, (b) Energy efficiency, (c) Coulombic efficiency, and (d) Ohmic resistance VS cycle number.

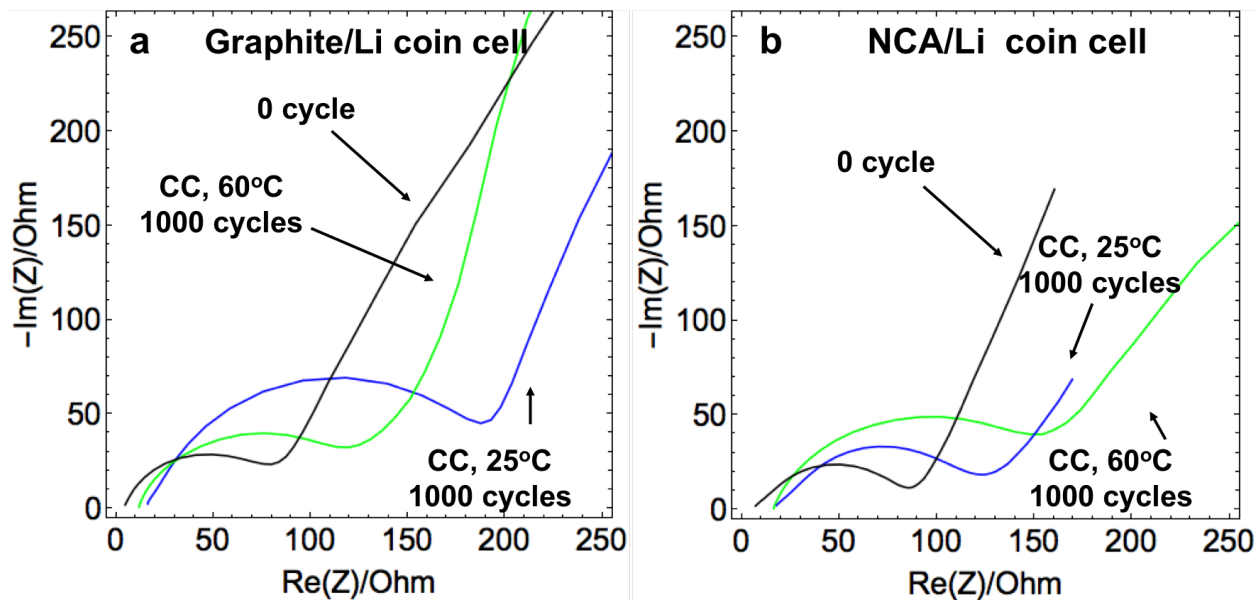


**Figure 4-5.** (a) EIS of the graphite/Li coin cell with the anodes extracted from either a pristine 18650 cell, the [CC, 25 °C] cell or the [CC, 60 °C] cell. (b) EIS of the NCA/Li coin cell with the cathodes extracted from either a pristine 18650 cell, the [CC, 25 °C] cell or the [CC, 25 °C] cell.

#### 4.3.2 Electrochemical characterization of harvested electrodes

To further study electrode impedance change before and after cycling, the EIS of the anode and cathode separately extracted from the [CC, 25 °C] cell and the [CC, 60 °C] cell are done, as shown in Figure 4-5. The charge transfer resistance of the anode from the [CC, 25 °C] cell increases around 120% after 1000 cycles compared to the pristine one while the anode from the [CC, 60 °C] cell increases around 40%. As for the cathode, the charge transfer resistance of the cathode from the [CC, 25 °C] cell increases 35% after 1000 cycles. The charge transfer resistance is the resistance against the process of electron transfer from one phase to another. In our case, it would be between graphite (solid state phase) and electrolyte (liquid phase).

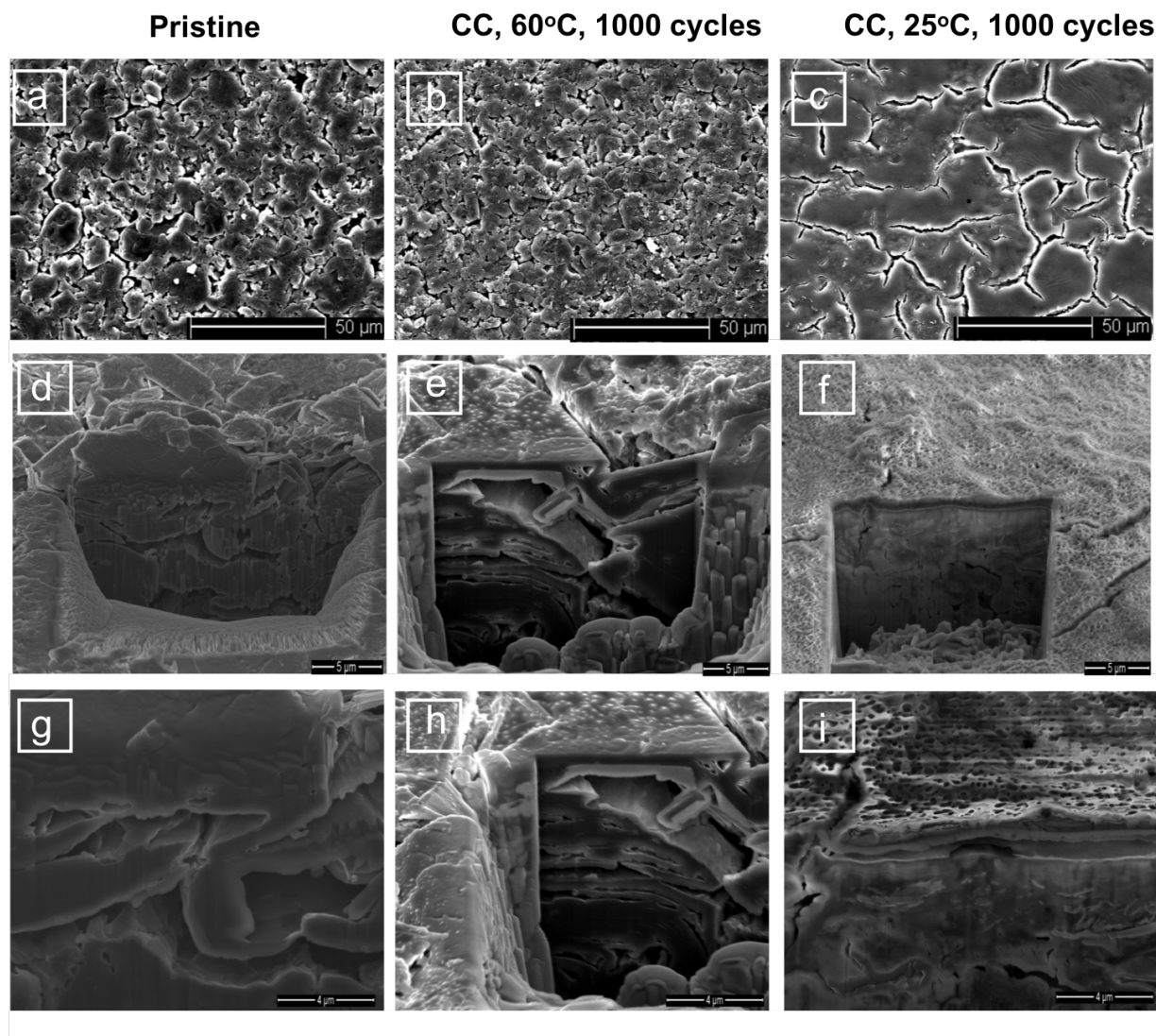


**Figure 4-6.** SEM and FIB cross sectional images of the anode extracted from (a)(d)(g) a pristine cell, (b)(e)(h) the [CC, 60 °C] cell after 1000 cycles, (c)(f)(i) the [CC, 25 °C] cell after 1000 cycles. (g), (h) and (i) are zoomed-in image at surface of (d), (e) and (f) respectively.

#### 4.3.3 Morphology and surface chemistry characterization of harvested anode

Using a SEM with focused ion beam (FIB) sectioning capabilities, we characterized both the surface and a cross-section of the anodes from our samples, as shown in Figure 4-6. In Figure 4-6 (b), the anode extracted from the [CC, 60 °C] cell doesn't show an obvious difference from that

of the pristine cell in Figure 4-5 (a). In comparison, the anode extracted from the [CC, 25 °C] cell in Figure 4-6 (c) has a distinct layer of SEI at the surface of the anode. We will refer to this layer of SEI in Figure 4-6 (c) as the thick secondary SEI in the rest of the chapter. From the cross-section image captured using FIB in Figure 4-6 (f), it is clear to see the thick SEI layer on the anode surface and the thickness of the SEI is around 1  $\mu\text{m}$  while the same thick SEI is not seen in Figure 4-6 (d-e). Based on Figure 4-6, it is evident that the thick secondary SEI forms on the anode surface extracted from the [CC, 25 °C] cell is significantly different from the SEI formed on the anode surface extracted from the [CC, 60 °C] cell and the SEI formed during manufacturing. Also, this thick secondary SEI forms only on the anode's surface as opposed to the SEI that normally forms throughout the anode on the surface of all the anode active material particles.

For chemical characterization of the anode, FT-IR and XPS data were collected, as shown in Figure 4-7. In Figure 4-7 (a), the FT-IR data of the anode extracted from the [CC, 25 °C] cell shows two different absorption peaks at  $1770\text{cm}^{-1}$  and  $1540\text{ cm}^{-1}$ , which are not present in the spectra from the anodes of the [CC, 60 °C] cell and of the pristine cell. In Figure 4-7 (b), the C 1s spectra of the anode from the [CC, 25 °C] cell shows an extra peak around 289.7 eV, which is likely to be  $\text{Li}_2\text{CO}_3$ . The elemental content of the anode surface based on EDX data is shown in Table 4-1. Three different locations are chosen for each sample to get averaged EDX data. The results shown in Table 4-1 are based on the average value with a certain deviation. The fluorine and oxygen content of the anode extracted from the (CC, 25 °C) cell is much higher than that of the (CC, 60°C) cell. Note that FT-IR, XPS and, EDX were done after the samples were exposed to air during sample transfer into the instruments. It is true that oxidation of the anode surface

likely occurred in this short time so that the results we show are not representative of the materials chemistry before the samples are exposed to air. However, this significant difference in the data after they are all exposed to the same amount of air reveals that the original surface chemistry of the anode must have been significantly altered in the batteries cycled at 25 °C compared with the pristine cell.

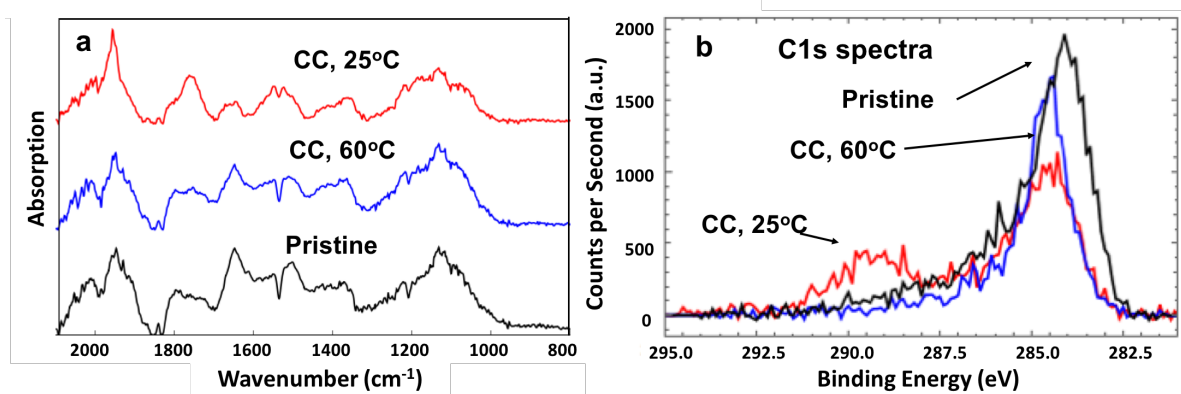


**Figure 4-7.** (a) FT-IR of the anode and (b) XPS C 1s spectra of the anode extracted from a pristine cell, the [CC, 60 °C] cell and the [CC, 25 °C] cell.

Table 4-1. Atomic% at Anode Surface by EDX from Different Cells			
Element	Pristine	CC, 25°C, 1000 cycles	CC, 60°C, 1000 cycles
C	94±2 %	43±4 %	84±4 %
O	5±0.8 %	31±3 %	7±1%
F	1±0.5 %	26±5 %	9±2 %

## 4.4 Discussion

Figure 4-1 (a) suggests that the charge protocols tested here have a profound impact on the capacity degradation rate, whereas the cycling temperature only has an effect on the capacity

degradation rate when the CC charge protocol is used. The implication is that the CC-CV protocol is a better choice for this type of cell when doing long-term charge-and-discharge cycling. However, if the cell uses the CC charge protocol, the cell has a better long-term performance at 60 °C than at 25 °C, and it is generally similar to the performance of the CC-CV charge protocol at both 25 °C and 60 °C. Since the [CC, 25 °C] cell behaved surprisingly worse than the [CC, 60 °C] cell, we will focus our discussion on these two cases at 25 °C.

The data in Figure 4-2 (b) suggests that the [CC, 25 °C] cell has larger resistance than the [CC, 60 °C] cell. It should be noted that during tear-down process, no obvious mechanical damage was observed, including electrode delamination and/or the destruction of active material particles. As such, the observed effects do not seem to be attributable to mechanical degradation mechanisms. The EIS tests of the coin cells in Figure 4-5 suggest that the increasing resistance of the [CC, 25 °C] cell after cycling mainly comes from the anode instead of the cathode. The morphology of the anode surface (Figure 4-6) show that there is a thick secondary SEI formed on the anode surface extracted from the [CC, 25 °C] cell while the same SEI is not detected on the anode extracted from the [CC, 60 °C] cell. The crack of the thick secondary SEI is formed potentially due to evaporation of electrolyte solvent. The similar crack was also observed in under microscope where vacuum environment was not needed. Based on the above discussion, we think that the thick secondary SEI on the anode surface is electrochemically resistive. The FT-IR, XPS and EDX data in Figure 4-7 and Table 4-1 also suggest that the surface chemistry of the anode extracted from the [CC, 25 °C] cell is different from that of the [CC, 60 °C] cell and the pristine cell, particularly the fluorine content. Previous papers<sup>25, 61-62</sup> posit that the SEI growth is more severe and cell performance is worse when the cell is operated at 60 °C than at 25 °C,



which is in contrast to the results presented. Based on the data of electrochemical tests, morphology and chemical characterization, a possible explanation is that, when this particular cell chemistry is cycled at 25 °C, a thick secondary SEI is formed by electrolyte decomposition products shuttling to the anode surface and being reduced, as suggested by Burns et al.<sup>49</sup>

We have also considered how temperature and the shuttling of decomposition products from the cathode to the anode could explain why the thick SEI formed in the [CC, 25 °C] cell anode but not the [CC, 60 °C] one. Previous reports<sup>37, 41, 43-44</sup> have claimed that among the decomposition products formed at the cathode surface, CO<sub>2</sub> is the most likely compound to shuttle to and reduce on the anode surface.<sup>37, 63</sup> The reduction products of CO<sub>2</sub> on the anode surface would be Li<sub>2</sub>C<sub>2</sub>O<sub>2</sub> or some related carbonate<sup>63</sup>. However, the EDX data (Table 4-1) shows the anode surface extracted from the [CC, 25 °C] cell has significantly higher F content than the other samples. Additional electrolyte decomposition products at the cathode include compounds such as POF<sub>3</sub>, POF<sub>2</sub>R and POFR<sub>2</sub>.<sup>64-66</sup> (The specific side group that R represents depends on the solvent used in the electrolyte). The reduction product of these on the anode surface should contain F.

Therefore, in order to explain our results, we propose the theory shown in the Figure 4-8. At 60 °C, the electrolyte decomposition product at cathode/electrolyte interphase has a higher gas content (mostly CO<sub>2</sub>) than that at 25 °C due to different decomposition reaction kinetics at the

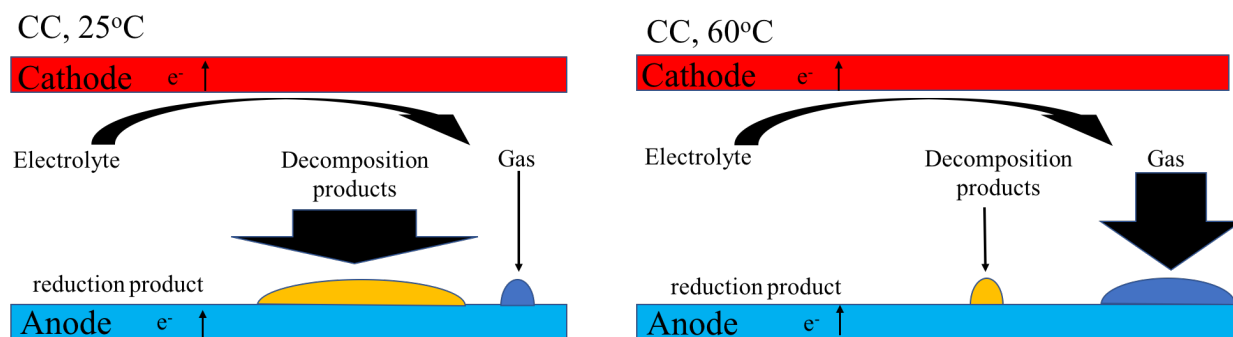


**Figure 4-8.** A schematic of the proposed formation of the SEI on the anode surface in 18650 batteries at 25 °C and 60 °C under CC charge condition. This figure is modified based on the figure from the reference.<sup>44</sup>

different temperatures, with gas formation being favored at higher temperatures. When these products are shuttled to the anode and are reduced on the anode surface, the reduction product at 60 °C is mostly the result of  $\text{CO}_2$  while the reduction product at 25 °C has more F content. An examination of the exact composition of the decomposition products and their reduction products at both 25 °C and 60 °C is beyond the scope of this paper.

At this point, we wish to further explain how the thick secondary SEI contributed to why the [CC, 25 °C] cell showed faster capacity degradation rate than the [CC, 60 °C] cell. During Stage 1 in Figure 4-3, the DC resistance of the [CC, 25 °C] cell stays relatively stable. The increasing Ohmic-resistance -corrected average voltage and the decreasing EE of the [CC, 25 °C] cell suggest that some transportation barrier is built up. Therefore, the over-potential in the cell increases and the deliverable capacity under the same voltage cut-off decreases. This is shown in Figure 4-2 (a), where the majority of the capacity decrease occurs during Stage 1, which is about 0-300 cycles. We propose this transportation barrier could come from the thick secondary SEI formed on the anode surface. While the Li plating could potentially cause similar transportation

barrier as a result of reaction with electrolyte, this is not likely to happen during Stage 1. We suggest that this is the case since the QE for [CC, 25 °C] cell is still close to 1 (even higher than the [CC, 60 °C] cell). If the Li plating happened during Stage 1, the QE value would be observed to drop very fast according to the Li plating model published by Yang.<sup>67</sup> During Stage 2, for the [CC, 25 °C] cell, QE starts to decrease dramatically and the average voltage and EE decrease at an even higher rate than in Stage 1. All of these suggest that the secondary SEI formed during Stage 1 resulted in a higher over-potential at the anode. In these conditions, we believe some of cyclable lithium in the system is consumed at the anode, as the QE decrease from 99% to 94% during this time. To investigate this, pristine and [CC, 25 °C] batteries are torn down and their anodes are immediately put into DI-water. Both the anode from the pristine 18650 cell and the [CC, 60 °C] cell show much less gas generation than the anode from the [CC, 25 °C] cell. Moreover, the DI-water the anodes are soaked in is found to be basic after the gas generation reaction, suggesting that the gas could be H<sub>2</sub> generated by water reacting with deposits on the anode surface of the [CC, 25 °C] cell. Therefore, the secondary SEI on the anode surface from [CC, 25 °C] cell is the result of the secondary SEI formed due to shuttle effect during Stage 1 plus the Li plating during Stage 2.

When comparing the cells under [CC, 25 °C] and [CCCV, 25 °C] conditions, it is clear that the cells behaves differently in term of degradation rate by adding the CV step. There are couple of potential reasons behind this. First, it is likely during the CV step, the electrolyte decomposition product did not migrate to anode surface because of the electric field under the current.<sup>44</sup> Instead, the decomposition product was consumed by cathode surface<sup>43</sup>. Although this could lead to growth of SEI on the cathode surface, the effect of the cathode SEI on the cell is less detrimental

than the effect of the secondary SEI on the anode surface. Second, if Li precipitation happens during the CC step, the precipitated Li on the anode surface can insert into graphite anode during the CV step. With that, there is less side reaction between the precipitated Li and electrolyte, which can cause less impedance. The examination of these reasons, however, is not in the scope of this chapter.

When comparing the cells [CC, 25 °C] condition but using 1A and 2A current for CC step, the cell using 2A current show much faster degradation rate. One potential reason is that the lower current leads to lower over-potential, which can lead to less side reaction on the cathode side or difference in composition of decomposition materials. Therefore, when the cell is cycled under 1A, the secondary SEI, which was formed under 2A current, is not formed or partially formed.

## 4.5 Conclusion

Both charge protocol and cycling temperature play important roles in commercially produced lithium-ion cell capacity degradation in long-term cycling.

When 18650 cells are cycled at 25°C, the CV step during charge process reduces formation of secondary SEI on the anode surface.

The thick secondary SEI from the [CC, 25 °C] cell has a large resistance and different chemical composition as compared to the SEI from the [CC, 60 °C] cell. It is theorized that at 25°C, the thick secondary SEI is gradually formed when the electrolyte decomposition products at the

cathode shuttle to the anode surface and get reduced, especially those decomposition products that contain fluorine while the gas is evolving more at the 60 °C.

# Chapter 5. Aging level and inhomogeneity of cathode linked to 18650 Li-ion cell in long-term cycling

## 5.1 Overview

To better understand NCA aging properties under different cycling conditions, we focus on the cathode side in the cell in this chapter. Relationships between observed cathode aging phenomena and cycling conditions were explored at the cell and cathode materials level. We note area-specific inhomogeneities in cathodes cycled under constant current charge protocol at 25 °C while such inhomogeneity was not observed in three other conditions. The mechanism behind the cathode inhomogeneity was discussed in the context of uneven growth of the secondary solid electrolyte interphase (SEI) on the anode surface from cells under constant current charge protocol at 25 °C.

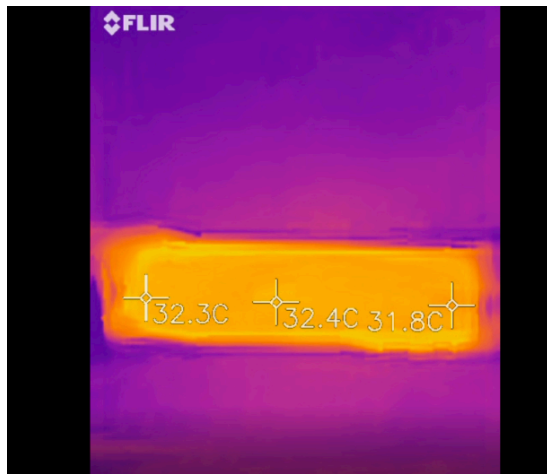
Hypotheses:

- At both 25°C and 60 °C, the aged cathode, extracted from 18650 cycling with CV step, shows lower electrochemical capacity and thicker SEI at cathode/electrolyte interface, when compared with aged cathode from 18650 cell without CV step.
- The inhomogeneity of aged cathode from 18650 cell under CC charge condition at 25°C results from the inhomogeneous temperature distribution of 18650 cell.

## 5.2 Experimental

In general, the 18650 cycling test, tear-down procedure, the electrode acquirement procedure, electrode fabrication process is described in Chapter 3

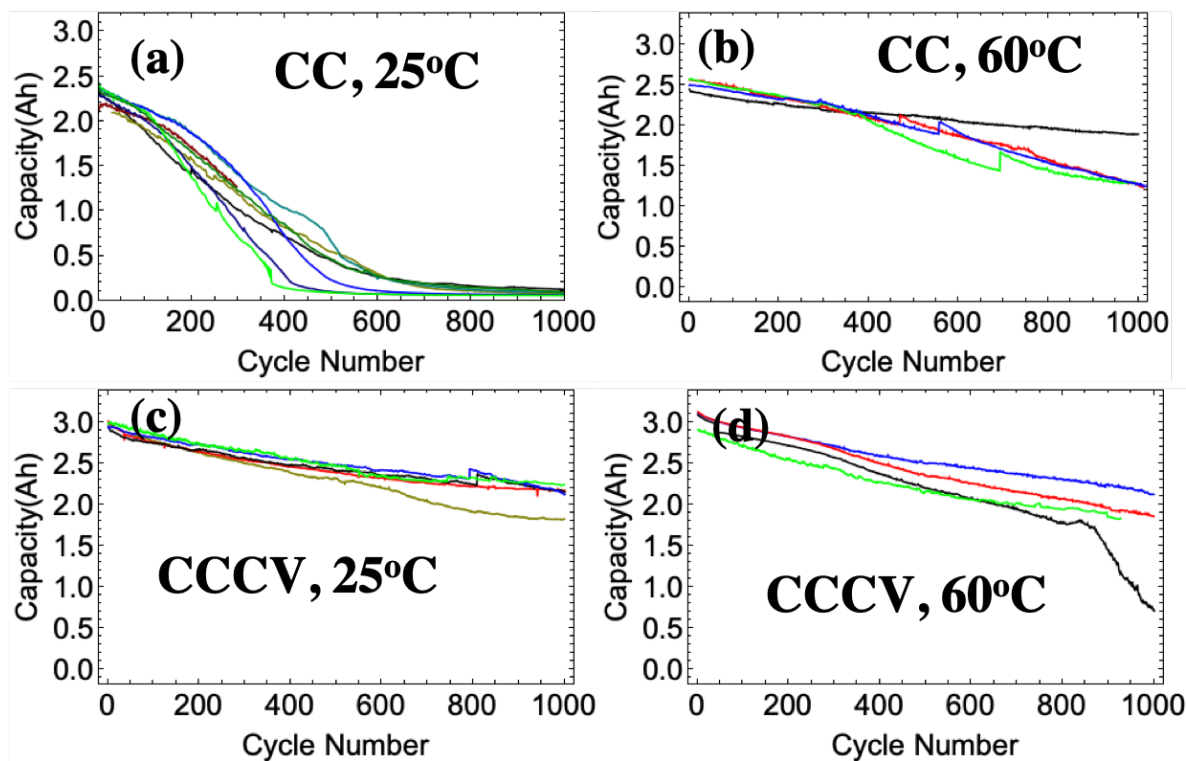
As for the in-situ thermal measurement, thermal detector from FLIR was used and the three measured points were located at two ends and center locations, as shown by Figure 5-1.



**Figure 5-1.** In-situ thermal measurement of 18650 cell during long-term cycling.

## 5.3 Result

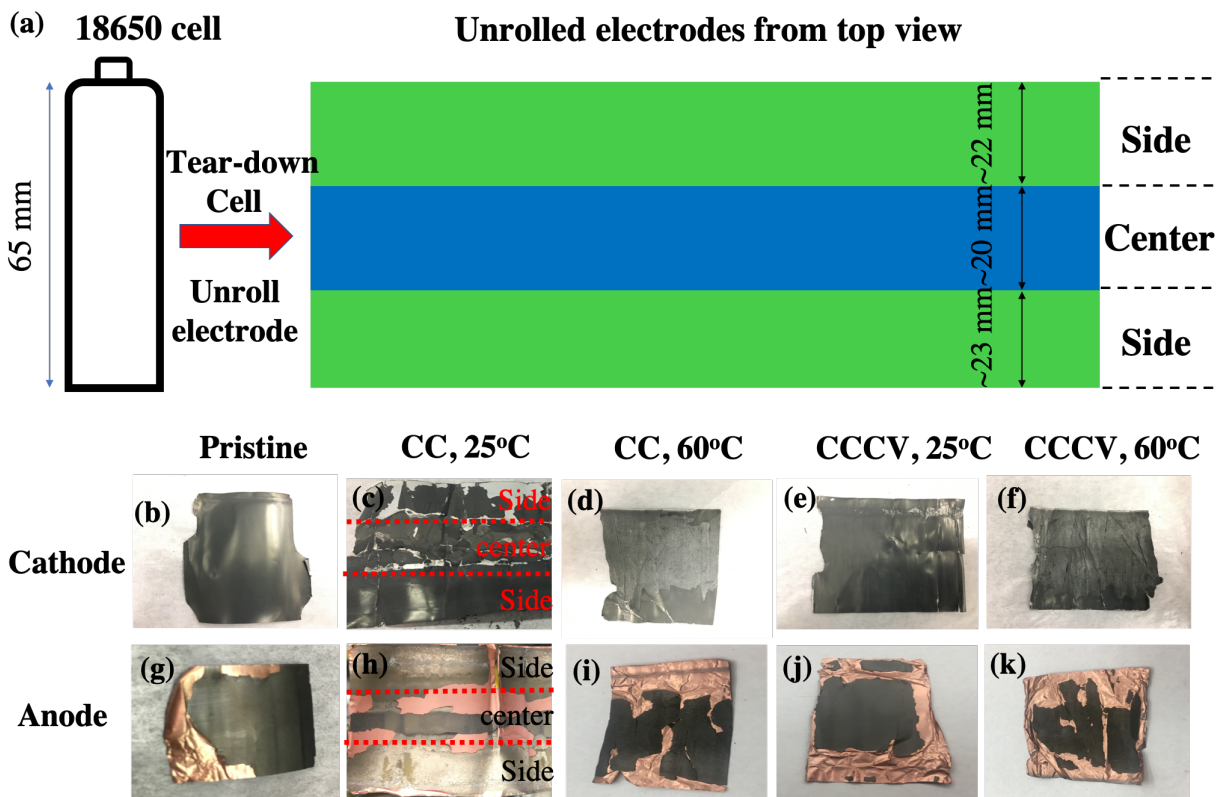
Figure 5-2 shows the long-term cycling result of 18650 cells under different conditions. The [CC, 25°C] cell shows much faster capacity degradation than cells under three other conditions. The tests were repeated multiple times at each condition: these unexpected results are repeatable



**Figure 5-2.** 18650 cell long-term cycling performance under different conditions with repeat. For CC charge step, 2A current was used with 4.2V voltage cut-off. For CV step, the voltage was held at 4.2V with a current cut-off at 59mA. For discharge step, 2A current was used with 2.5V voltage cut-off

Figure 5-3a is a schematic of the electrodes once they are removed and unrolled. In some cases, the electrodes have three distinct regions running parallel to the long direction of the electrode. Optical images of the cathode and anode electrodes extracted from cells after cycling under the different condition are shown in Figure 5-3(b-k). Both the cathode and anode from the [CC, 25°C] cell show location-based differences in electrode appearance and adhesion, while the cathode and anode pair from cells tested under the other three conditions are nominally homogeneous in appearance. As shown in Figure 5-3 (c), the cathode at the center of the [CC 25°C] cathode is partially delaminated while the cathode in the “side” location do not show any

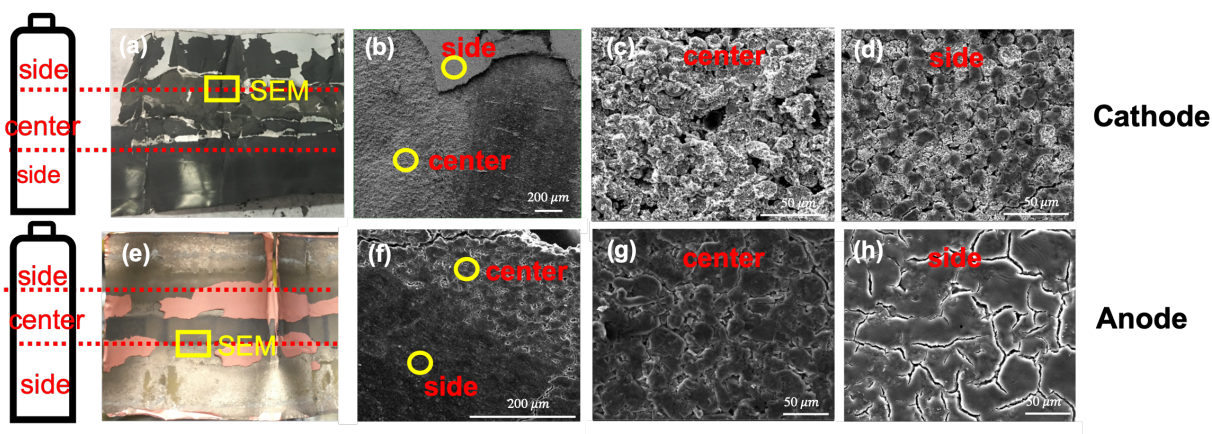




**Figure 5-3.** (a) Schematic diagram of the electrode extracting process and naming of electrode based on location; image of cathode and anode extracted from pristine cell (b,g), [CC, 25°C] cell (c,h), [CC, 60°C] cell (d,i), [CCCV, 25°C] cell (e,j) and [CCCV, 60°C] cell (f,k) after 1000 cycles.

sign of delamination. The anode sample for this same cell is shown in Figure 5-3 (h). The anode material at the center is a dark black color while the anode at the “side” presents a shiny dark grey surface. For all the extracted anodes, part of the anode materials delaminated off of the current collector during tear-down.

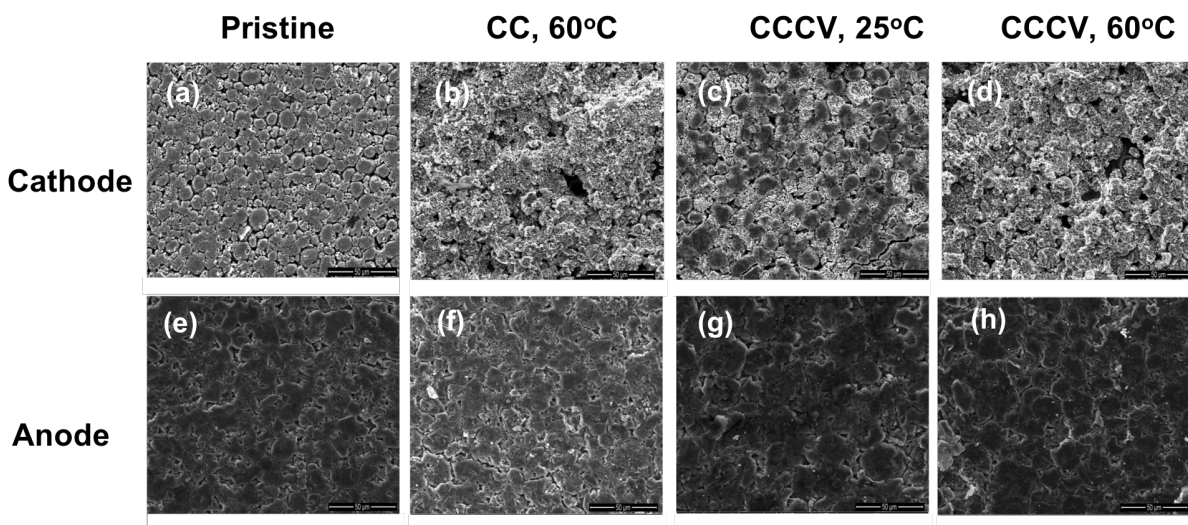
Since both the anode and cathode from [CC, 25°C] cell had significant areal variation across their electrode areas, we elected to characterize these different areas using SEM, as shown in Figure 5-4. Figures 5-4 (c) show that the surface of the cathode at the center of the electrode is



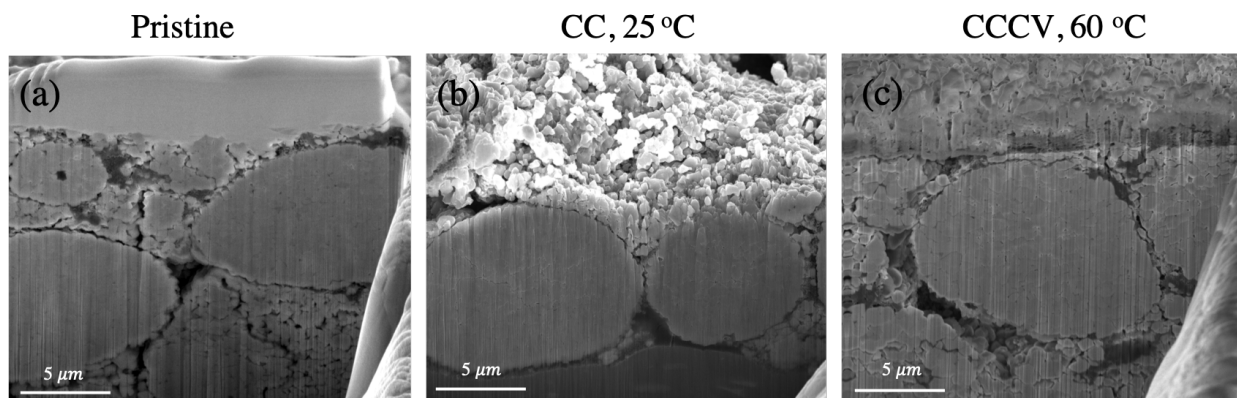
**Figure 5-4.** Images of cathode and anode extracted from [CC, 25°C] cell (a,e) after 1000 cycles. The yellow rectangles indicate the location for SEM images. SEM image of the cathode (b-d) and the anode (f-h) under different magnification. The yellow circle indicate the locations where the SEM images with higher magnification are done.

rough while elsewhere the surface is flat/smooth. For the anode in Figure 5-4 (e), the anode in both regions are also distinct from each other. Only the anode on the side with the shiny morphology has a thick “secondary SEI” layer on top of the surface of the anode, as seen in Figure 5-4 (f). This layer was investigated in our previous chapter, which showed that this layer has the thickness of 1  $\mu\text{m}$  (Figure 4-5 (i)) and caused large polarization due to poor Li-ion transport property potentially.<sup>1</sup> The anode at the center does not have a similar surface layer and the interfacial structure maintained the porous morphology, shown in Figure 5-4 (g). The cathode and anode from pristine cell and [CC, 60°C] cell, [CCCV, 25°C] cell, [CCCV, 60°C] cells were also characterized by SEM. The cathode harvested from the [CCCV, 25°C] cell (Figure 5-5 (c)), shows a flat surface just like the cathode from the pristine cell (Figure 5-5 (a)). But the cathode from both [CC, 60°C] cell and [CCCV, 60°C] cell shows rough surfaces, Figure 5-5 (b, d). The

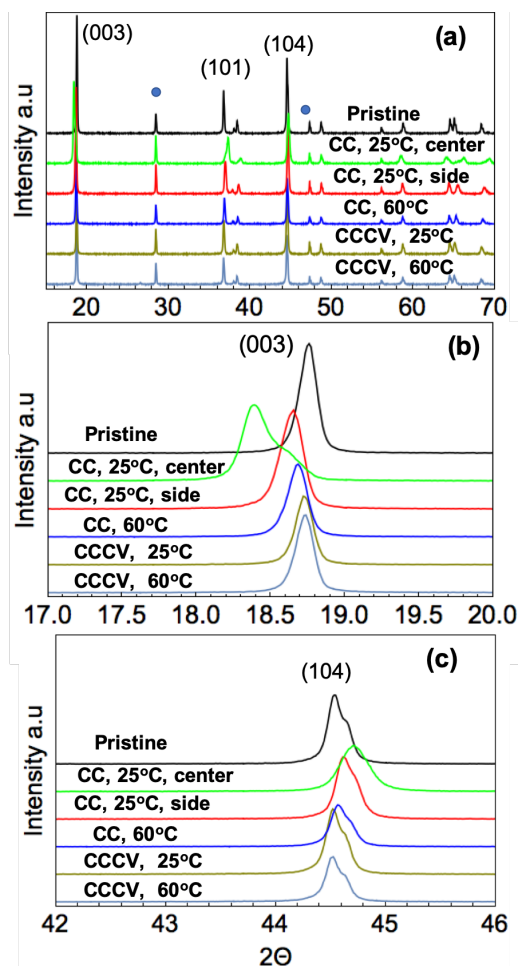
anode from [CC, 60°C] cell, [CCCV, 25°C] cell, [CCCV, 60°C] cell all had porous surfaces, like the anode from the pristine cell. Cross-section images were collected by FIB-SEM (Figure 5-6). No severe crack was observed in the cathode collected from [CC, 25°C] cell, [CCCV, 60°C] cell.



**Figure 5-5.** The SEM image of cathode (a-d) and of anode (f-h) extracted from pristine 18650 cell and [CC, 60°C], [CCCV, 25°C] and [CCCV, 60°C] cells after 1000 cycles.



**Figure 5-6.** FIB image of cathode from (a) pristine cell, (b) [CC, 25°C] cell and (c) [CCCV, 60°C] cell after 1000 cycles.



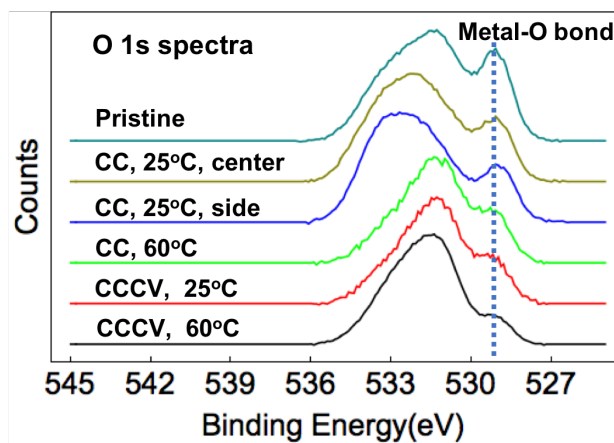
**Figure 5-7.** (a) X-ray diffraction pattern comparison between cathode extracted from pristine, CC, 25°C], [CC, 60°C], [CCCV, 25°C] and [CCCV, 60°C] cells after 1000 cycles. (b-c) Zoomed-in peak (003) and (104) from (a). The blue dots indicate peaks of Si for calibration.

Figure 5-7 (a) shows the X-ray diffraction pattern of the cathode harvested from a pristine cell, from a cell after cycling under the four different conditions described in the experimental section. For the cathode from the [CC, 25 °C] cell, the material from both side region and center region are characterized separately. All NCA samples show the same layered crystal structure (space group  $R\bar{3}m$ ) without impure phase peaks. Taking a closer look at (003) and (104) peaks of the layered

structure NCA in Figure 5-7 (b-c), the peak location of cathode from [CC, 60 °C], [CCCV, 25 °C] and [CCCV, 60 °C] cells after 1000 cycles is slightly different from that of pristine cell. But the peak location of cathode at the side and at the center from [CC, 25 °C] cell after 1000 cycles, especially the cathode on the center, shifted a lot more than other cathode samples.

The XPS data in Figure 5-8 shows that, while in the O 1s spectra, the bonds with higher binding energy than 530 eV are hard to differentiate, the metal-O bond with binder energy around 529 eV is clear. The peak intensity for metal-O bond in different cathode lie in the sequence: pristine < [CC, 25°C] center  $\cong$  [CC, 25°C] side < [CC, 60°C]  $\cong$  [CCCV, 25°C] < [CCCV, 60°C].

In Figure 5-9, the cathode was extracted from the 18650 cell after tear-down process and re-fabricated into electrode for reference cycle test in coin cell following the procedure described in



**Figure 5-8.** XPS O 1s spectra of the cathode from pristine, [CC, 60°C], [CCCV, 25°C] and [CCCV, 60°C] cells and [CC, 25°C] cell at both the side and center after 1000 cycles.



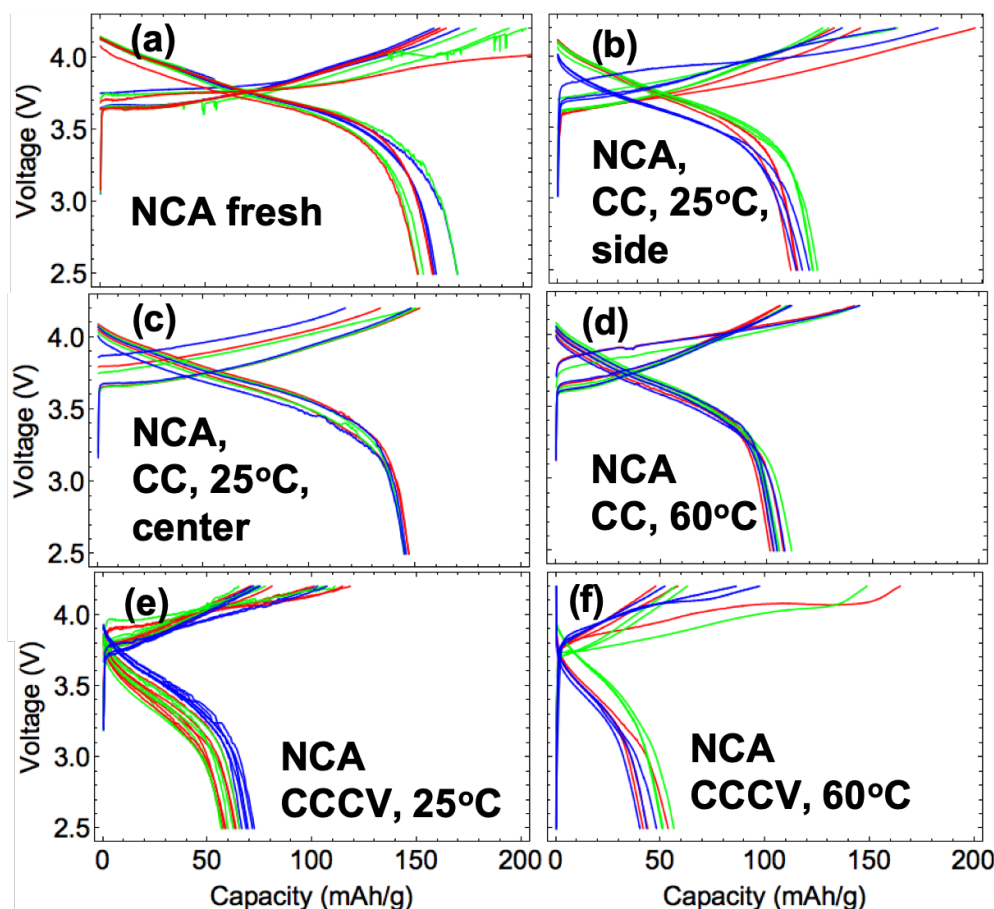


**Figure 5-9.** The reference cycle of re-fabricated cathode from different 18650 cells after long-term cycling. For reference cycle, the coin cell is cycled at 0.1C rate for both charge and discharge with 2.5 V and 4.2 V voltage cut-off. For each sample, 3 coin cells were made (shown by different color). For each cell, 3 reference cycles were done (a). cathode from pristine cell; (b) cathode at side location from [CC, 25°C] cell; (c) cathode at center location from [CC, 25°C] cell; (d) cathode from [CC, 60°C] cell; (e) cathode from [CCCV, 25°C] cell and (f) cathode from [CCCV, 60°C] cell.

the experimental section. Under a C/10 charge/discharge rate, the observed discharge capacity suggests the deliverable capacity of cathode active materials. The sequence for discharge capacity of cathode is: pristine > [CC, 25 °C] center > [CC, 25 °C] side > [CC, 60 °C] > [CCCV, 25 °C] > [CCCV, 60 °C].

## 5.4 Discussion

### 5.4.1 Cathode aging in full cell under different cycling conditions

To facilitate better understanding, we will use the [CC, 25°C] cell and the [CCCV, 60°C] cell, which had the most contrasting test conditions and results, for comparison and discussion. A detailed discussion regarding the causes for the performance of [CC, 25°C] cell is in chapter 4, and this topic is not the primary focus of this paper. Briefly, a thick secondary SEI formed on the anode surface in all cells cycled using the CC,25°C charge cutoff condition, which we found to cause the observed performance. We will first compare how the electrodes aged under these two conditions with a focus on relating full cell performance during cycling to electrodes aging.

#### 5.4.1.1 Anode

For the [CC, 25°C] cell anode, there was a thick layer of SEI growing on the surface of the anode on the side locations as shown in Figure 5-4 (f, h). Based on SEM-FIB section analysis (Figure 4-5 (i)), we find that the secondary SEI layer has a thickness of approximately 1  $\mu\text{m}$ . Based on the coin cell test of the extracted anode in Figure 5-10, the electrochemical capacity of the [CC, 25°C] anode on the side location is less than 25 mAh/g and the [CC, 25°C] anode on the center location is around 130 mAh/g. The anode from [CCCV, 60°C] cell shows the capacity of 220 mAh/g (total mass of anode is used for calculation of specific capacity). The voltage drop at the beginning of discharge is larger for the anode on the side from [CC, 25°C] cell while the anode on the center from [CC, 25°C] cell and from [CCCV, 60°C] cell relatively the same, which is likely due to the transportation barrier of the secondary SEI.

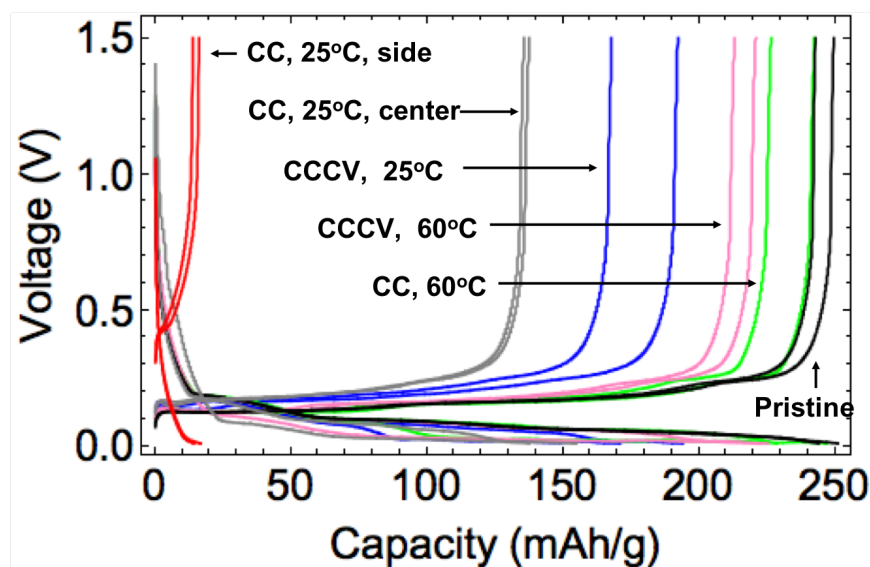


**Figure 5-10.** The reference cycle of anode extracted from different 18650 cells after cycling. For reference cycle, the coin cell is cycled at 0.1C rate for both charge and discharge with 0.01V and 1.5 V voltage cut-off.

#### 5.4.1.2 Cathode

The NCA materials used as cathode materials in this paper has a layered structure. For this type of structure, the (003) peak has scales directly with the lattice parameter  $c$  which is, in turn, directly correlated to Li content <sup>68</sup> (ie the lattice expands along the  $c$  axis when Li is not present within the structure, as is the case for  $\text{LiCoO}_2$ ). Using this assessment too, we found that the harvested cathode materials contained different amounts of Li (Figure 5-7 (b)). Specifically, the cathode material taken from the central location from the CC, 25°C cell contained significantly less Li than other harvested cathode materials. The cathode from the [CC, 25°C] cell (Figure 5-9 (b-c)) shows a loss of 10 and 30 mAh/g electrochemical capacity after 1000 cycles in the full cell compared with the cathode from the pristine cell (Figure 5-9 (a)) while the cathode from the



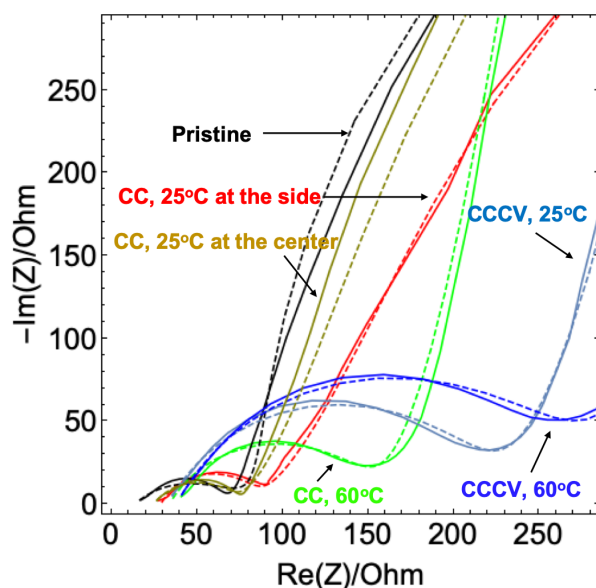
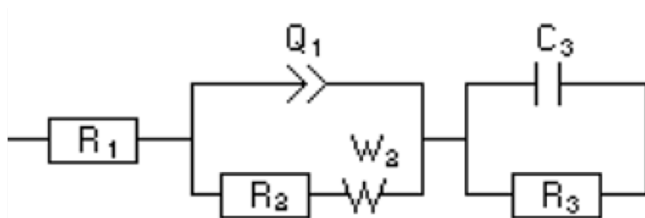


**Figure 5-11.** EIS of cathode extracted from 18650 cells after 3 reference cycles in coin cell. The solid-line is based on collected data. The dashed line is based on simulated data. The detailed simulated data is in Table 5-1.

**Table 5-1.** Equivalent circuit model and impedance parameters based on the model



	R1 (Ohm)	Q1 ( $F.s^{a-1}$ )	a1	R2 (Ohm)	s2 ( $\Omega.s^{-1/2}$ )	C3 (F)	R3 (Ohm)
Pristine	3.187	0.01165	0.038	13.82	3 253	0.01983	1093
[CCCV, 60°C]	2.486	16.25e-6	0.705	183.8	210.5	0.988 3e-3	40823
[CCCV, 25°C]	3.474	12.98e-6	0.700	221.7	181.9	1.502e-3	0.4929e18
[CC, 25°C ]at the side	38.81	57.66e-6	0.702	57.56	62.11	0.02181	631.6
CC, 60°C	4.417	23.43e-6	0.677	139.2	134.2	1.444e-3	14808
[CC, 25°C ]at the center	4.917	0.111 6e-3	0.604	49.38	37.08	0.03072	1069

[CCCV, 60°C] cell shows a loss of 100 mAh/g in capacity. The difference in the discharge capacity lies in the aging of cathode active materials (NCA). The EIS data (Figure 5-11) suggest the cathode from the [CCCV, 60°C] cell shows larger charge transfer resistance than the cathode from the [CC, 25°C] cell, which is likely due to the growth of SEI on the cathode surface and/or an interfacial reconstruction. Additionally, XPS assessment (Figure 5-8) indicated that peak intensity for metal-O bond is lower for the cathode from the [CCCV, 60°C] cell than from the [CC, 25°C] cell. This result is consistent with the existence of a thicker SEI formed on the cathode from [CCCV, 60°C] cell.

#### 5.4.1.3 Full cell

For the [CC, 25°C] cell, chapter 4 has shown that the capacity is anode-limited and that the thick SEI on the anode surface is the key to the fast capacity degradation of the full cell. This thick SEI leads to high electrochemical impedance and limited transport and indicates the consumption of cyclable lithium. As such, the [CC, 25°C] cell shows large polarization and reaches the voltage cut-off without delivering full capacity, and the actual voltage on the cathode at the cell cut-off voltage is lower with increasing resistance on the anode the side.

Additionally, lithium consumption leads to a reduction of voltage usage window of the cathode. As the cyclable lithium is consumed by formation of SEI/ thick SEI layer, the amount of Lithium goes back to cathode is less during the charge process, which leads to decreasing of potential at cathode at the upper voltage cut-off. In other words, the cathode can't be charged to the same level as in previous cycle due to the consumption of cyclable Lithium, under the same cell upper voltage cut-off. Because of both effects mentioned above, the "usage" of cathode active

materials is low, leading to the low capacity loss of cathode active materials. This can be supported by the measured discharge capacity of the cathode after 1000 full cell cycles (Figure 5-9 (b-c)). For the [CCCV, 60°C] cell, a different degradation mechanism was evident as compared to the [CC, 25°C]; there was a clear lack of thick secondary SEI formation in the former. We suggest that the cathode active materials lost much more capacity than the cathode from [CC, 25°C] cell as shown by (Figure 5-9 (f)). The cathode capacity loss in the [CCCV, 60°C] cell is likely due to higher cycling temperature, longer cycling duration and commensurate longer exposure times to a higher cathodic voltage. These effects result in large interfacial resistance due to SEI build-up and/or a surface layer transformation from the layered structure to rocksalt structure, which is suggested by the larger semi-circle in EIS test in Figure 5-10.<sup>69</sup> The thickness of rocksalt phase (<50nm normally) is order of magnitude smaller than the particle size of NCA we have (~500nm). The XRD peaks location of rocksalt phase are very close to that of layer phase. These factors make it hard to detect and differentiate rocksalt phase from layer phase on XRD pattern Figure 5-7.

#### 5.4.2 Inhomogeneity in cathode aging in full cell

To our knowledge, areally inhomogeneous aging in cathode as a result of long-term cycling has not been reported before. The sectional difference in the electrode regions shown here (Figure 5-3 (c)) is from the outermost part of the rolled electrode, approximately the last 60 cm of the ~90 cm roll. The electrode from the inner part of electrode roll (i.e. closest to the bobbin during the cell rolling process) did not exhibit consistent sectional difference. The images in Figures 5-3 and Figure 5-4 show inhomogeneity in visual appearance and electrode materials morphology on both anode and cathode from the [CC, 25°C] cell. The delamination of the cathode occurred in

cells cycled at 60°C. This delamination was homogeneous at all locations (side and center), as shown in Figure 5-3 (d, f). In this case, the delamination mechanism could be related to the cycling temperature. In contrast, the cathodes from cell cycled at 25°C generally remain intact and showed no sign of delamination. The only exception is the center part of the cathode from [CC, 25°C] cell (Figure 5-3 (c)). This suggests that the cycling at high temperature is not the only cause for the delamination of the cathode. Other factors, which we will discuss later, also weigh in the cathode delamination. Moreover, the inhomogeneity in surface chemistry of the cathode materials is also manifested through XPS measurement. The difference in the XRD peak shift (Figure 5-7) indicates the difference in the level of lithiation. Moreover, electrochemical testing (Figure 5-9) shows that the cathode at the side has less capacity than that on the center.

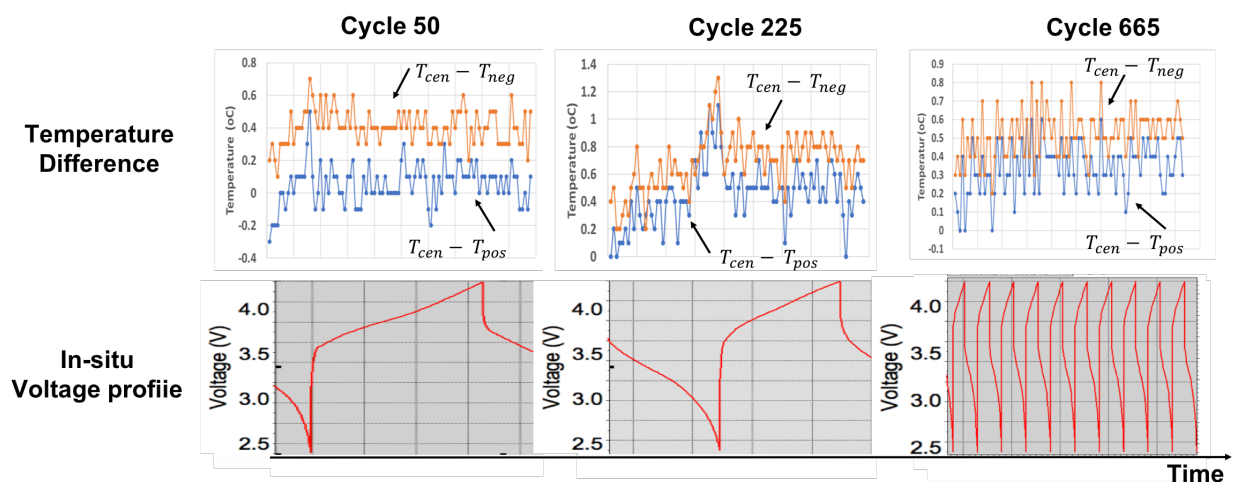


**Figure 5-12.** Temperature difference of [CC, 25°C] cell between center and positive/negative points along with the corresponding voltage profile during cycling. The current is 2A for both charge and discharge step with voltage cut-off at 2.5V and 4.2V

All the results above suggest there is inhomogeneous aging of the cathode aged as [CC, 25°C] cell over the electrode area, while this is not the case for the cathode cycle aged using the [CCCV, 60°C] condition. In-situ thermal measurements were also conducted during cycling

(Figure 5-12). There is uneven thermal distribution in the cell. This is due to the difference in the heat dissipation rate at different zones. At the center zone, the cell has less exposure to the air, reducing its heat dissipation rate. The surface temperature difference between location and two end locations of the 18650 cells was no more than 1.5 °C. With this temperature difference, the difference in the thermal volume expansion or change of conductivity along is not likely to cause such inhomogeneity.<sup>70</sup> The published papers<sup>71-73</sup> using CT-scan showed that there was room for electrodes near the top and bottom of the 18650 cell, suggesting the electrodes near the top and bottom of the 18650 cell did not experience “corner force” by the case. These results indicate that the inhomogeneity in the cathode did not originate from the uneven pressure distribution caused by the cell manufacturing.

While these effects are difficult to understand and interpret, we offer a potential causal mechanism that is based on the evolution of internal cell pressures in those cells that lost capacity most rapidly during testing (ie. CC, 25°C). The effects are separated into three stages (Figure 5-13): At stage 1, which is before cycling, there is no secondary layer growth on the anode surface anywhere. The secondary SEI layer we mentioned here is the layer of materials that covers the anode electrode surface where it interfaces with the separator; this is not the same SEI formed during formation cycle in the course of manufacturing. During stage 2, which occurs over the first several hundred cycles (under [CC, 25°C] in this case), the secondary SEI starts to form at anode surface near the top and bottom of the cell. As the secondary SEI gradually grows

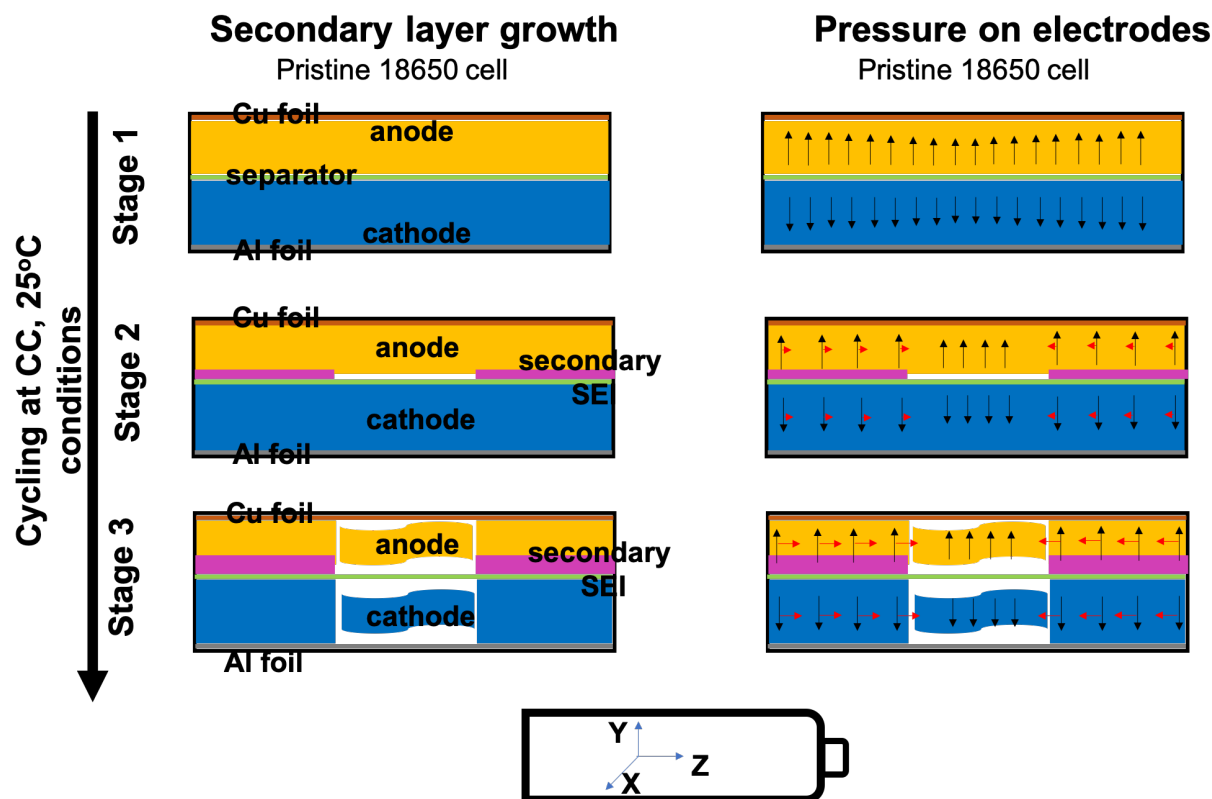


**Figure 5-13.** Cross sectional schematic of inhomogeneous aging in the electrodes from [CC, 25°C] cell. The figure on the left shows the growth of the secondary layer on the anode surface in different stages while the figure on the right shows the pressure changes in both direction and size suggested by the arrows. The Y-axes is along the radial direction and the Z-axes is along the axial direction. The arrow of the pressure is along the Y-axes. Stage 1 is before the long-term cycling, stage 2 is during long-term cycling and stage 3 is after long-term cycling.

thicker, the pressure on the electrodes near the top and bottom of the cell increases due to limited space available inside the case. This increased pressure then decreases the local porosity and increases the tortuosity of the separator and electrodes, which then further limits lithium diffusion path through the separator and the porous anode.<sup>74-75</sup> This leads to further growth of the secondary SEI (as fewer ions can reach the electrode interior and instead react or deposit), becoming a self-reinforcing cycle.

At stage 3, which is the last several hundreds of cycles, the SEI with a thickness of 1.5  $\mu\text{m}$  on the anode surface, accounts for about 1.5% thickness of the pristine anode and the partial delamination of cathode then happens at the center location. Some of the cathode at the center delaminated and lost electronic contact during long-term cycling so that this material was not as fully used as the cathode at the material at the side locations, resulting in less loss of its electrochemical capacity as suggested by the area-specific coin cell testing. Moreover, even after complete discharging of the 18650 cell before tear-down, there was still a significant difference in the level of lithiation between the cathode materials depending on location, also consistent with the concept that the some of the cathode at the center lost electronic contact during cycling. These findings also allow us to rule out a mechanism wherein the cathode located in the center region was cycled more heavily, since this doesn't match the results in Figure 5-9 (b, c), where the harvested cathode materials from the side regions actually provided lower capacities than the cathode material at the center.

## 5.5 Conclusion

Commercial 18650 cells were tested under different cycling conditions and were disassembled for post-mortem study. Comprehensive characterization and analyses suggest that the aging level of cathode materials is closely related to the cycling conditions of cell, and that in some cases the cathodes aged very differently as a function of position in the cell/electrode. We suggest that in order to better evaluate the aging level of cathode materials, cell cycling condition, cell aging mechanism and inhomogeneous aging need to be taken into consideration. We find that it cannot be concluded that all of the cathode material within a cell is in the same condition/state of

lithiation, since some of it could be in an area that was under cycled due to the formation of secondary SEI. We proposed a mechanism based on the evolution of internal mechanical pressure to describe the observed effects based on the inhomogeneous evolution of this SEI on the anode and the electrochemical and mechanical implications of this layer. To prove/disprove the proposed mechanism, we suggest that techniques, such as in-situ X-ray computed tomography (CT) scanning <sup>71,76</sup>, should be used in the future to non-destructively detect the effect of mechanical stress inside 18650 cell while the cell is cycling.



# Chapter 6. Towards Practical Application of Direct Relithiation of Aged Cathode: Effect of Process Variables and Contaminant

## 6.1 Overview

Now that we know the difference in the aged cathode properties, the next step is to understand how to deal with these differences through the recycling process and get consistent recycled product. To do that, we first need to understand the effect of the various recycling process parameters on the recycled product. This chapter is going to investigate the effect of three process variables on the recycling cathode active materials using solid-state approach. The three variables are: lithium source type ( $\text{Li}_2\text{CO}_3$  or  $\text{LiOH}$ ), aged cathode to lithium source molar ratio, and graphite anode content. Furthermore, the potential mechanism behind the effect of each variable will be discussed. The reasons that these three variables are picked up among other process variables is to reduce the cost of recycling cost. Based on the cost model of the direct recycling<sup>2</sup>, the cost of lithium source used in the direct recycling has a big effect on the overall cost of recycling process.  $\text{Li}_2\text{CO}_3$  has the similar price to  $\text{LiOH}$  in term of \$/kg of Li but requires high temperature during calcination process. The optimized ratio of lithium source to aged cathode ratio can reduce the amount of lithium source used. As for graphite content, the collection of “pure” aged cathode materials is done by separating it from anode materials, which is mostly graphite. Currently, the separation efficiency is less than 90% at larger scale, meaning the cathode materials collected after the separation has more than 10% anode. To further

increasing the separation efficiency, multiple separation steps are needed, which increases the overall cost of recycling process. Here, we try to investigate the effect of graphite content on the recycled product in order to find the optimal point between cost and recycled product performance.

#### Hypotheses:

- Relithiation of aged cathode material can be done by using  $\text{Li}_2\text{CO}_3$  or  $\text{LiOH}$ .
- For the aged cathode active materials from 18650 cell [CC, 25 °C], an optimal molar ratio of Lithium source to the aged cathode, in the range between 0.5:1 and 3:1, will be found to get relithiated product with the highest electrochemical capacity, when other process variables are the same.
- Graphite will reduce the metal-ion during calcination process to create a reduced phase on the surface of relithiated cathode and cause the decreasing of capacity.

## 6.2 Experimental

The aged cathode acquirement procedure was described in Chapter 3 after the 1000 cycles. The collected aged cathode materials from 18650 cell [CC, 25 °C] will be used as source of aged cathode materials.

### 6.2.1 Direct recycling process via solid-state method

The recycling process was composed of two calcination steps. Before the first calcination, aged NCA cathode powder and Lithium source were mixed using mortar & pestle for 10 min in the air. Graphite, if needed, was added to the mixture powder and mixed again using mortar & pestle

for 10 min. The total mass for the mixture powder was around 200 mg. Then under O<sub>2</sub> flow rate 60 sccm, the mixture was heated at 480°C for 3h with rate of a 10°C/min for heat-up and cool-down. After the first calcination step, the mixture was taken out and re-mixed using mortar & pestle for 10 min. Then under O<sub>2</sub> flow rate 60 sccm, the mixture was heated at 730°C for 12h with a rate of 10°C/min for heat-up and cool-down. The crucibles used in the heating step are aluminum crucible with a volume of 5mL. In this paper, three factors have been investigated: type of lithium source, the molar ratio of aged cathode to lithium source, and w% of graphite contaminant in the aged cathode.

- Type of lithium source: LiOH and Li<sub>2</sub>CO<sub>3</sub>, are chosen based on the cost and the environmental effect of side product.
- Molar ratio of aged cathode to lithium source: for simplicity, we assume that the mass of aged NCA cathode powder equals to mass of aged NCA active materials (though in reality the binder and conductive filter took up ~5% mass based on TGA) and that the stoichiometry of aged NCA cathode active materials is the same as fresh NCA active materials (1 lithium-ion per NCA). Four different molar ratio, 0.5:1, 1:1, 2:1, and 3:1 were investigated. For example, the molar mass of aged NCA is 183 g/mol. The molar mass of LiOH\*H<sub>2</sub>O is 42 g/mol. The mass of NCA is weighted as X, the mass of LiOH\*H<sub>2</sub>O is  $\frac{X*42}{183} * \frac{1}{0.5}$  (*ratio*), if 0.5:1 ratio is used.
- Graphite content: note that there is around 2-3 wt% conductive filler, such as carbon black in the aged cathode and the graphite wt% is against total mass of aged cathode. Graphite with 0 wt%, 3 wt% and 6 wt% of the total mass of aged NCA cathode powder were investigated. The graphite used has a purity of 99% with the particle size of 44 micrometer (50-70%).

### 6.2.2 Sample Naming

In this chapter, fresh cathode materials will be referred as Fresh NCA. The collected aged cathode materials from 18650 cell [CC, 25 °C] will be referred as aged NCA. The base-line of the recycling process will use the following condition: LiOH as lithium source, 1:1 molar ratio of age cathode to LiOH and no graphite added. The product of the base-line relithiation process will be referred as R-NCA. When one of the factors is changed, the name of the product will be R-NCA-changed condition. For example, if  $\text{Li}_2\text{CO}_3$  was used instead of LiOH, the product will be referred as R-NCA- $\text{Li}_2\text{CO}_3$ . If 3% graphite was added, the product will be referred as R-NCA-3% graphite.

### 6.2.3 Characterization

Both physical, including XRD and XPS, and electrochemical characterization, such as GCPL, follow the procedure described in Chapter 3.

## 6.3 Result

Figure 6-1 shows XRD patterns of fresh NCA, aged NCA, R-NCA after 1<sup>st</sup> and 2<sup>nd</sup> calcination and R-NCA- $\text{Li}_2\text{CO}_3$  after 1<sup>st</sup> and 2<sup>nd</sup> calcination. Fresh NCA shows hexagonal layered phase in the R-3mspace group ( $\alpha$ -NaFeO<sub>2</sub>-type structure) with typical twin-peak shape for (108) peak and (110) peak. For aged NCA, the structure remains but the (003)/(104) peak ratio is lower than fresh NCA. Moreover, the separation of (108) peak and (110) peak suggests a lower level of lithiation in structure due to the change in the lattice parameters. For both R-NCA and R-NCA- $\text{Li}_2\text{CO}_3$  after 1<sup>st</sup> calcination, the layered structure remains, but there is merging of (108)

peak and (110) peak. Also, they both show a sign of peak for  $\text{Li}_2\text{CO}_3$  [00-0830145], as suggested by black dashed lines. For both R-NCA and R-NCA\_ $\text{Li}_2\text{CO}_3$  after 2<sup>nd</sup> calcination, the layer structure still remains and the twin-peak shape of (108) and (110) is back but not completely for R-NCA\_ $\text{Li}_2\text{CO}_3$ . They both show the peaks from impurity phases of  $\text{Li}_2\text{CO}_3$  but the R-NCA\_ $\text{Li}_2\text{CO}_3$  also shows the peaks from impurity phases of  $\text{Li}_4\text{AlO}_5$  [00-0270-209] with much high intensity, suggested by the orange dash line.

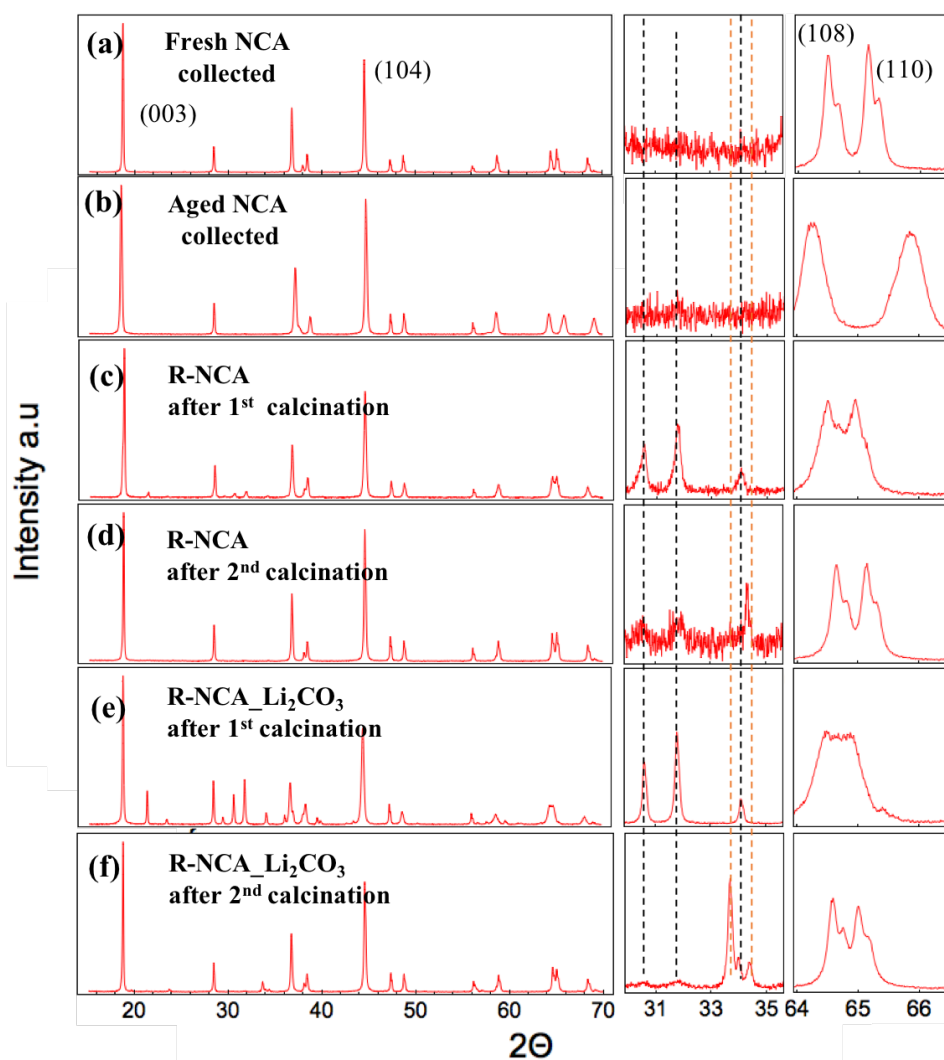


**Figure 6-1.** XRD patterns of (a) fresh NCA, (b) aged NCA, (c-d) R-NCA after 1<sup>st</sup> and 2<sup>nd</sup> calcination, (e-f) R-NCA\_Li<sub>2</sub>CO<sub>3</sub> after 1<sup>st</sup> and 2<sup>nd</sup> calcination. The black dash lines stand for peaks location of Li<sub>2</sub>CO<sub>3</sub> and the orange dash lines stand for peaks location of Li<sub>4</sub>AlO<sub>5</sub>

Figure 6-2 shows the shows XRD patterns of R-NCA\_3% graphite and R-NCA\_6% graphite after 1<sup>st</sup> and 2<sup>nd</sup> calcination. In general, all four samples still show the layer structure mainly and peaks from impurity phases of Li<sub>2</sub>CO<sub>3</sub> other than of R-NCA\_3% graphite after 2<sup>nd</sup> calcination. For R-NCA\_3% graphite after 2<sup>nd</sup> calcination, it shows the peaks from impurity phases of Li<sub>4</sub>AlO<sub>5</sub>.

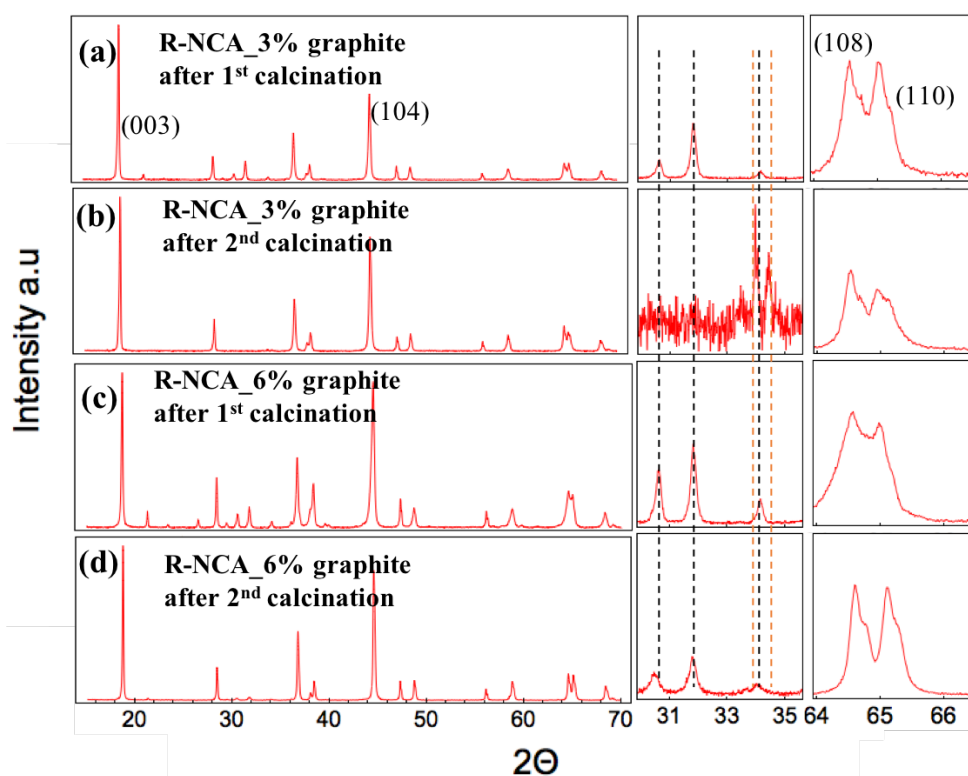


**Figure 6-2.** XRD patterns of (a-b) R-NCA\_3% graphite after 1<sup>st</sup> and 2<sup>nd</sup> calcination and (c-d) R-NCA\_6% graphite after 1<sup>st</sup> and 2<sup>nd</sup> calcination. The black dash lines stand for peaks location of Li<sub>2</sub>CO<sub>3</sub> and the orange dash lines stand for peaks location of Li<sub>4</sub>AlO<sub>5</sub>

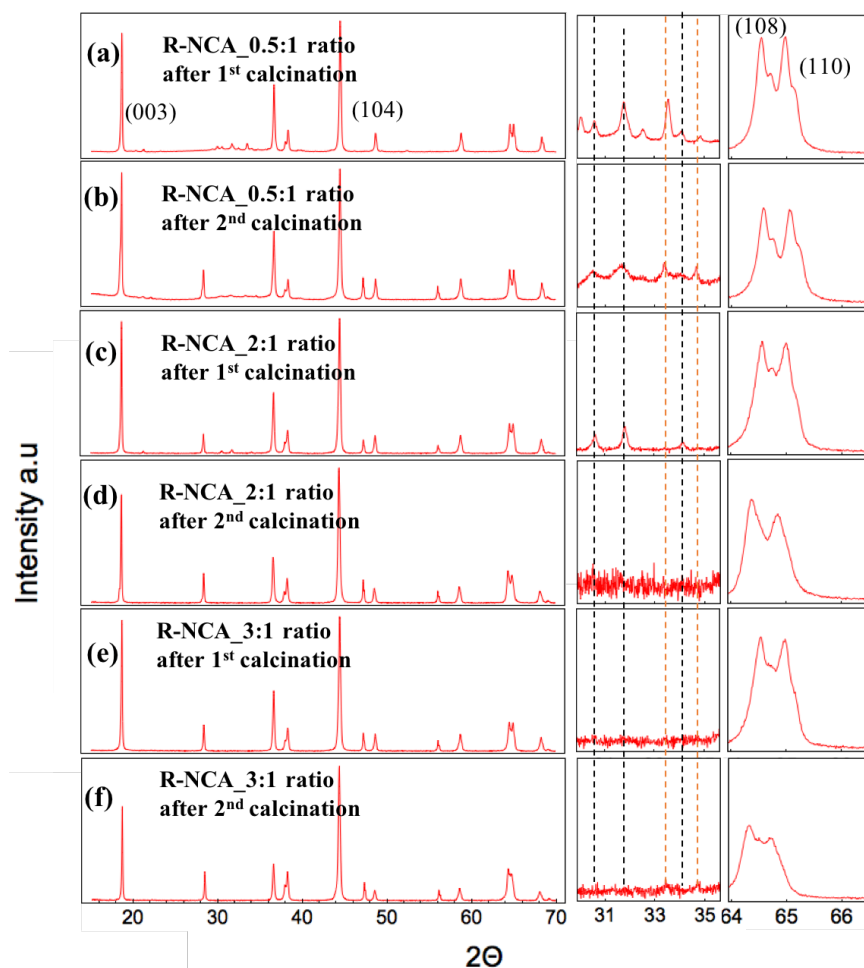


**Figure 6-3.** XRD patterns of (a-b) R-NCA\_0.5:1 ratio after 1<sup>st</sup> and 2<sup>nd</sup> calcination, (c-d) R-NCA\_2:1 ratio after 1<sup>st</sup> and 2<sup>nd</sup> calcination and (e-f) R-NCA\_3:1 ratio after 1<sup>st</sup> and 2<sup>nd</sup> calcination. The black dash lines stand for peaks location of  $\text{Li}_2\text{CO}_3$  and the orange dash lines stand for peaks location of  $\text{Li}_4\text{AlO}_5$

Figure 6-3 shows the XRD patterns of R-NCA, R-NCA\_2:1 ratio and R-NCA\_3:1 ratio after 1<sup>st</sup> and 2<sup>nd</sup> calcination. After 1<sup>st</sup> calcination, the twin-peak shape remains for the three conditions but the peaks from impurity phases for  $\text{Li}_2\text{CO}_3$  decreases with a lower ratio of LiOH (less LiOH per NCA). After 2<sup>nd</sup> calcination, the level of the merging of twin peaks increases with a lower ratio of LiOH.

Table 6-1. Lattice parameter c-axis calculated based on Si peak correction			
Sample Name	c (nm)	Sample Name	c (nm)
Aged NCA	$1.437 \pm 0.002$	R-NCA_2:1 ratio after 1 <sup>st</sup> calcination	$1.418 \pm 0.002$
Commercial NCA powder	$1.419 \pm 0.002$	R-NCA_2:1 ratio after 2 <sup>nd</sup> calcination	$1.422 \pm 0.002$
R-NCA after 1 <sup>st</sup> calcination	$1.419 \pm 0.002$	R-NCA_3:1 ratio after 1 <sup>st</sup> calcination	$1.419 \pm 0.002$
R-NCA_Li <sub>2</sub> CO <sub>3</sub> after 1 <sup>st</sup> calcination	$1.417 \pm 0.002$	R-NCA_3:1 ratio after 2 <sup>nd</sup> calcination	$1.423 \pm 0.002$
R-NCA after 2 <sup>nd</sup> calcination	$1.420 \pm 0.002$	R-NCA_3% graphite after 1 <sup>st</sup> calcination	$1.419 \pm 0.002$
R-NCA_Li <sub>2</sub> CO <sub>3</sub> after 2 <sup>nd</sup> calcination	$1.418 \pm 0.002$	R-NCA_3% graphite after 2 <sup>nd</sup> calcination	$1.420 \pm 0.002$
R-NCA_0.5:1 ratio after 1 <sup>st</sup> calcination	NA	R-NCA_6% graphite after 1 <sup>st</sup> calcination	$1.421 \pm 0.002$
R-NCA_0.5:1 ratio after 2 <sup>nd</sup> calcination	NA	R-NCA_6% graphite after 2 <sup>nd</sup> calcination	$1.420 \pm 0.002$

**Table 6-1.** the calculated value for c-axis of NCA layered structure based on the Si peak correction.

Figure 6-4 shows XPS spectra of O 1s, F 1s and Ni 2p of all the samples. In general, O 1s spectra of different samples have two peaks other than R-NCA\_Li<sub>2</sub>CO<sub>3</sub>, with no peak at lower binder energy. For fresh cathode and aged cathode, these two peaks are at 530.67 eV and 528.31 eV while for all recycled product, the location for both peaks is slightly shifted towards higher binder energy, around 530.6 eV and 529.1 eV. In term of relative intensity for the peak at lower binding energy (around 529 eV) in O 1s, R-NCA\_Li<sub>2</sub>CO<sub>3</sub> didn't have it at all and R-NCA\_6% graphite and R-NCA\_3% graphite show the small peak while the other samples show the peak much higher intensity. In F 1s spectra, in general, all the samples, other than the fresh and aged cathodes, show two peaks. The locations for these two peaks are at around 687.6 eV (F from PVDF binder) and 684.8 eV (F from LiF potentially) respectively. In Ni 2p spectra, all the



samples show typical peaks for Ni ions other than R-NCA\_Li<sub>2</sub>CO<sub>3</sub> in which no obvious Ni peak is shown.

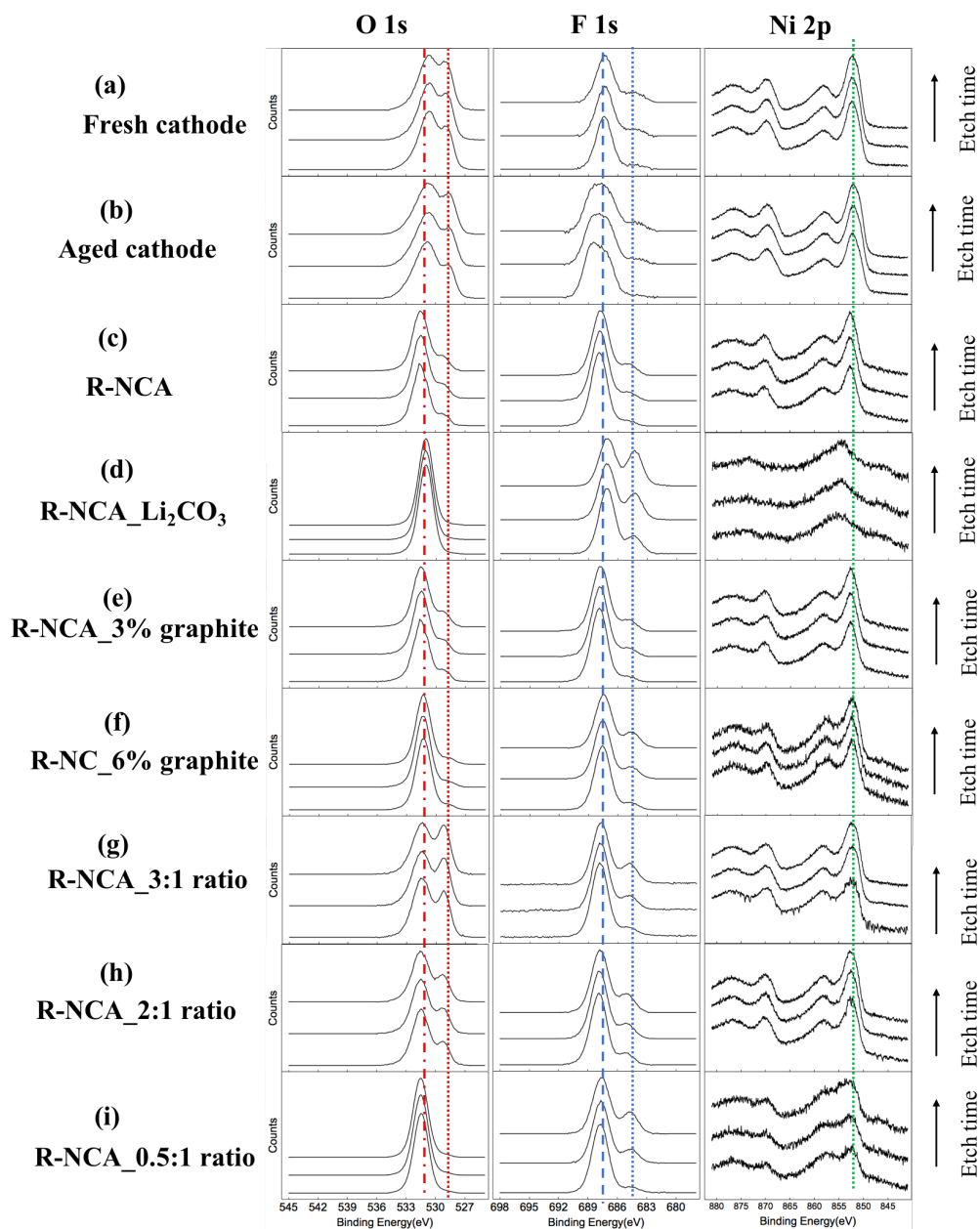


**Figure 6-4.** XPS spectra of O 1s, F 1s and Ni 2p for (a) fresh cathode, (b) aged cathode, (c) R-NCA, (d) R-NCA\_Li<sub>2</sub>CO<sub>3</sub>, (e) R-NCA\_3% graphite, (f) R-NCA\_6% graphite, (g) R-NCA\_3:1 ratio, (h) R-NCA\_2:1 ratio and (i) R-NCA\_0.5:1 ratio. In O 1s spectra, the red dashed and dot lines sit on 530.67 eV and 528.31 eV separately. In F 1s spectra, the blue dashed and dot lines sit on 687.71 eV and 684.74 eV separately. In Ni 2p spectra, the green line sits on 855.42 eV. The etch time per step is 40s.

Figure 6-5 shows the electrochemical capacity at 0.1 C rate of different samples. The NCA active materials mass is used for the calculation of the specific capacity. The fresh cathode and aged cathode show discharge capacity at around 170 mAh/g and 140 mAh/g respectively. In term of lithium source, R-NCA shows discharge capacity of 160mAh/g, which is higher than aged cathode but slightly lower than fresh cathode but R-NCA\_Li<sub>2</sub>CO<sub>3</sub> shows nearly no discharge capacity. In term of graphite content, the higher graphite content, the worse the

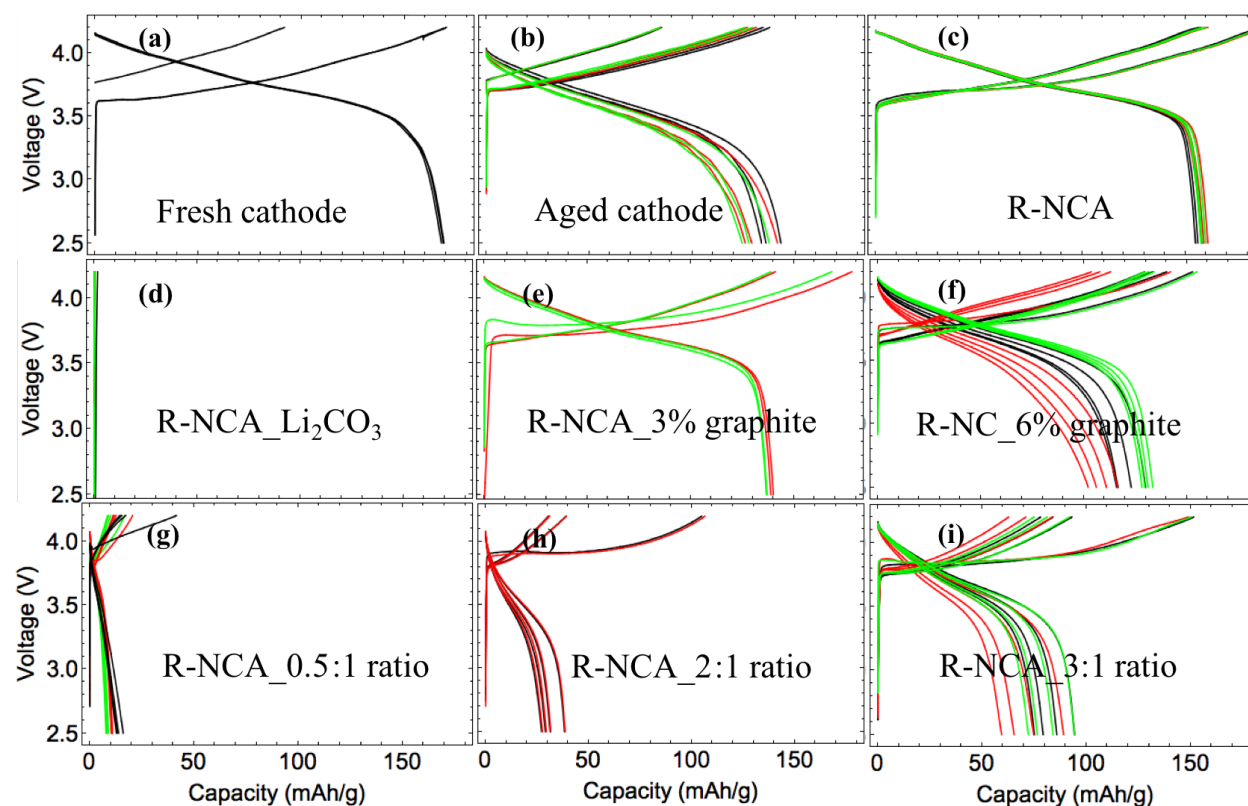


**Figure 6-5.** Comparison of the reference cycle of (a) fresh cathode, (b) aged cathode, (c) R-NCA, (d) R-NCA\_Li<sub>2</sub>CO<sub>3</sub>, (e) R-NCA\_3% graphite, (f) R-NCA\_6% graphite, (g) R-NCA\_0.5:1 ratio, (h) R-NCA\_2:1 ratio and (i) R-NCA\_3:1 ratio. For reference cycle, the coin cell is cycled at 0.1C rate for both charge and discharge with 2.5 V and 4.2 V voltage cut-off.

performance is. In term of the aged cathode to lithium source reactants ratio, when the ratio is  $\geq 1$ , the higher the ratio (less LiOH per NCA), the worse the performance. The data from R-NCA\_0.5:1 ratio is to be collected.

## 6.4 Discussion

In this section, we will discuss the results of the three process variables in three sub-sections.

### 6.4.1 Effect of lithium source

As shown in Figure 6-5 (c), R-NCA, which is the best result among all the conditions, show improvement of discharge capacity over aged cathode but still slightly lower than fresh cathode materials. Figure 6-5 (d) shows that R-NCA\_Li<sub>2</sub>CO<sub>3</sub> has even much worse performance than the aged cathode. To investigate the reason behind the two phenomena, three aspects are taken into consideration: bulk structure of NCA active materials, the near-surface structure of NCA active materials and surface layer on the NCA active materials. Firstly, XRD pattern of both samples in Figure 6-1 (d, f) shows that the bulk structure of both samples remains as layered structure. Based on twin-peak shape for (108) and (110),<sup>77-78</sup> Li/Ni ordering level is relatively the same in the bulk. But for that R-NCA\_Li<sub>2</sub>CO<sub>3</sub>, the peaks from impurity phases of Li<sub>4</sub>AlO<sub>5</sub> suggest decomposition of NCA to a certain degree. Secondly, O 1s spectra data in Figure 6-4 (c) shows that the peak at lower binder energy, which is from the metal-O bond, is shifted to higher binder energy when compared to the fresh cathode. Based on the previous paper, binder energy of metal-O bond is higher in the reduced surface layer, such as cubic NiO phase, than in layer structure phase (where Ni<sup>3+</sup> is present).<sup>79-80</sup> Thirdly, XRD pattern in Figure 6-1 (d,f) show the existent of the peaks from impurity phases of Li<sub>2</sub>CO<sub>3</sub> for both samples and Li<sub>4</sub>AlO<sub>5</sub> for R-

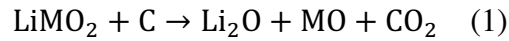
NCA\_Li<sub>2</sub>CO<sub>3</sub>. O 1s spectra of both samples shows peak at around 530.6 eV, which is likely to belong to the bond in Li<sub>2</sub>CO<sub>3</sub>. Moreover, since the analysis depth of XPS is between 3-10nm, the surface contaminant layer of R-NCA\_Li<sub>2</sub>CO<sub>3</sub> is thicker than the analysis depth and that of R-NCA is less than the analysis depth since the metal-O bond peak disappears in R-NCA\_Li<sub>2</sub>CO<sub>3</sub> while there is metal-O bond peak in R-NCA. For R-NCA\_Li<sub>2</sub>CO<sub>3</sub>, even after etching, there is still no peak for metal-O bond. With all the result we have above, the reasons that R-NCA didn't return to full capacity as fresh cathode could be: (1) near-surface layer is electrochemical resistant, though it is very thin; (2) the surface contaminant such as Li<sub>2</sub>CO<sub>3</sub>, though thin, is still electrochemical resistant. For R-NCA\_Li<sub>2</sub>CO<sub>3</sub>, the worst performance could be mostly due to the thick layer of contaminants on the surface, such as Li<sub>4</sub>AlO<sub>5</sub> and Li<sub>2</sub>CO<sub>3</sub>, which create high resistance.<sup>81</sup> So when comparing the two different lithium source during relithiation reaction, LiOH is better than Li<sub>2</sub>CO<sub>3</sub>. The reason could be that for Li<sub>2</sub>CO<sub>3</sub>, the activation energy is higher than that of LiOH, which means that the kinetics of relithiation process is slower when reacting with Li<sub>2</sub>CO<sub>3</sub>. Also, LiOH is in the form of molten salt during the 1<sup>st</sup> calcination (melting point is around 460°C) while Li<sub>2</sub>CO<sub>3</sub> is still solid. Molten salt/solid would have better contact than solid/solid so that the reaction is more homogeneous when using LiOH as the reactant.

#### 6.4.2 Effect of graphite content

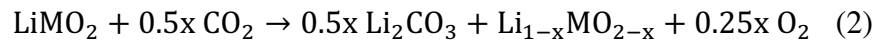
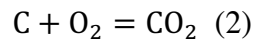
Based on Figure 6-5 (c, e, f), the general trend is that the higher the graphite content in reactants mixture, the worse the electrochemical performance of the recycled product has. Three aspects of factors as-above are considered to analyze the data. Firstly, XRD patterns of the three samples in Figure 6-1 (d) and Figure 6-2 (b,d) show that the bulk structure of the samples remains as layered structure, though R-NCA\_3% graphite shows slightly higher Li/Ni disordering as suggested by

the merging of twin-peaks (108) and (110). Secondly, O 1s spectra data in Figure 6-4 (e, f) show that the peak for metal-O bond is shifted to higher binder energy when compared to the fresh cathode which is a sign of reduced surface layer as we mentioned in part 1. Thirdly, R-NCA\_6% graphite shows much high intensity of the impure peak of  $\text{Li}_2\text{CO}_3$  than the other two samples in XRD pattern and lower the metal-O bond in XPS O 1s spectra. These two phenomena suggested that the surface contaminant layer of R-NCA\_6% graphite, containing more  $\text{Li}_2\text{CO}_3$  relatively, is thicker than that of the other two samples. Based on the result above, the effect of graphite content during relithiation process could be that during the 2<sup>nd</sup> calcination,  $\text{Ni}^{3+}$  at the surface layer of NCA materials is reduced to  $\text{Ni}^{2+}$  by graphite so that a reduced surface layer is formed. Based on the previous publications, there are two paths of the reaction:<sup>82-84</sup> (1) graphite directly reacts with NCA active materials; (2) graphite firstly react with  $\text{O}_2$ , forming  $\text{CO}_2$  which further reacts with NCA active materials. (M here stands for metal element including Ni, Al, Co).

Path 1:



Path 2:

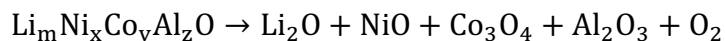


The exact path of reaction during relithiation is beyond the scope of this chapter. But whichever the path, the side products are reduced phase and  $\text{Li}_2\text{CO}_3$ , which explains the higher intensity of  $\text{Li}_2\text{CO}_3$  for R-NCA\_6% graphite. These two side products are electrochemical resistant, causing lower capacity.<sup>82, 84</sup> Although R-NCA\_3% has higher Li/Ni disordering level, it might not play as important role as the two side products mentioned above, though the exact reason for the higher level of disordering is unknown so far.

#### 6.4.3 Effect of molar ratio of aged cathode active materials to lithium source

The general goal for this section is to understand whether the optimal ratio of aged cathode active materials to lithium source exists or not, with which the recycled cathode shows best electrochemical performance. To do so, we firstly would pick the ratio number at the boundary where the lithium source is over-amount (0.5:1 ) and less-amount (3:1) and then narrow down the boundary. Based on Figure 6-5 (c, h, i), the general trend is that when the ratio is  $\geq 1$ , the higher the ratio (less LiOH per mol of NCA), the worse the electrochemical performance of relithiated product shows. Three aspects of factors as-above are considered to analyze the data. Firstly, XRD pattern of the three samples in Figure 6-3 (b, d, f) show that the bulk structure of the samples remains as layered structure. But R-NCA\_2:1 and R-NCA\_3:1 show high Li/Ni disordering as suggested by the merging of twin-peaks (108) and (110). Secondly, O 1s spectra data in Figure 6-4 (g, h) show that the peak for metal-O bond in R-NCA\_2:1 and R-NCA\_3:1 is shifted to higher binder energy when compared to the fresh cathode which is a sign of reduced surface layer as we mentioned in part 1. Thirdly, R-NCA\_2:1 and R-NCA\_3:1 shows relatively high intensity of metal-O bond when compared with the bond from  $\text{Li}_2\text{CO}_3$ , suggesting that surface contamination layer is thinner for these two samples when compared with R-NCA. With the result above, the effect of reactant ratio (when  $\geq 1$ ) during relithiation process could be explained through disordering/decomposition reaction vs relithiation reaction. The background information in 2.2.5.1 shows the disordering/decomposition reaction to start at temperature lower than  $200^\circ\text{C}$  and the set-on temperature varied depending on the level of lithiation and other factors, such as oxygen partial pressure. The TGA result of aged cathode used in this case shows that the

disordering/decomposition reaction starts at around 210°C. During the calcination process, two types of reaction compete with each other, disordering/decomposition reaction vs relithiation reaction. The lower the level of lithiation and the higher temperature, the faster rate the disordering/decomposition reaction has. For relithiation reaction, higher temperature and higher concentration of lithium source lead to a higher rate. So, to reduce the disordering/decomposition reaction, it is better to have high level of lithiation of NCA during calcination processes, especially 2<sup>nd</sup> one with high temperature. In the cases of R-NCA\_2:1 and R-NCA\_3:1, where the amount of available LiOH per NCA is low, lithium-ion can't diffuse into the structure (relithiation reaction) fast enough so that the decomposition or disordering reaction of NCA dominate. The decomposition product, based on the previous result,<sup>58</sup> should be NiO-like compound mainly along with other side products, as shown by the equation below. We haven't detected NiO phase in XRD pattern, potentially due to the amount is too low. But we do see the NiO-like phase peak in O 1s spectra.



Based on Figure 6-5 (c, g), the general trend is that when the ratio is  $\leq 1$ , the smaller the ratio (more LiOH per mol of NCA), the worse the electrochemical performance of relithiated product shows. XRD result in Figure 3 (b) and XPS result in Figure 6-4 (i) suggest that there is layer of materials, potentially composed of  $\text{Li}_4\text{AlO}_5$  and  $\text{Li}_2\text{CO}_3$ , on the surface of R-NCA\_0.5:1 ratio material, creating high electrochemical resistance. This is very similar to the R-NCA\_ $\text{Li}_2\text{CO}_3$  samples. The difference here is that the reason to causes formation of  $\text{Li}_4\text{AlO}_5$  is not due to the improper mixing of  $\text{Li}_2\text{CO}_3$  and aged NCA, but due to the excess available of LiOH per aged NCA.

One more point that is worth discussion. In the F 1s spectra of all the samples, there is one peak at around 685 eV, which potentially comes from LiF. For all the recycled product, the relative intensity from LiF increases with more etching during XPS. The source of LiF is not clear. It could be from the decomposition product of  $\text{LiPF}_6$  (salt in the electrolyte) or the reaction of SEI on the cathode surface with lithium source during the calcination. Also, the effect of LiF is not clear. It seems that LiF covers NCA active materials but doesn't cause high resistance as  $\text{Li}_2\text{CO}_3$ .

## 6.5 Conclusion

In general, the effect of three process variables of solid-state recycling approach on the recycled product has been investigated.

- For the type of lithium source, using LiOH as the source of lithium shows a better result than  $\text{Li}_2\text{CO}_3$ , potentially due to better contact of reactants and lower activation energy, though both lithium source can relithate the aged cathode materials during the calcination process.
- Graphite content shows a negative effect on the final product due to the reduction effect of graphite on the Ni-ion on the surface to form NiO-like phase.
- As for the reactant ratio, when the ratio is  $\geq 1$ , the higher the ratio (less LiOH per mol of NCA), the worse the electrochemical performance of relithiated product shows. The lower LiOH content causes a lower rate of relithiation reaction. Therefore, disordering/decomposition reaction dominates and cause the decreasing of electrochemical capacity. When the ratio is  $\leq 1$ , the higher the ratio (less LiOH per mol of NCA), the better the electrochemical performance of relithiated product. The excess



LiOH causes impurities such  $\text{Li}_2\text{CO}_3$  and  $\text{Li}_4\text{AlO}_5$ , creating high electrochemical resistance.

The result in this chapter would contribute to optimizing the relithiation of aged NCA and reducing the cost of recycled NCA. Further, the conclusion could be applied to other layered structure commercial cathode materials, such as  $\text{Li}(\text{Ni}_x\text{Co}_y\text{Mn}_z)\text{O}_2$  ( $x+y+z=1$ ) NCM cathode materials.

# Chapter 7. Effect of properties of aged cathode active materials on recycled product

## 7.1 Overview

Aged NCA materials collected from different sources have inhomogeneous properties. For direct recycling, it is crucial to prove that the direct recycling process can handle the aged NCA materials with inhomogeneous properties in one batch and produce consistent recycled NCA. The aged NCA collected from cells cycled under different condition shows more than just one difference in properties. It is hard to understand which process parameter is important to deal with certain difference in aged NCA properties. In this paper, we will investigate the direct recycling process factors that address the effect of three properties of aged  $\text{LiNi}_{8.15}\text{Co}_{1.5}\text{Al}_{0.35}\text{O}_2$  (NCA) materials: variation of state-of-charge (SoC) of the aged NCA, the existence of a surface reconstruction layer within the aged NCA, and the growth of the solid electrolyte interface (SEI) on the aged NCA. We will explore how each property impacts the consistency of the recycled NCA in terms of several key materials properties.

Hypotheses:

- Under the same relithiation process parameter, the aged cathode with high level of lithiation will have product with better electrochemical performance.
- Under the same relithiation process parameter, the aged NCA with thin SEI will have product with better electrochemical performance.

- Under the same delithiation process parameter, the aged NCA with lower content of surface reconstruction phases will have product with better electrochemical performance.

## 7.2 Experimental

### 7.2.1 Preparation of materials

#### 7.2.1.1 Preparation of NCA with different SoC

The pristine NCA (NCA<sub>p</sub>) with the composition (Ni: Co: Al=8.15: 1.5: 0.35) was purchased from MTI corporation. Br<sub>2</sub> with 99.99% purity from Sigma was used for chemical delithiation of the pristine NCA. The more delithiation the NCA has, the higher its SoC. For the preparation of the NCA with a higher level of SoC, 400 mg of NCA was added to 40 mL acetonitrile solvent in the beaker and stirred for 5 min. Then 40  $\mu$ L oBr<sub>2</sub> was added to the mixture solution and stirred overnight. All the steps were done in the glovebox filled with Ar gas and the O<sub>2</sub> content was less than 2 ppm. Next, the mixture was transferred out and the delithiated NCA was separated from the solution by centrifuge. The delithiated NCA was washed with 20 mL acetonitrile solvent and separated by centrifuge again. The washing process was repeated 3 times to make sure the residual Br<sub>2</sub> and any other by-products of the reaction were washed away. Finally, the delithiated NCA was dried under vacuum at 60°C overnight. The prepared delithiated NCA materials with a high level of SoC was named NCA<sub>HSoC</sub>. To prepare the delithiated NCA materials with a low level of SoC, the same procedures were used other than that the volume of Br<sub>2</sub> was 10  $\mu$ L instead of 40  $\mu$ L. The name for the delithiated NCA materials with a low level of SoC was NCA<sub>LSoC</sub>.

#### 7.2.1.2 Preparation of NCA with different level of structure transformation

To prepare NCA materials with different levels of structure transformation,  $\text{NCA}_{\text{HSoC}}$  was treated under different temperatures. To prepare NCA materials with a high level of structure transformation,  $\text{NCA}_{\text{HSoC}}$  was transferred into the tube furnace with constant  $\text{O}_2$  flow (60 scsm). The heating process was: from room temperature to  $650^\circ\text{C}$  with a rate of  $10^\circ\text{C}/\text{min}$ , hold at  $650^\circ\text{C}$  for 3h, cool down to room temperature with a rate of  $10^\circ\text{C}/\text{min}$ . The prepared material was named  $\text{NCA}_{\text{HSoC\_}650^\circ\text{C}}$ . To prepare NCA materials with a low level of structure transformation, the same procedure as above was used other than the temperature was  $350^\circ\text{C}$  instead of  $650^\circ\text{C}$ . The prepared material was named  $\text{NCA}_{\text{HSoC\_}350^\circ\text{C}}$ .

#### 7.2.1.3 Preparation of NCA with SEI

To prepare NCA with SEI formed on the surface, 400 mg of  $\text{NCA}_{\text{HSoC}}$  was submerged in 20 mL electrolyte (DEC:EC=1:1, 1M  $\text{LiPF}_6$ ) for 14 days. Then the post-treated NCA was separated from electrolyte by centrifuge and then rinsed with DEC solvent twice to wash away residual electrolyte. Then, the materials were dried under vacuum at  $60^\circ\text{C}$  overnight. The prepared sample was named  $\text{NCA}_{\text{HSoC\_Electrolyte\_14d}}$ .

<b>Table 7-1. Naming of samples in this chapter</b>	
[1] NCA with high level of SoC by chemically delithiation	$\text{NCA}_{\text{HSoC}}$
[2] NCA with low level of SoC by chemically delithiation	$\text{NCA}_{\text{LSoC}}$
[3] NCA with high level of SoC [1] treated under $350^\circ\text{C}$ for 3h	$\text{NCA}_{\text{HSoC\_}350^\circ\text{C}}$
[4] NCA with high level of SoC [1] treated under $650^\circ\text{C}$ for 3h	$\text{NCA}_{\text{HSoC\_}650^\circ\text{C}}$

[5] NCA with high level of SoC [1] treated with electrolyte for 14d	$\text{NCA}_{\text{HSoC\_Electrolyte\_14d}}$
Recycled product using any above-mentioned samples (This refers to final product after 2 <sup>nd</sup> sinter process and wash step unless otherwise specified)	R-sample name (one of the above)

### 7.2.2 Recycling of prepared NCA materials

For the recycling of the prepared NCA, the general procedures were that (1) the prepared NCA sample and  $\text{LiOH}\cdot\text{H}_2\text{O}$  were weighted with 1: 1 molar ratio; (Note: NCA samples have different molar mass due to loss of Lithium or Oxygen. The molar mass of NCA used for weighing was based on the composition  $\text{LiNi}_{0.815}\text{Co}_{0.15}\text{Al}_{0.035}\text{O}_2$  regardless of its actual compositional changes just for the convenience of calculation.) (2) mixture of NCA sample and  $\text{LiOH}\cdot\text{H}_2\text{O}$  was transferred them into alumina crucible boat; (3) the 1<sup>st</sup> heat treatment under  $\text{O}_2$  flow from room temperature to 480°C with a heating and cooling rate of 10 °C/min and hold at 480°C for 3h; (4) took out the mixture and re-mixed again; (5) the 2<sup>nd</sup> heat treatment under  $\text{O}_2$  flow from room temperature to 730°C with a heating and cooling rate of 10 °C/min and hold at 730°C for 12h. Some of the samples were heated at 730°C for 24h. (6) took out the sample, washed it with water, and dried it under vacuum. This step was skipped for some samples and will be indicated by the sample legend in the figures. To make the naming easier, we use “R” for samples having been recycled. For example, if the prepared NCA sample was  $\text{NCA}_{\text{HSoC}}$ , the recycled product of it after going through the above-mentioned procedures was named R- $\text{NCA}_{\text{HSoC}}$ .

### 7.2.3 Characterization of materials

#### 7.2.3.1 Thermo-gravimetric (TG) analysis (TGA)

The sample with around 10mg mass was weighed and transferred into the TGA instrument. TGA was carried out on SDT Q600. The heating procedure for TGA was: (1) jump to 120°C and hold for 20min; (2) heat from 120°C to 700°C with a heating rate of 5min/°C; (3) cool down. The TGA test was done under O<sub>2</sub> flow with a rate of 100 mLmin<sup>-1</sup>.

#### 7.2.3.2 X-ray Diffraction (XRD)

Silicon powder (99% purity) with 10wt% of the total sample mass was mixed with the prepared NCA sample for peak correction. XRD patterns of samples were characterized on a PANalytical X'pert diffractometer with a Cu K $\alpha$  radiation with a scan range from 15—70° 2 $\theta$ . Three scans were collected per sample for better resolution quality.

#### 7.2.3.3 X-ray photoelectron spectroscopy (XPS)

XPS was performed using an ESCALAB 250Xi X-ray photoelectron spectrometer microprobe, with a 650  $\mu$ m spot size. Elements were analyzed using monochromatic Al K $\alpha$  (1486.6 eV) radiation as the primary excitation source. For the etching step, 3kV voltage was used and etch time was 40 s per step.

#### 7.2.3.4 Transmission electron microscopy (TEM)

Samples were prepared through suspending 5 mg of active material powder in 20 ml et-OH, then sonicating for at least 1 hour before allowing the solution to settle for ~3 hours, after a pipette was filled with solution from the middle of the vial and 10 drops were deposited onto the Ted

Pella copper grid and allowed to dry in a fume hood overnight. TEM imaging and electron diffraction patterns were done using a FEI Tecnai F20 Field Emission Transition Electron Microscope. A Dual tilt stage was used to hold the samples. The microscope was set to the high-tension accelerating voltage of 200 kV, with spot size 1, alignment followed standard procedures as outlined in the Tecnai user manual. Images were taken in brightfield mode.

#### 7.2.3.5 Electrochemical test

Electrode preparation:

NCA active materials, carbon black and Polyvinylidene fluoride (PVDF) powder were weighed with a weight ratio of 9:0.5:0.5 and N-methyl-2-pyrrolidone (NMP) was gradually added into the mixture to make a black slurry. Then the black slurry was screened onto Al foil using the doctor blade and the aluminum foil was transferred into a vacuum oven and held at 80°C overnight.

Coin cell assembly:

The prepared electrode was paired with Li foil in the 2032 coin cell. The Celgard battery separator and commercial electrolyte (1 M LiPF<sub>6</sub> in 1:1 ethylene carbonate (EC): diethyl carbonate (DEC)) from Sigma were used. For each sample, three coin cells were made for repeatability

Coin cell test:

The coin cell was rested for 4h before start cycling. The cycling condition for the reference cycle was a 0.1C rate current (using 180mAh/g as theoretical capacity) for both charge and discharge with 2.5 V and 4.2 V voltage cut-off. For each coin cell, four reference cycles were conducted. All the reference cycle tests were conducted at 25°C.

## 7.3 Result and discussion part

### 7.3.1 Preparation of materials for recycling

Pristine NCA was chemically delithiated by  $\text{Br}_2$  with different concentrations in order to get NCA with different SoC. The XRD pattern in Figure 7-1 shows that after Silicon peak (111) correction, there was a shift in (003) peak to lower angle and split of twin-peak at around  $65^\circ$  for delithiated NCA ( $\text{NCA}_{\text{HSoC}}$  and  $\text{NCA}_{\text{LSoC}}$ ) when compared to  $\text{NCA}_{\text{P}}$  (space group  $\text{R}\bar{3}\text{m}$ ). These changes suggest that we did create NCA with different SoC.<sup>85-86</sup> Furthermore, the open-circuit-voltage (OCV) of coin cell using  $\text{NCA}_{\text{HSoC}}$  and  $\text{NCA}_{\text{LSoC}}$  as cathode materials shows different OCV, which again suggests that the difference in the SoC between  $\text{NCA}_{\text{HSoC}}$  and  $\text{NCA}_{\text{LSoC}}$ .

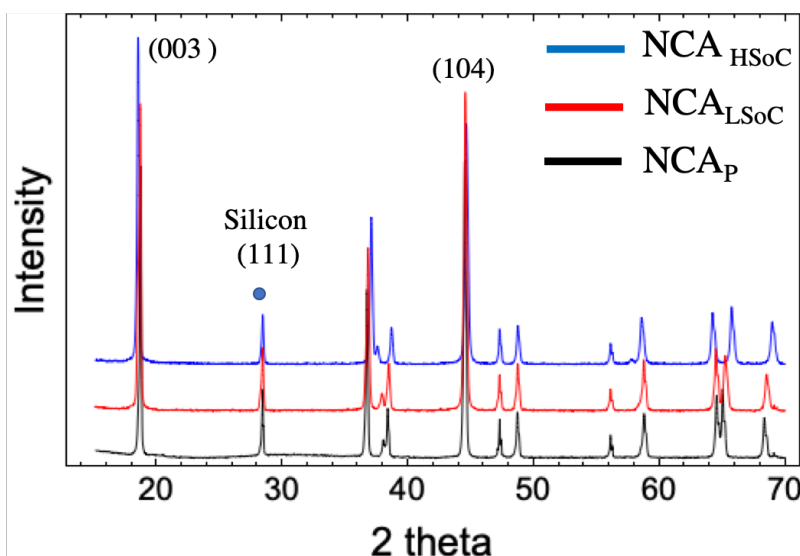


**Figure 7-1.** XRD of  $\text{NCA}_{\text{P}}$  and chemically delithiated NCA materials,  $\text{NCA}_{\text{HSoC}}$  and  $\text{NCA}_{\text{LSoC}}$ . (003) and (104) peaks from NCA materials are labeled. The blue dot is for Silicon (111) peak location which is used as reference point.



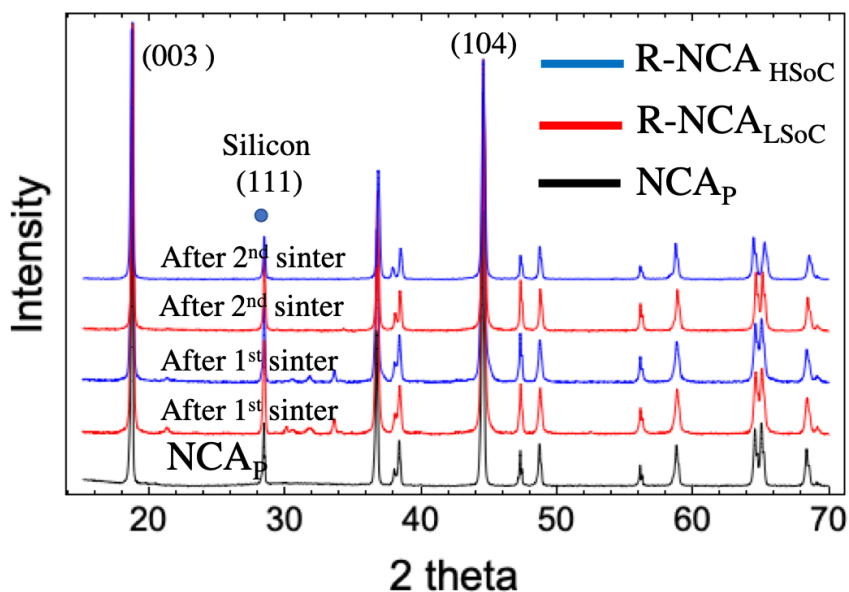


**Figure 7-2.** XRD of NCA<sub>P</sub> (black) and R-NCA<sub>HSoC</sub> (blue) and R-NCA<sub>LSoC</sub> (red) after 1<sup>st</sup> and 2<sup>nd</sup> sinter treatment.

(003) and (104) peaks from NCA materials are suggested. The blue dot is for Silicon (111) peak location which is used as the reference position for all the samples

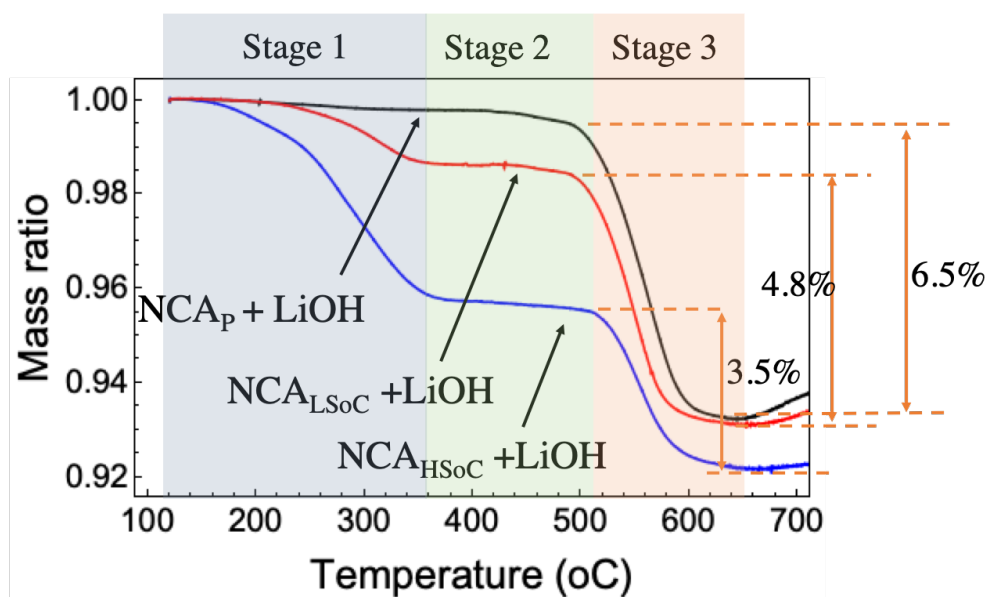


**Figure 7-3.** TGA of NCA<sub>HSoC</sub>, NCA<sub>LSoC</sub>, and NCA<sub>P</sub> with LiOH with 1:1 molar ratio from 120 °C to 700°C with heating rate 5 °C/min under O<sub>2</sub> flow. The mass after holding at 120°C for 20min is used as 1 for mass ratio calculation. During the holding step, the H<sub>2</sub>O in LiOH•H<sub>2</sub>O is removed.

<b>Table 7-2. Calculation of Lattice Parameter c</b>	
<b>Sample Name</b>	<b>Lattice c (nm)</b>
NCA <sub>p</sub>	1.419 ± 0.002
NCA <sub>LSoC</sub>	1.423 ± 0.002
NCA <sub>HSoC</sub>	1.436 ± 0.002
R-NCA <sub>LSoC</sub> after 1 <sup>st</sup> calcination	1.419 ± 0.002
R-NCA <sub>HSoC</sub> after 1 <sup>st</sup> calcination	1.421 ± 0.002
R-NCA <sub>LSoC</sub> after 2 <sup>nd</sup> calcination	1.420 ± 0.002
R-NCA <sub>HSoC</sub> after 2 <sup>nd</sup> calcination	1.420 ± 0.002

**Note:** the lattice parameter c is calculated based on the peak location of (003) after the peak location correction based on Silicon powder (111) peak location. The 0.002 error comes from the variance of Silicon powder (111) peak location from a 4-time repeated test.

### 7.3.2 Effect of difference SoC

#### Understanding of relithiation process

Before we discuss the effect of the difference in SoC of NCA materials on the recycled NCA, we wish to first understand the relithiation step. Figure 7-2 shows the XRD pattern of R-NCA<sub>HSoC</sub> and R-NCA<sub>LSoC</sub> after 1<sup>st</sup> sinter process which is at 480°C for 3h. The result suggests that for both samples, the twin-peak at 65° disappears when compared to NCA<sub>HSoC</sub> and NCA<sub>LSoC</sub> in Figure 7-1. Moreover, the lattice parameter c of R-NCA<sub>HSoC</sub> and R-NCA<sub>LSoC</sub> after the 1<sup>st</sup> sinter process is very close to NCA<sub>p</sub> (Table 7-2). Since for NCA with layer structure, the lattice parameter c is a good indication for the level of Lithium content in the structure at the low SoC range<sup>87</sup>, the result suggests that both R-NCA<sub>HSoC</sub> and R-NCA<sub>LSoC</sub> are fully relithiated after the 1<sup>st</sup> sinter treatment.

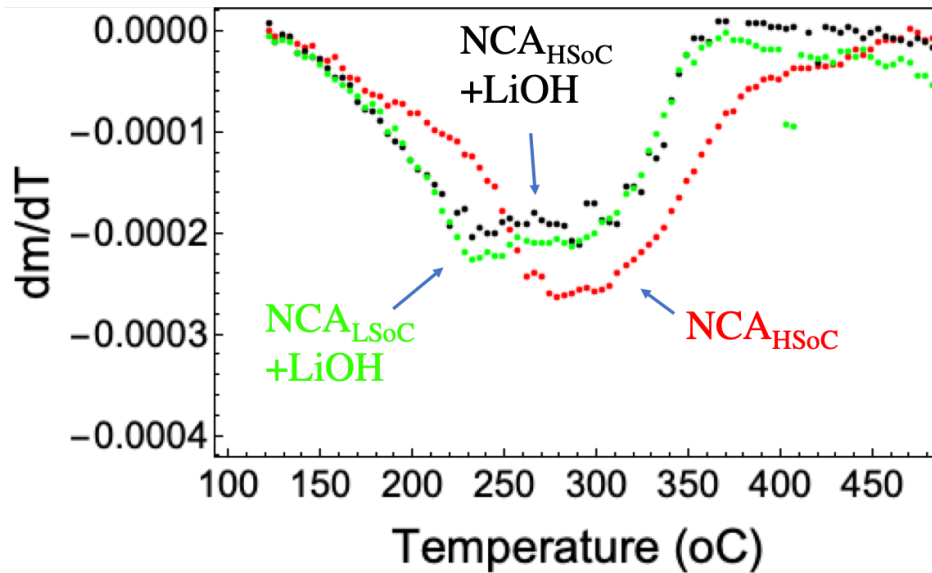


**Figure 7-4.** Mass differential curve with respect to temperature for samples ( $\text{NCA}_{\text{HSoC}}$ ,  $\text{NCA}_{\text{LSoC}}$  and  $\text{NCA}_{\text{HSoC}}$  with  $\text{LiOH} \cdot \text{H}_2\text{O}$  with 1 to 1 molar ratio) from 120 °C to 500 °C. The heating rate is 5 °C/min.

To further understand the relithiation reaction during the 1<sup>st</sup> sinter treatment, TGA assessments of  $\text{NCA}_{\text{HSoC}}$ ,  $\text{NCA}_{\text{LSoC}}$ , and  $\text{NCA}_p$  with  $\text{LiOH}$  samples are done and the data is shown in Figure 7-3. In general, there are three stages:

- 1) For 1<sup>st</sup> stage, the sample,  $\text{NCA}_p + \text{LiOH}$ , barely lost mass while for the other two samples,  $\text{NCA}_{\text{HSoC}} + \text{LiOH}$  and  $\text{NCA}_{\text{LSoC}} + \text{LiOH}$ , there are 1.8% and 4.1% mass loss respectively. There are two sources for the mass loss. The 1<sup>st</sup> source is the oxygen evolution and phase transformation of the charge (Lithium poor) NCA ( $\text{NCA}_{\text{HSoC}}$ ,  $\text{NCA}_{\text{HSoC}}$ ) due to instability of layer phase in the charged NCA. The less Li in the structure (the higher SoC), the greater its instability<sup>86</sup>. The rate of oxygen evolution reaction is maximized at 250 °C for  $\text{NCA}_{\text{HSoC}}$  (Figure 7-4). The 2<sup>nd</sup> source the reaction between  $\text{LiOH}$  and the charged NCA. When  $\text{LiOH}$  is presenting with the charged NCA,  $\text{LiOH}$  reacts with charged NCA before the oxygen evolution reaction of charged NCA during heating. This can be supported by the  $\text{dm}/\text{dT}$  curve in Figure 7-

- 4). The temperature at which the maximum mass loss rate is reached is lower (225°C) for the charged NCA in the presence of LiOH than the charged NCA without LiOH (250°C).
- 2) For the 2<sup>nd</sup> stage, the mass of all the samples (NCA<sub>P</sub>+LiOH, samples, NCA<sub>HSoC</sub>+LiOH and NCA<sub>LSoC</sub> + LiOH) remains stable. For NCA<sub>HSoC</sub> +LiOH and NCA<sub>LSoC</sub> + LiOH, no obvious mass loss suggests that the reaction between LiOH and the charge NCA (NCA<sub>HSoC</sub> , NCA<sub>LSoC</sub>) is done before the 2<sup>nd</sup> stage.
- 3) For the 3<sup>rd</sup> stage, all the three samples, NCA<sub>P</sub>+LiOH, samples, NCA<sub>LSoC</sub> + LiOH, NCA<sub>HSoC</sub> +LiOH and, show mass loss of 6.5%, 4.8% and 3.5% respectively. The source of mass loss is the decomposition of LiOH. When the charged NCA is not present, LiOH does not decompose until the temperature reaches 3<sup>rd</sup> stage. In contrast, when the charged NCA is present, some of the LiOH reacts with the charged NCA during the 1<sup>st</sup> stage and the remaining LiOH does not decompose until the temperature reaches the 3<sup>rd</sup> stage. Therefore, the mass loss is larger for NCA<sub>P</sub>+LiOH (6.5%) than NCA<sub>LSoC</sub>+LiOH (4.8%) and NCA<sub>HSoC</sub> + LiOH (3.5%).

Another thing to notice for the 1<sup>st</sup> stage is that the actual reaction rate for the oxygen evolution reaction of the charged NCA with the presence of LiOH and the reaction between LiOH and the charged NCA cannot be calculated with TGA. In-situ XRD analysis could be helpful in the future to tackle this puzzle. But this is beyond the scope of this chapter.

In general, when the charged NCA and LiOH are present during heat-treatment, LiOH starts to react with the charged NCA during 1<sup>st</sup> stage (120°C--360 °C). Therefore, the relithiation reaction

is complete (meaning charged NCA is fully relithiated) during the 1<sup>st</sup> sinter process (480°C for 3h), regardless of the SoC of the charged NCA as long as there is sufficient LiOH (in this case 1:1 molar ratio of reactant makes it sure).

#### Effect of difference in SoC

For a specific SoC value of the charged NCA, corresponding optimal amount/ratio of LiOH is needed. For example, some researchers firstly used inductively coupled plasma (ICP) to analyze the composition of to-be-recycled cathode materials.<sup>10,88</sup> Then they calculated the appropriate amount of Lithium source needed. However, as mentioned in the introduction, it is not practical to implement this method since the SoC and therefore the degree of lithiation of aged cathode materials from different collected aged Li-ion batteries will vary significantly. To overcome this problem, we proposed that there are two key factors in the process: utilization of an excess of LiOH and implementing a washing step after 2<sup>nd</sup> sinter step.

Our previous result in chapter 6 suggests that when less-than-stoichiometric LiOH was brought into contact with charged NCA, the final recycled product shows the transformation of layer phase to spinel/rocksalt phase due to insufficient Li in structure to stabilize the layered structure during the high temperature process<sup>85</sup>, which then results in poor electrochemical performance and/or low specific capacity material. Based on the result and the understanding of the relithiation steps discussed above, we submit that it is critical to have a significant excess of LiOH (more than stoichiometry) when compared to the charged NCA. In this paper, we used 1:1 molar ratio to make sure that the charged NCA with different SoC can be fully relithiated regardless of their SoC. This is supported by the XRD result in Figure 7-2 and Table 7-2, where

both  $\text{R-NCA}_{\text{HSoC}}$  and  $\text{R-NCA}_{\text{LSoC}}$  shows a layer structure and full relithiation based on lattice parameter  $c$ .

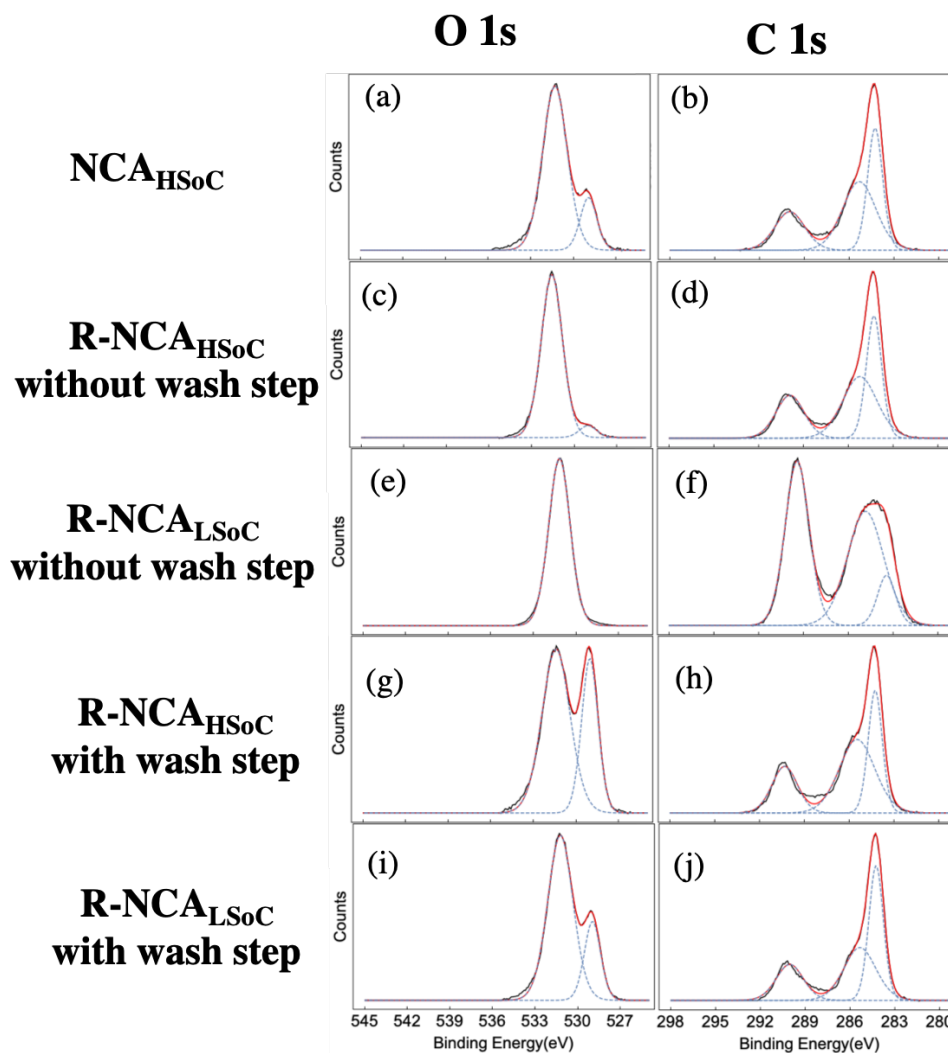


**Figure 7-5.** XPS O1s and C1s spectrums of samples, (a-b)  $\text{NCA}_{\text{HSoC}}$ , (c-d,g-h)  $\text{R-NCA}_{\text{HSoC}}$ , with/without wash step after 2<sup>nd</sup> sinter process and (e-f, i-j)  $\text{R-NCA}_{\text{LSoC}}$  with/without wash step after 2<sup>nd</sup> sinter process. The black line is recorded data. The blue dashed lines are peaks deconvolution. The red line is for simulated peaks based on deconvoluted peaks.

The problem with using an excess of LiOH is the residual surface layer materials.  $\text{R-NCA}_{\text{HSoC}}$  and  $\text{R-NCA}_{\text{LSoC}}$  without wash step after 2<sup>nd</sup> sinter step were characterized by XPS (Figure 7-5). In O 1s spectrum, the peak around 528.31 eV is from the metal-O bond. Both  $\text{R-NCA}_{\text{HSoC}}$  and  $\text{R-NCA}_{\text{LSoC}}$

NCA<sub>LSoC</sub> without the wash step present much lower intensity or no intensity of metal-O bond at all when compared to NCA<sub>HSoC</sub> and NCA<sub>LSoC</sub>. This is due to the fact that a layer of materials with a certain thickness covers the NCA particle surface so that the XPS signal of metal-O bond from NCA is shielded by this layer of materials.<sup>66</sup> At the same time, we also notice the strong XPS peak signal at 531.50 eV, indicated by red dashed line, is from C-O in CO<sub>3</sub><sup>2-</sup>.<sup>66, 80</sup> This suggests that the layer of materials that covers the NCA particle surface is from Li<sub>2</sub>CO<sub>3</sub> which is likely to be the product of air and residual LiOH/Li<sub>2</sub>O after the 2<sup>nd</sup> sinter process. To further confirm this finding, TEM imaging of the R-NCA<sub>LSoC</sub> without the wash step was collected (Figure 7-6). The effect of this layer of Li<sub>2</sub>CO<sub>3</sub> on the recycled product is obvious. The electrochemical test in Figure 7-7 shows that both R-NCA<sub>HSoC</sub> and R-NCA<sub>LSoC</sub> without the wash step show large polarization even at 0.1C rate and barely any usable capacity, mainly due to resistance of surface Li<sub>2</sub>CO<sub>3</sub>.

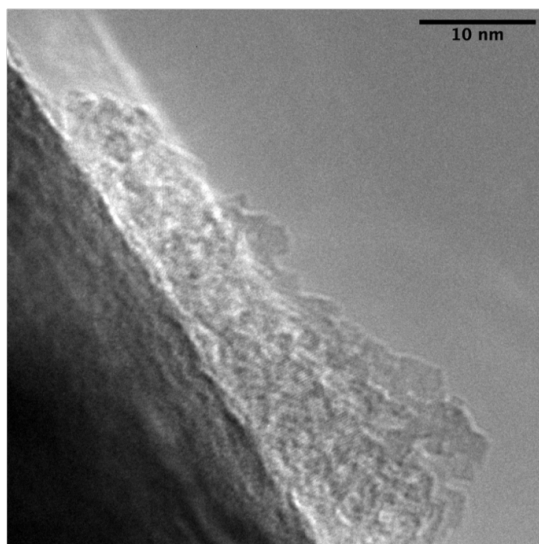


**Figure 7-6.** TEM image of R-NCA<sub>LSoC</sub> without(b) wash step after 2<sup>nd</sup> sinter process.

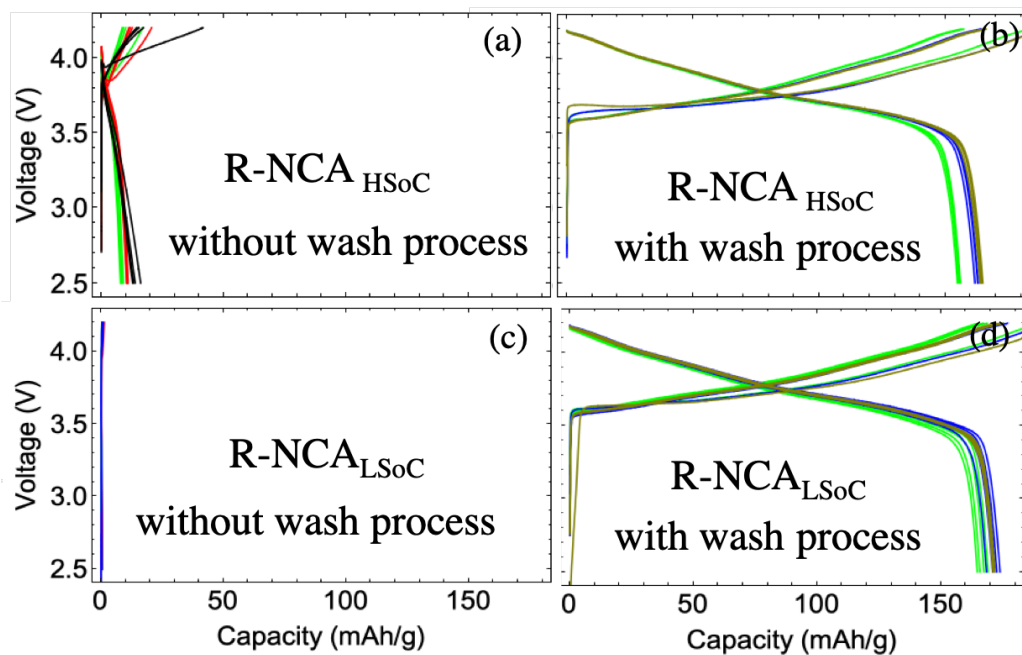


**Figure 7-7.** Electrochemical test of 4 samples in coin cells, R-NCA<sub>HSO<sub>c</sub></sub> with/without wash step after 2<sup>nd</sup> sinter process and R-NCA<sub>LSoC</sub> with/without wash step after 2<sup>nd</sup> sinter process. For each sample, three coin cells were tested, indicated by three colors. For each coin cell, it was cycled in between 2.5V and 4.2V with a 0.2c rate for 4 cycles.

In order to resolve this problem, we added a wash step by washing recycled products with DI-water and then dried it. For R-NCA<sub>HSO<sub>c</sub></sub> and R-NCA<sub>LSoC</sub> with the wash step, the peak at 528.31 eV appears again and the relative intensity of peak at 531.50 eV decreases, indicating that the thickness of the Li<sub>2</sub>CO<sub>3</sub> surface layer is reduced. As for the electrochemical performance, R-NCA<sub>HSO<sub>c</sub></sub> and R-NCA<sub>LSoC</sub> with the wash step show consistent and as good discharge capacity as NCA<sub>p</sub>, which is around 175 mAh/g. By comparing the samples with/without the wash step, we can see the wash step can wash away some Li<sub>2</sub>CO<sub>3</sub> on the surface due to the excess of LiOH, reduce the resistance, and help improve the recycled product electrochemical performance.

No Li-rich cathode phase is formed in R-NCA<sub>LSoC</sub> and R-NCA<sub>HSO<sub>c</sub></sub> even when excess of LiOH is used. This was supported by the coin cell test where no plateau was present at high voltage<sup>89</sup> (up



to 4.8V) and XRD pattern where no corresponding peak for Li-rich phase<sup>90</sup>. The potential reason is that the Li-rich phase ( $x\text{Li}_2\text{MnO}_3 \cdot (1-x)\text{LiMO}_2$ ) is Mn-based. For NCA materials, there is no Mn so that Li-rich phase thermodynamically not stable.

In general, we used the excess Li strategy to deal with variation in SoC of different NCA and to make sure they can all be fully relithiated. Then, we use a water wash step to remove excess/residual  $\text{Li}_2\text{CO}_3$ . With these two strategies, the effect of different SoC of aged NCA materials on the recycled NCA can be resolved.

### 7.3.3 Effect of surface reconstruction layer

As mentioned in the introduction part, NCA is likely to have surface reconstruction when cycled under high temperature or high voltage, where the layer phase transforms into spinel/rocksalt phases. To investigate the effect of the surface reconstruction layer, we firstly create NCA materials with different levels of the spinel/rocksalt phases by treating  $\text{NCA}_{\text{HSoC}}$  at two different temperatures, 350°C and 650°C.<sup>86</sup> For  $\text{NCA}_{\text{HSoC}_350\text{C}}$  (Figure 7-8 (a)), the peak ratio of (003)/(104) decreases and the twin-peak at 65° merged into one peak. All these suggest transformation from the layered phase to the spinel/rocksalt phases.<sup>85-86</sup> For  $\text{NCA}_{\text{HSoC}_650\text{C}}$ , the peak ratio of (003)/(104) is even lower, which qualitatively suggest a higher level of spinel/rocksalt phases for  $\text{NCA}_{\text{HSoC}_650\text{C}}$  when compared with  $\text{NCA}_{\text{HSoC}_350\text{C}}$ . Here, the general trend was clear but the quantitative calculation of the percentage of layer, spinel, and rocksalt phases was not done due to overlap of peaks for three phases in XRD pattern and resolution of XRD facility we have.<sup>91</sup> For the future, XRD with in-situ mass spectra of  $\text{O}_2$  can be used for quantitative analysis<sup>87</sup>. Electrochemical test results in Figure 7-9 (a,d) match with the XRD result as  $\text{NCA}_{\text{HSoC}_350\text{C}}$

shows lower impedance and higher discharge capacity than  $\text{NCA}_{\text{HSoC}_{650\text{oC}}}$  due to less content of spinel/rocksalt phases.

After the recycling process with a 12h 2<sup>nd</sup> sinter step, both of the recycled products show XRD peaks similar to that of the layered structure (Figure 7-8). However, the peak ratio of (003)/(104) for  $\text{R-NCA}_{\text{HSoC}_{350\text{oC}}}$  is 0.92, which is slightly higher than that of  $\text{R-NCA}_{\text{HSoC}_{650\text{oC}}}$  (0.86). As for electrochemical performance, Figure 7-9(b,e) show that  $\text{R-NCA}_{\text{HSoC}_{350\text{oC}}}$  shows slightly lower discharge capacity than  $\text{NCA}_{\text{P}}$  while  $\text{R-NCA}_{\text{HSoC}_{650\text{oC}}}$  shows lower capacity and less stability. There are two possible reasons behind the difference. First, it is known that the spinel/rocksalt phase is a thermodynamically more stable phase than the layer phase<sup>92</sup> and they cause large resistance due to the lower Li diffusion rate. While  $\text{NCA}_{\text{HSoC}_{350\text{oC}}}$  and  $\text{NCA}_{\text{HSoC}_{650\text{oC}}}$  went through the same recycling process,  $\text{NCA}_{\text{HSoC}_{650\text{oC}}}$  needs more kinetic driving force<sup>93-94</sup> (longer time, higher temperature or more Li source) to transform the spinel/rocksalt phase back to the layer phase as  $\text{NCA}_{\text{HSoC}_{650\text{oC}}}$  contains more spinel/rocksalt phases than  $\text{NCA}_{\text{HSoC}_{350\text{oC}}}$ . Second, the recycled products contain the layered phase. However, there is Li/Ni disordering that happened in the bulk of recycled products.<sup>77</sup> As both reasons could lead to a lower ratio of (003)/(104) in XRD pattern and lower electrochemical performance<sup>77</sup>, it is hard to differentiate which is the major cause. High-resolution XRD would help to the differentiation in the future. But this is not within the scope of this paper. Based on these two potential causes, we did experiments where we extended the 2<sup>nd</sup> sinter time to 24h while keeping the rest of the process parameters the same. In Figure 7-8 (a,b), for samples with 2<sup>nd</sup> sinter time of 24h, ratios of (003)/(104) for  $\text{R-NCA}_{\text{HSoC}_{350\text{oC}}}$  and  $\text{R-NCA}_{\text{HSoC}_{650\text{oC}}}$  further increased to 1.11 and 0.98 from 0.91 and 0.86,

respectively. The electrochemical performance (Figure 7-9 (c.f)) of both samples shows similar discharge capacity and stability as  $\text{NCA}_P$ .

In general, the result in this part suggests that with the presence of a Lithium source, a appropriate temperature, we can transform the spinel/rocksalt phases of NCA back to layered phase in order to regain electrochemical capacity. The longer 2<sup>nd</sup> sinter time may be needed to re-construct/ re-order NCA with a different level of spinel/rocksalt phases. One thing to mention is that other factors could affect the recycled NCA when the longer sinter time is used, for example, evaporation of the Lithium source. Here, since we used a 1:1 molar ratio for reactants, we make sure there was enough Lithium source to compensate for evaporation even if the 2<sup>nd</sup> sinter time is 24h. Although increasing the temperature is another way to offer more kinetical driving force, higher temperature ( $>730^\circ\text{C}$ ) could result in more problems, such as more evaporation of Li and decomposition of NCA.<sup>95</sup>

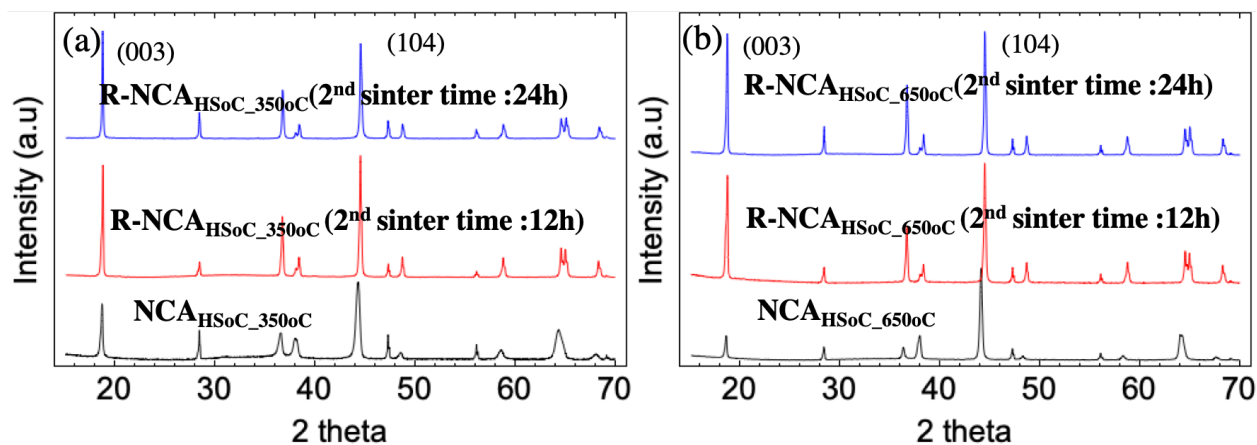


**Figure 7-8.** XRD of samples (a)  $\text{NCA}_{\text{HSoC}_350^\circ\text{C}}$ ,  $\text{R-NCA}_{\text{HSoC}_350^\circ\text{C}}$  with different 2<sup>nd</sup> sinter time (12h and 24h) and (b)  $\text{NCA}_{\text{HSoC}_650^\circ\text{C}}$ ,  $\text{R-NCA}_{\text{HSoC}_650^\circ\text{C}}$  with different 2<sup>nd</sup> sinter time (12h and 24h)

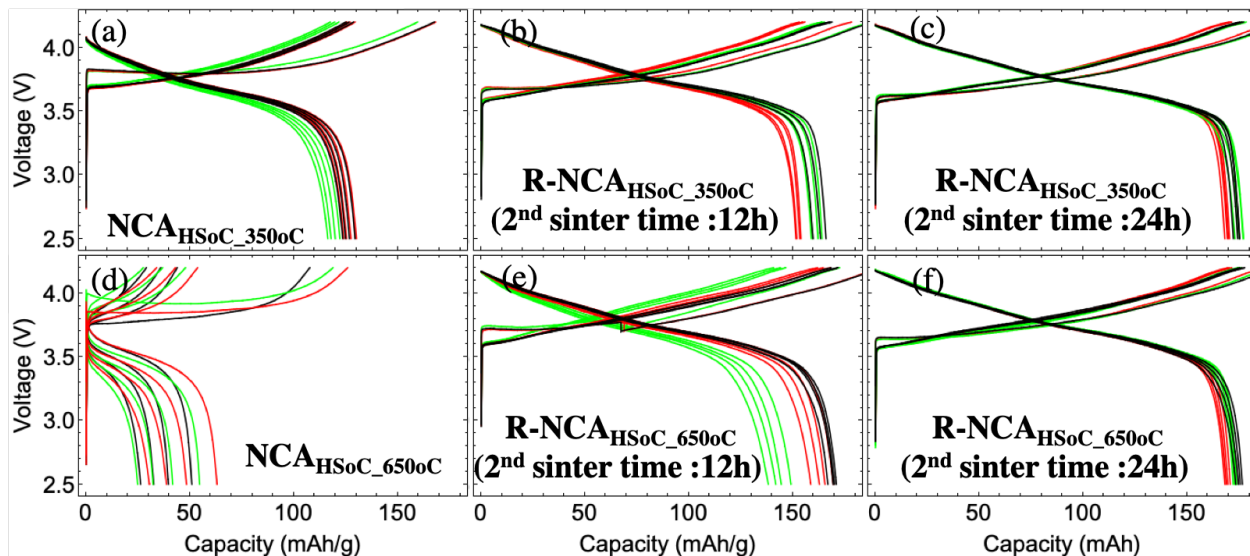


**Figure 7-9.** Electrochemical test of 6 samples in coin cells,  $\text{NCA}_{\text{HSO}_c_{350^\circ\text{C}}}$ ,  $\text{R-NCA}_{\text{HSO}_c_{350^\circ\text{C}}}$  with different 2<sup>nd</sup> sinter time (12h and 24h) and (b)  $\text{NCA}_{\text{HSO}_c_{650^\circ\text{C}}}$ ,  $\text{R-NCA}_{\text{HSO}_c_{650^\circ\text{C}}}$  with different 2<sup>nd</sup> sinter time (12h and 24h). For each sample, three coin cells were tested, indicated by three colors. For each coin cell, it was cycled in between 2.5V and 4.2V with a 0.2c rate for 4 cycles.

Note that we are describing the bulk NCA (particle size > 500 nm) change in between layered phases and spinel/rocksalt phases. For typical aged NCA materials, the layer of surface reconstruction (spinel/rocksalt phases) normally has a thickness less than 20nm.<sup>92, 96</sup> The percentage of spinel/rocksalt phases in total phases is very small so that less thermal driving force (sinter time) is needed. Therefore, the 2<sup>nd</sup> sinter time used here may be too long to reconstruct/ re-order surface reconstruction layer of aged NCA materials.

#### 7.3.4 Effect of SEI

As mentioned in the introduction part, NCA will form SEI during cycling, which has been found to be a combination of organic and inorganic compounds. To investigate the effect of the SEI on the recycled NCA, we firstly create NCA with thick SEI on the particle surface by immersing  $\text{NCA}_{\text{HSO}_c}$  in the electrolyte (DEC:EC=1:1, 1M  $\text{LiPF}_6$ ) for 14 days. As

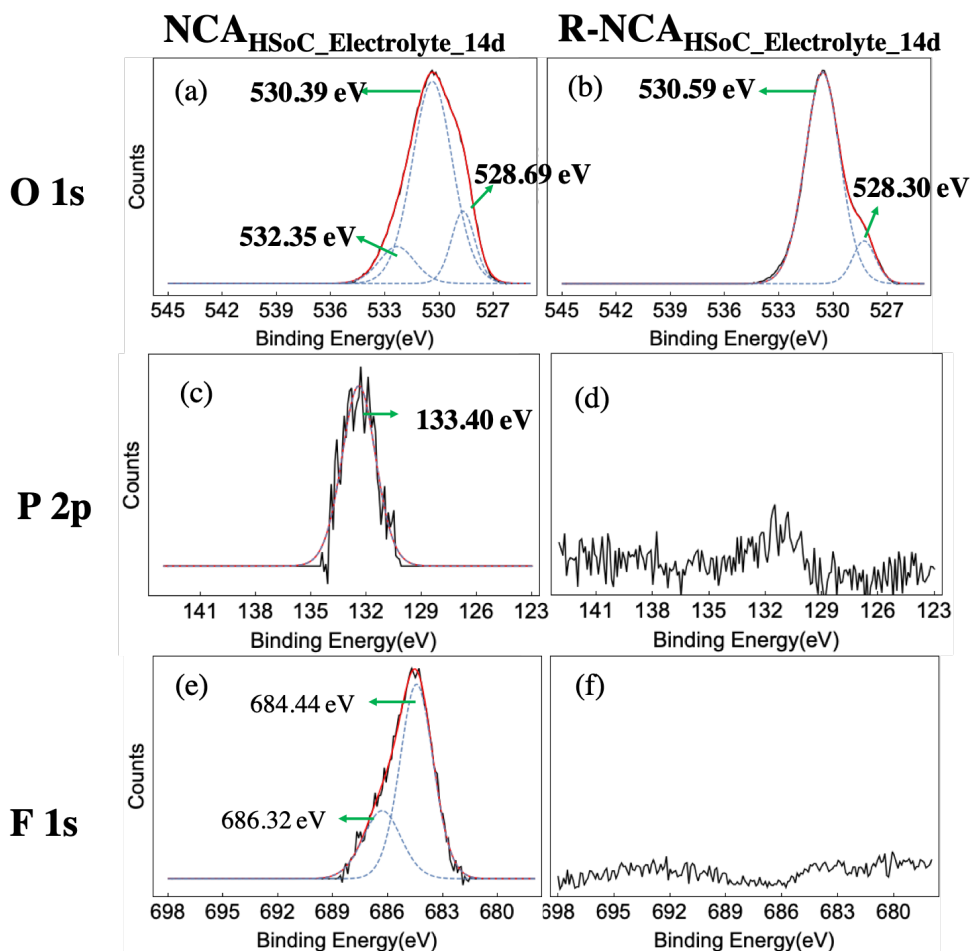


**Figure 7-10.** XPS O1s, P2p and F1s spectrums of  $\text{NCA}_{\text{HSoC\_electrolyte\_14d}}$  (a, c, e) and  $\text{R-NCA}_{\text{HSoC\_electrolyte\_14d}}$  (b, d, f).

The black line is recorded data. The blue dashed lines are peaks deconvolution. The red line is for simulated peaks based on deconvoluted peaks.

shown by XPS result in Figure 7-10 (a,c,e),  $\text{NCA}_{\text{HSoC\_electrolyte\_14d}}$  shows a change of surface chemistry, suggesting formation of SEI on  $\text{NCA}_{\text{HSoC}}$  surface. In O 1s spectrum (Figure 7-10 (a)), the deconvolution of the O1s by 3 peaks is used. The peak at 528.69 eV corresponds to the metal-oxygen bond in NCA. The peak at 530.39 eV corresponds to  $\text{Li}_2\text{CO}_3$ . The peak at 532.35 eV corresponds to C=O bond, which is likely to be lithium alkyl carbonate species.<sup>80</sup> The peak at 133.4 eV in P 2p (Figure 7-10 (c)) is likely to be  $\text{Li}_x\text{PF}_y\text{O}_z$ .<sup>66</sup> In the F 1s spectrum (Figure 7-10

(e)), the peak at 684.44 eV corresponds to LiF and the peak at 686.32 eV corresponds to  $\text{Li}_x\text{PF}_y\text{O}_z$ .<sup>66</sup>

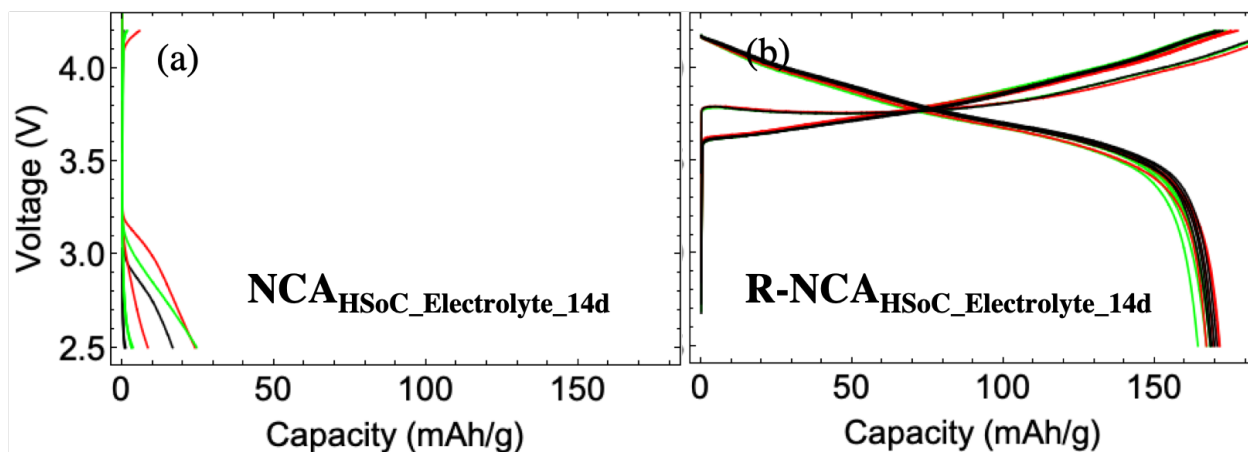


**Figure 7-11.** Electrochemical test of 2 samples in coin cells,  $\text{NCA}_{\text{HSoC\_electrolyte\_14d}}$  (a) and  $\text{R-NCA}_{\text{HSoC\_electrolyte\_14d}}$  (b).

For each sample, three coin cells were tested, indicated by three colors. For each coin cell, it was cycled in between 2.5V and 4.2V with 0.2c rate for 4 cycles.

As for the electrochemical performance,  $\text{NCA}_{\text{HSoC\_electrolyte\_14d}}$  shows large polarization and low capacity, which is likely due to the thick SEI formed on the NCA particle surface. After the recycling process, the surface chemistry of  $\text{R-NCA}_{\text{HSoC\_electrolyte\_14d}}$  is very different from  $\text{NCA}_{\text{HSoC\_electrolyte\_14d}}$ . No peak is observed in P 2p and F 1s spectrums, suggesting P and F containing compounds in the SEI, such as  $\text{Li}_x\text{PF}_y\text{O}_z$  and LiF, reacted with LiOH and were eliminated during the recycling process. As for the electrochemical performance,  $\text{R-NCA}_{\text{HSoC\_electrolyte\_14d}}$  (Figure 7-11) shows similar performance as  $\text{NCA}_p$ .

In general, SEI on the NCA surface will not have an obvious effect on the recycled product as long as LiOH is present during the high temperature(730°C) sintering step since the SEI reacts with LiOH during the sintering step.

## 7.4 Conclusion

In this chapter, we investigated process factors that affect the evolution of three properties of aged  $\text{LiNi}_{8.15}\text{Co}_{1.5}\text{Al}_{0.35}\text{O}_2$  (NCA). We did this separately on the recycled products, and we examined the influence of state-of-charge (SoC), surface reconstruction layer, and SEI formation. To address the difference in SoC of aged NCA, an excess of LiOH and a wash step after 2<sup>nd</sup> sinter process were found to be critical. For the surface reconstruction layer, a longer 2<sup>nd</sup> sinter time was necessary to provide enough thermal driving force, provided that enough LiOH is present. As for the SEI, we found that LiOH reacts with the SEI and decomposes it during the sintering process. As such, no additional steps were needed. Therefore, it is practical to use direct recycling to deal aged NCA with the difference in these three properties and get homogeneous recycled NCA. In the future, other properties of aged NCA materials, including cracking and metal dissolution, should be investigated further to find out the corresponding key process step/factor to address the difference in each property.

# Chapter 8. Direct Recycling of Aged $\text{LiMn}_2\text{O}_4$

## Cathode Materials used in Aqueous Lithium-ion Batteries: Processes and Sensitivities

### 8.1 Overview

Chapter 6 and 7 is focused on NCA materials from the organic-electrolyte Li-ion battery system. In this chapter, we used aged LMO cathode material from a large-format aqueous lithium-ion battery. We applied two direct recycling methods with different process parameters: solid-state method and hydrothermal method and compare the sensitivity of two processes to starting materials. The recycled products of the two methods are compared in terms of phase purity and electrochemical energy storage capacity. Moreover, we created aged LMO with different state of charge (SoC), applied the same direct recycling method to them and compared the results.

Hypotheses:

- Lost electrochemical capacity of aged  $\text{LiMn}_2\text{O}_4$  can be recovered by either one of these methods: solid-state reaction method and hydrothermal reaction method. After cycling,  $\text{LiMn}_2\text{O}_4$  cathode materials lost electrochemical capacity compared with fresh  $\text{LiMn}_2\text{O}_4$ . Exposing the aged and low-capacity  $\text{LiMn}_2\text{O}_4$  to LiOH solid by two-step heat treatment (solid state method) or to LiOH solution by hydrothermal reaction (hydrothermal method) can recover lost electrochemical capacity of the aged  $\text{LiMn}_2\text{O}_4$ .



- The lithium content in aged  $\text{LiMn}_2\text{O}_4$  influences the recycled product regarding phase purity and electrochemical capacity. Aged  $\text{LiMn}_2\text{O}_4$  with less lithium content shows lower thermal stability. Under the same regeneration process, aged  $\text{LiMn}_2\text{O}_4$  with lower thermal stability is more likely to decompose or transform into another phase, resulting in more impure phase and lower electrochemical capacity for recycling product.

## 8.2 Experimental

This section will describe the collection of both aged and fresh LMO and creation of the aged LMO with different SoC using electrochemical titration. Two different recycling methods were applied to the aged cathode. Different properties and electrochemical characterization of recycled products are described. The naming of different samples used in the paper is introduced in Table 8-1.

<b>Table 8-1. Outline for Sample Name</b>	
<b>Description</b>	<b>Name</b>
Collected LMO without being cycled in battery	Fresh LMO
Collected LMO cycled in battery for over hundreds of cycles	Aged LMO
Recycled product of aged LMO through solid-state reaction	LMO-SS
Recycled product of aged LMO through hydrothermal reaction	LMO-HT (molar ratio of reactants LMO:LiOH, reaction temperature, reaction time)

### 8.2.1 Collecting of aged LMO and fresh LMO

Details of synthesis of LMO, LMO electrode making procedure and cycling of  $\text{LiMn}_2\text{O}_4$  were described previously.<sup>97</sup> Briefly,  $\text{LiMn}_2\text{O}_4$  was synthesized through the solid-state reaction between electrolytic manganese dioxide and lithium carbonate.  $\text{Li}_2\text{CO}_3$  was ball milled with electrolytic manganese dioxide (EMD, Tronox) (Spex 8000, silicon nitride crucible) or attritor

milled (Union Process, 2 mm diameter media) in the proper molar ratio for 60–120 min. This precursor mix, held in alumina crucible, was fired at 750–800 °C in ambient air for 8–12 h with heating and cooling ramp rates of 5 °C min<sup>-1</sup>. The composite cathode electrode pellet consisted of LiMn<sub>2</sub>O<sub>4</sub>, carbon black, natural graphite and binder in 80:2:10:8 mass ratio. The cathode was cycled in full aqueous battery stack over hundreds of cycles and the cycling data is shown in SI. The aged LMO was collected by taking out cathode electrode pellet after cycling, cleaning cathode electrode materials with DI water for three times and drying at 80°C overnight. The fresh LMO was collected by taking out the cathode electrode pellet that sat in the aqueous battery for the same period but without cycling, cleaning with DI water for three times and drying at 80°C overnight.

### 8.2.2 Creating aged LMO with different SoC

The aged LMO with different SoC was created by electrochemical titration. A three-electrode cell was used that was comprised of Teflon Swagelok with the aged LMO as a working electrode (around 100mg), activated carbon as a counter electrode and Hg/Hg<sub>2</sub>SO<sub>4</sub> (MSE) as a reference electrode. The mass load of the counter electrode was four times that of the working electrode to ensure that the working electrode reached voltage limit first. The full cell was exposed to galvanostatic cycling with potential limitation at a low rate (less than 0.05C) to get the full capacity of the working electrode. Then the aged LMO with different SoC was created by charging the working electrode for different times in the second cycle based on the slow-rate cycling capacity data in the first cycle.

### 8.2.3 Recycling of aged LMO through solid-state reaction method

The final product of this method will be referred as LMO-SS, as shown in Table 1. In short, aged  $\text{LiMn}_2\text{O}_4$  and  $\text{LiOH}$  were mixed in 1:1 molar ratio and were ball-milled (Spex 8000 Mixer Mill) for 30 minutes. Then the mixture was heated to  $350^\circ\text{C}$  at the rate of  $5^\circ\text{Cmin}^{-1}$ , hold at  $350^\circ\text{C}$  for 2 hours and cooled down in the air. The intermediate product was collected by washing the mixture after the first heat-treatment with DI water three times and dried overnight at  $80^\circ\text{C}$ . Then the intermediate product was fired at  $750^\circ\text{C}$  for 6 hours with heating and cooling rate of  $5^\circ\text{Cmin}^{-1}$  in the air. The final product was washed with DI water three times and dried at  $80^\circ\text{C}$  overnight. For comparison, one sample was recycled through the two steps of heat-treatments without washing in between them. As shown in a previous paper,<sup>98</sup> the source of lithium (ie what type of salt), did not have an obvious effect on the structure or performance of  $\text{LiMn}_2\text{O}_4$ .

#### 8.2.4 Recycling of aged LMO through hydrothermal reaction method

The final product of this method will be referred as LMO-HT, as shown in Table1. In short, the aged LMO and  $\text{LiOH}$  molar ratio (1:10,1:1,10:1) were added into 50 mL DI water and were stirred for 1 hour. The solution was then transferred into a Teflon-lined stainless steel autoclave. The autoclave was sealed and heated at the chosen temperature ( $145^\circ\text{C}$ ,  $165^\circ\text{C}$ ,  $185^\circ\text{C}$ ) for the different time (12h, 24h,48h). The product was washed with DI water for 3 times and dried at  $80^\circ\text{C}$  overnight.

#### 8.2.5 Materials property characterization

XRD, SEM, and TGA were conducted based on the description in Chapter 3.

#### 8.2.6 Electrochemical characterization

Both cyclic voltammetry (CV) and galvanostatic cycling with potential limitation (GCPL) were conducted by Bio Logic VMP3 Multi-Channel Potential/Electrochemical Impedance Spectrometer. For the electrochemical test of the fresh and aged LMO electrode materials, the collected electrode materials were used without adding more binder and carbon black. LMO-SS, and LMO-HT electrode materials were prepared by mixing 80 wt% of recycled LMO materials (LMO-HT samples had a certain amount of graphite that came from aged LMO sample and did not react during the hydrothermal recycling process), 10 wt% carbon black and 10 wt% Polyvinylidene fluoride (PVDF) with N-methylpyrrolidone (NMP) and dried at 80°C overnight. For CV test, LMO electrode materials (around 5 mg) were pressed onto stainless steel mesh with an area of around 0.3 cm<sup>2</sup>. Samples were scanned between 0 V and +0.7 V vs Hg/Hg<sub>2</sub>SO<sub>4</sub> (MSE) with scan rate 0.25 mVs<sup>-1</sup> (all voltage values used in CV were versus MSE otherwise mentioned). The electrodes were tested in three-electrode cells containing 1M Li<sub>2</sub>SO<sub>4</sub> aqueous electrolyte with a platinum wire as the counter electrode and MSE as the reference electrode. The current density normalized by mass percentage of LMO active materials. For GCPL test, three-electrode Teflon Swagelok cells with stainless steel rods as current collectors and 1M Li<sub>2</sub>SO<sub>4</sub> aqueous electrolyte were used. The cathode was prepared by pressing 50 mg LMO electrode materials in a 10 mm die set. The anode was made by pressing the 500 mg NaTi<sub>2</sub>(PO<sub>4</sub>)<sub>3</sub> electrode materials used in a previous paper<sup>97</sup> in a 10 mm die set. MSE was used as reference electrode. The mass difference between anode and cathode ensured that the cathode was voltage limiting electrode. The cell was cycled with voltage limits of the cathode in the range from +0.24 V to +0.57 V at a C/6 rate. Only cathode charge-discharge curves are shown in this work. The capacity is normalized by mass percentage of LMO active materials.

## 8.3 Result

### 8.3.1 TGA

TGA data were collected and the mass percentage of active materials LMO was determined for LMO-HTs by different hydrothermal recycling conditions, aged LMO and fresh LMO by calculating mass at the end of TGA over mass at the beginning of TGA, as shown in Table 8-2. The mass difference before and after TGA test mainly results from burning of graphite, carbon black and binder.

<b>Table 8-2. Mass Ratio of LMO Active Materials in Products</b>				
$\frac{m_{end}}{m_{initial}}$		145°C	165°C	185°C
LMO:LiOH=10:1	24hr	0.640	0.666	
LMO:LiOH=1:1	12hr		0.683	
	24hr	0.645	0.658	0.652
	48hr		0.711	
LMO:LiOH=1:10	24hr		0.693	0.683
Aged LMO		0.775		
Fresh LMO		0.792		

### 8.3.2 SEM

Figure. 8-1 (a-c) show that primary particle size and particle shape are the almost the same for the aged LMO, LMO-SS, and LMO-HT(1:1, 165°C, 24hr). LMO-SS in Figure 8-1 (b) shows larger secondary particle while LMO-HAT in Fig. 1c shows more homogeneous particle size. In Figure 8-1 (d) for LMO-HT(10:1, 165°C, 24hr), there are flake-like and stick-like shape particles shown on the surface of bulk materials.

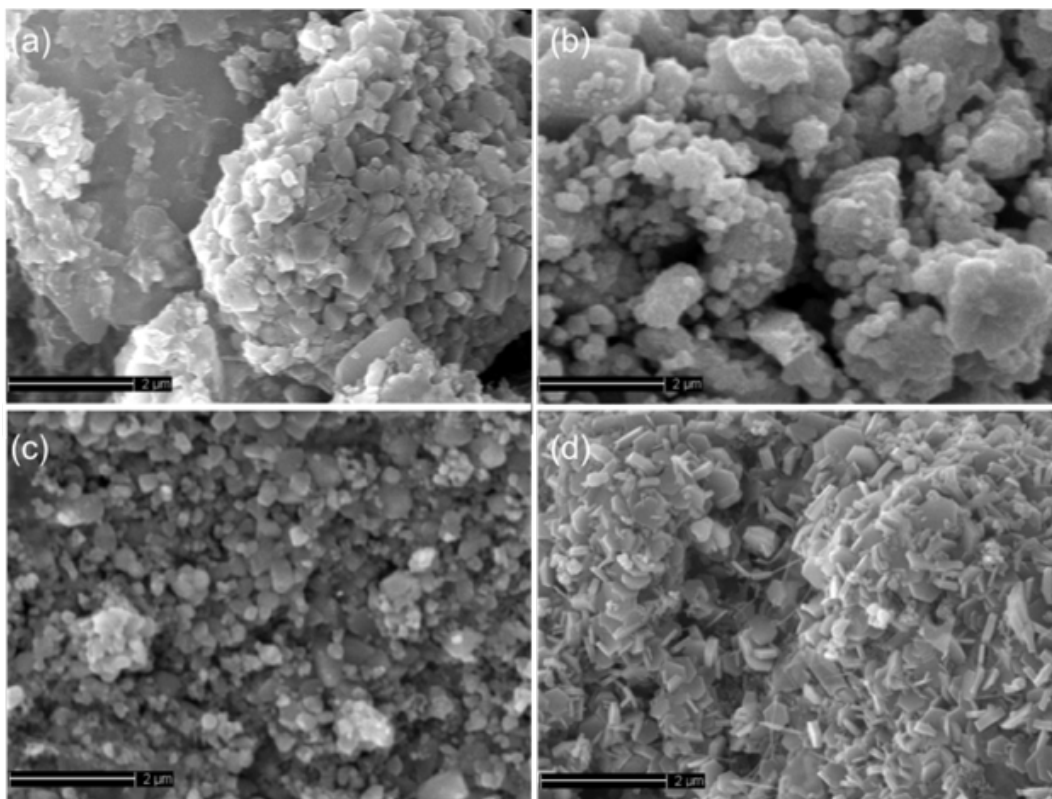
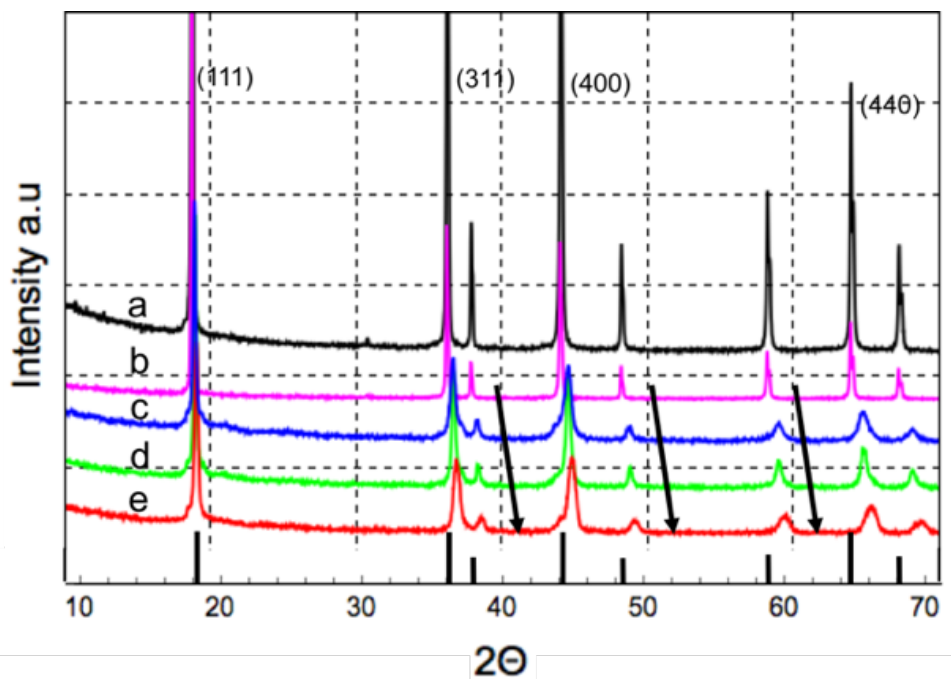


**Figure 8-1.** SEM images of a) aged LMO, b) LMO-SS recycled from aged  $\text{Li}_{0.7}\text{Mn}_2\text{O}_4$  with washing in between two-step of heat treatments, c) LMO-HT(1:1, 165°C, 24hr) recycled from aged  $\text{Li}_{0.7}\text{Mn}_2\text{O}_4$ , d) LMO-HT(10:1, 165°C, 24hr) recycled from aged  $\text{Li}_{0.7}\text{Mn}_2\text{O}_4$ .

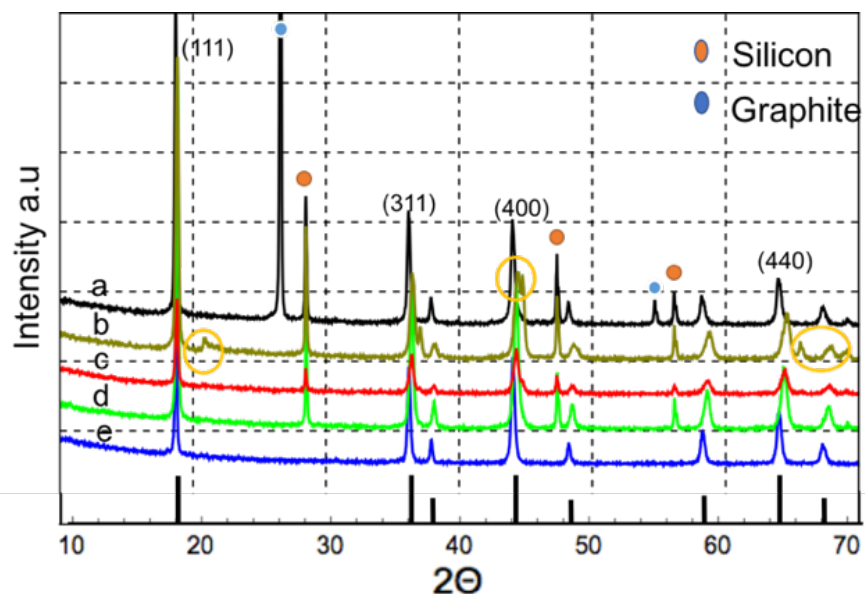
### 8.3.3 XRD

Figure 8-2 shows XRD patterns of fresh LMO and aged LMO at different SoC. The peaks shift to higher  $2\theta$  value when SoC of aged LMO increases. No peaks of impurity phases are present in the XRD patterns of any of the samples. Figure 8-3 shows XRD patterns of fresh LMO, LMO-SS recycled with/without washing in between two steps of heat-treatments and LMO-SS recycled from aged LMO at different SoC. Silicon powder was added into samples and its peaks are located at 28.5°(111), 47°(220) and 56°(311). Graphite peaks are located at 26°(002) and 55°(004). The LMO-SS from aged  $\text{Li}_{0.3}\text{Mn}_2\text{O}_4$  without washing shows peaks of impurity phases at around 21°, 45° and 67°. Other recycled products don't show any peaks of impurity phases.

Figure 8-4 shows XRD patterns of fresh LMO, LMO-HT(1:1, 165°C, 24hrs) recycled from aged LMO at different SoC. Graphite peaks are located at 26°(002), 55°(004). Both recycled products don't show any peaks of impurity phases are present.



**Figure 8-2.** X-ray diffraction patterns of a) fresh LMO, b) aged LMO, c) aged  $\text{Li}_{0.7}\text{Mn}_2\text{O}_4$ , d) aged  $\text{Li}_{0.5}\text{Mn}_2\text{O}_4$  and e) aged  $\text{Li}_{0.3}\text{Mn}_2\text{O}_4$



**Figure 8-3.** X-ray diffraction patterns of a) fresh LMO, b) LMO-SS recycled from aged  $\text{Li}_{0.3}\text{Mn}_2\text{O}_4$  without washing between two steps of heat-treatments, LMO-SS recycled with washing between two steps of heat-treatments from c) aged LMO, d) aged  $\text{Li}_{0.7}\text{Mn}_2\text{O}_4$  and e) aged  $\text{Li}_{0.3}\text{Mn}_2\text{O}_4$ .

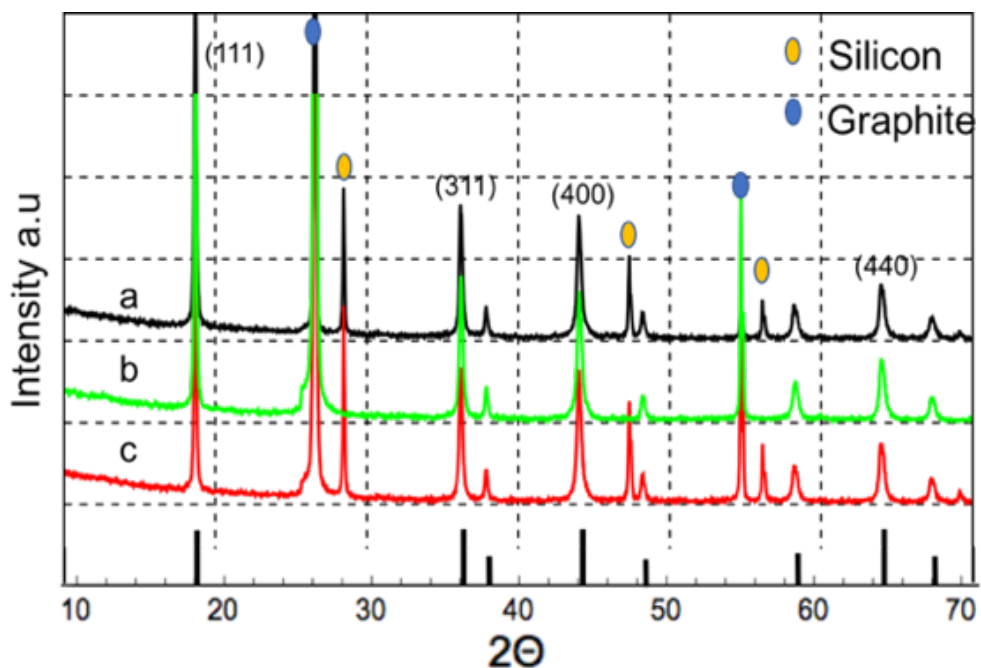


**Figure 8-4.** X-ray diffraction patterns of a) fresh LMO, b) LMO-HT(1:1, 165°C, 24hrs) recycled from aged  $\text{Li}_{0.7}\text{Mn}_2\text{O}_4$ , c) LMO-HT(1:1, 165°C, 24hrs) recycled from aged  $\text{Li}_{0.3}\text{Mn}_2\text{O}_4$



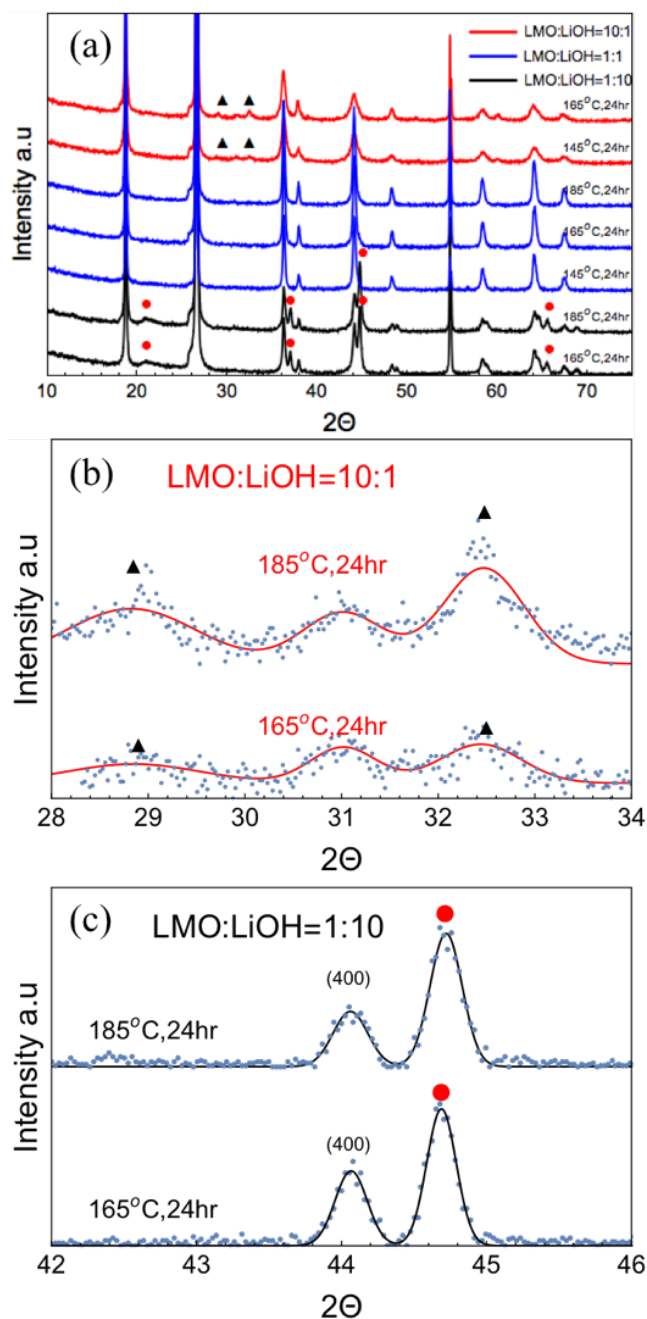
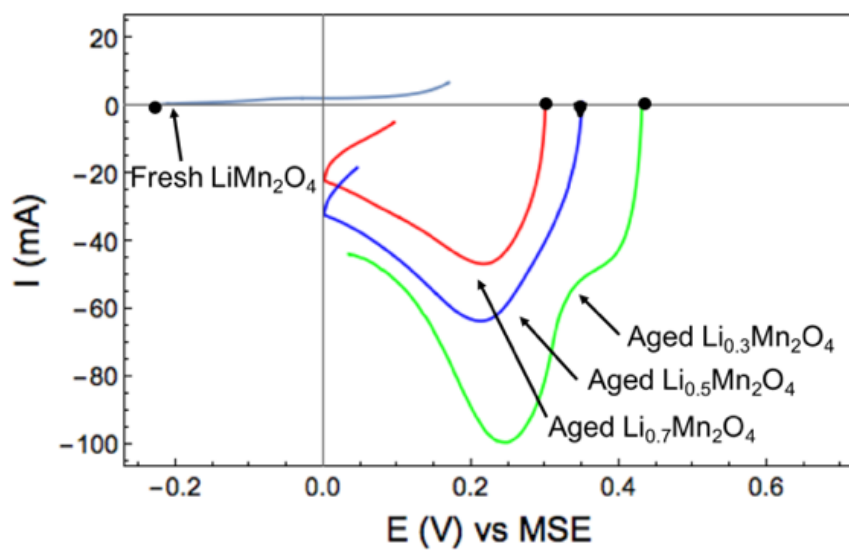


**Figure 8-5.** X-ray diffraction patterns of a) LMO-HT recycled from aged  $\text{Li}_{0.7}\text{Mn}_2\text{O}_4$  through different hydrothermal recycling conditions, b) and c) Fitting of peaks of impurity phases in LMO-HT samples in (a). Small blue dots are originally data points and solid lines are fitting line. ▲ and ● indicate peaks of impurity phases are present.

In order to investigate the effect of different hydrothermal process conditions on the recycled product, three process parameters (molar ratio of reactants, reaction temperature and reaction

time) were chosen and investigated. In Figure 8-5 (a), LMO-HT samples with recycling condition LMO:LiOH=1:1 do not show any peaks of impurity phases, while LMO-HT samples with recycling condition LMO:LiOH=10:1 and 1:10 show peaks of impurity phases but at different  $2\theta$ . Figure 8-5 (b-c) show enlarged image of peaks of impurity phases. The solid lines are the fitting of raw data points and they match with raw data points, which suggests the existence of these peaks of impurity phases.

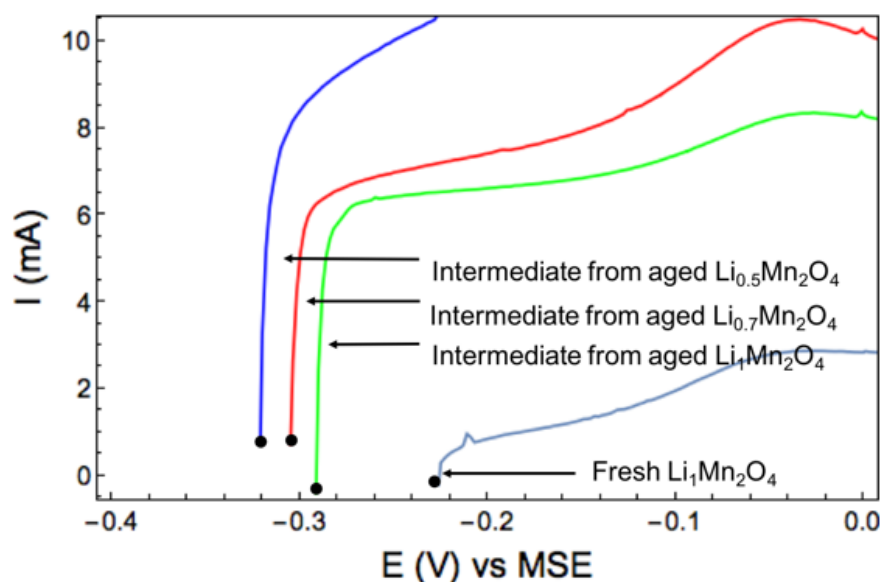
### 8.3.4 Electrochemical Results



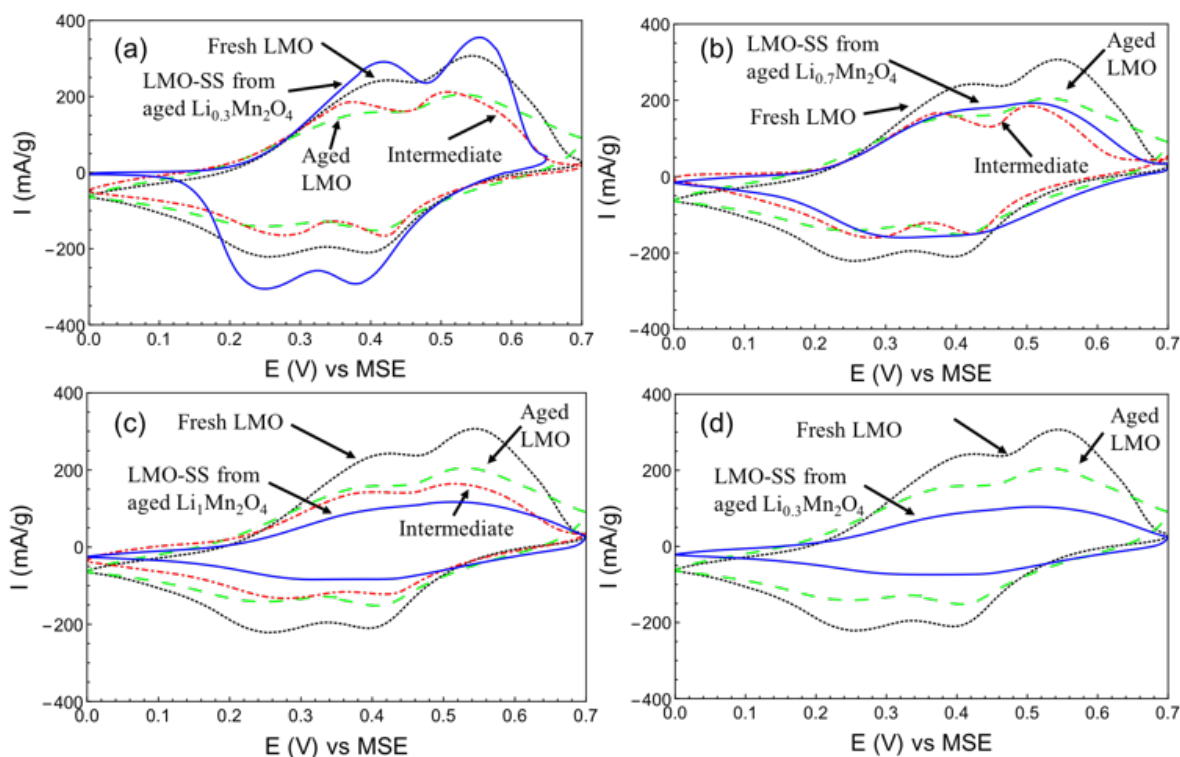
**Figure 8-6.** OCV of fresh LMO and aged LMO with different SoC using electrochemical titration. The black dot is OCV point.

Figure 8-6 shows open circuit voltage (OCV) of the fresh LMO and the aged LMO with different SoC. The aged LMO with higher SoC has higher OCV versus MSE. Figure 8-7 shows the OCV of the intermediate product of LMO-SS. The OCV of the intermediate products is closer to the OCV of the fresh LMO than the aged LMO with different SoC in Figure 8-6.

In Figure 8-8, compared with fresh LMO, all LMO-SS samples, and its intermediate samples show lower peak current density other than LMO-SS from aged  $\text{Li}_{0.3}\text{Mn}_2\text{O}_4$  in Figure 8-8 (a). With decreasing of aged LMO SoC, the peak current densities of LMO-SS in CV decrease and CV peak shape of LMO-SS changes from typical twin-peak to one broad peak, as shown in Figure 8 a-c. The peak current density of LMO-SS becomes relatively lower than its intermediate product as aged LMO SoC decreases, as shown in Figure 8 (a-c).



**Figure 8-7.** OCV of fresh LMO and intermediate product of LMO-SS from aged LMO with different SoC. The black dot is OCV point.



**Figure 8-8.** Cyclic voltammetry comparison between fresh LMO, aged LMO, intermediate product and final recycled product LMO-SS with washing between two steps of heat-treatments from a) aged  $\text{Li}_{0.3}\text{Mn}_2\text{O}_4$ , b) aged  $\text{Li}_{0.7}\text{Mn}_2\text{O}_4$ , c) aged  $\text{LiMn}_2\text{O}_4$ , d) aged  $\text{Li}_{0.3}\text{Mn}_2\text{O}_4$  without the wash in between two steps of heat-treatments.

In Figure 8-9, compared with fresh LMO and aged LMO, both LMO-HT samples show higher peak current densities than aged LMO and relatively the same peak current densities as fresh LMO. They both show typical twin-peak shape curve.

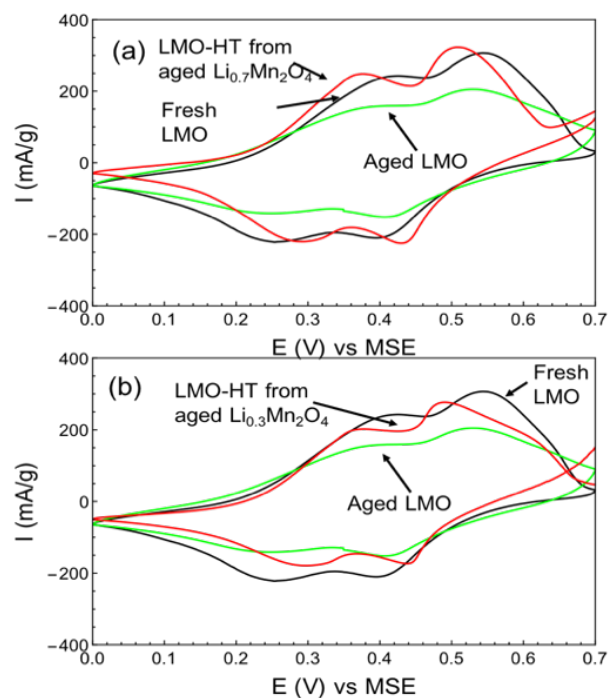


**Figure 8-9.** Cyclic voltammetry comparison between fresh LMO, aged LMO and LMO-HT(1:1, 165°C, 24hrs) from a) aged  $\text{Li}_{0.7}\text{Mn}_2\text{O}_4$  and b) aged  $\text{Li}_{0.3}\text{Mn}_2\text{O}_4$ .

In Table 8-3, the second oxidation peak height of the second cycle in CV (after normalized by active materials mass) is used as an indicator of capacity. The ratios of second oxidation peak height of LMO-HT to that of fresh LMO are listed. The peak current density of LMO-HT samples with LMO:LiOH=1:1 shows similar or higher height than fresh LMO while peak current density of the LMO-HT samples with LMO: LiOH=1:10 and 10:1 is smaller than that of fresh LMO. Within the condition LMO:LiOH=1:1, the LMO-HAT samples with different reaction time and reaction temperature show relatively the same peak intensity.

Table 8-3. Second oxidation peak intensity ratio in CV of LMO-HT to fresh LMO					
$I/I_o$	LMO:LiOH=10:1	LMO:LiOH=1:1		LMO:LiOH=1:10	
	24hr	12hr	24hr	48hr	24hr
145°C	0.87		1.07		
165°C	0.69	1.10	1.04	0.99	0.46
185°C			1.02		0.39

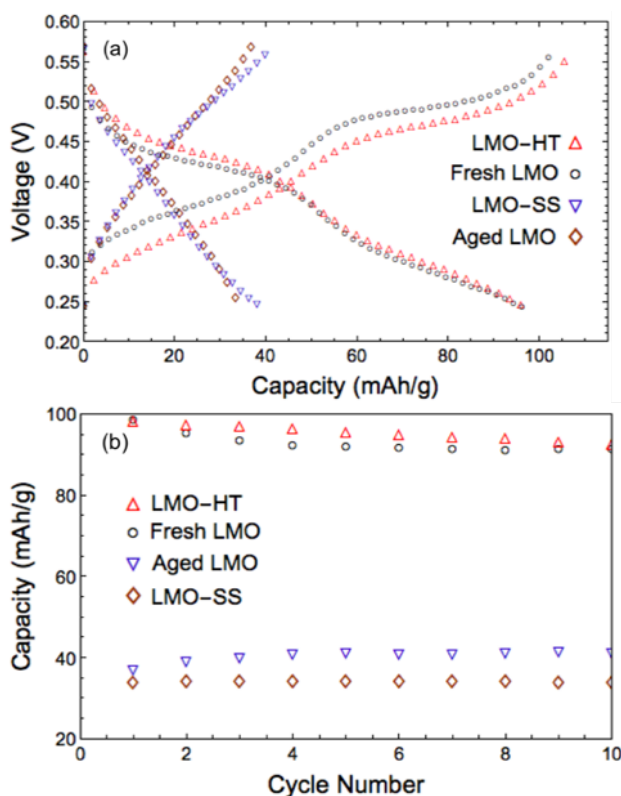


**Figure 8-10.** Comparison of a) cathode charge-discharge curve of 2<sup>nd</sup> cycle with +0.24 V to +0.57 V at a C/6 rate and b) discharge capacity vs cycle number for the first 10 cycles of fresh LMO, aged LMO, LMO-SS with washing in between two steps of heat-treatments from aged  $\text{Li}_{0.7}\text{Mn}_2\text{O}_4$  and LMO-HT(1:1, 165°C, 24hr) from aged  $\text{Li}_{0.7}\text{Mn}_2\text{O}_4$

Figure 8-10 shows the GCPL result tested in the full cell. LMO-HT(1:1, 165°C, 24hr) from aged  $\text{Li}_{0.7}\text{Mn}_2\text{O}_4$  shows relative the same electrochemical capacity as fresh LMO while the LMO-SS

sample with washing in between two steps of heat-treatments from aged  $\text{Li}_{0.7}\text{Mn}_2\text{O}_4$  shows no improvement in electrochemical capacity when compared with aged LMO.

## 8.4 Discussion

We will first compare the recycled products from both the solid-state method and the hydrothermal method and the effect of SoC in both cases, followed by detailed discussion of recycled products from the two methods separately.

### 8.4.1 Comparison between solid-state method and hydrothermal method

For the solid-state method, the quality of LMO-SS, including phase purity and electrochemical capacity, is hard to control due to the requirement for a stoichiometrically balanced ratio of LiOH to the aged LMO with different SoC. In order to avoid impure phase or loss of electrochemical capacity of LMO-SS, the stoichiometry of intermediate product needs to be close to  $\text{LiMn}_2\text{O}_4$  before high-temperature process. Otherwise, if the intermediate product of LMO-SS is over-lithiated or under-lithiated, it is not stable at high temperature, leading to the impure phase and loss of electrochemical capacity. To have the intermediate product with  $\text{LiMn}_2\text{O}_4$  stoichiometry, the ratio of LiOH to the aged LMO has to be adjusted based on SoC of the aged LMO. There is, however, a significant challenge in accurately determining the lithium content in aged LMO, which is hard to measure even if the battery was fully discharged before tear-down. Therefore, it is hard to get recycled LMO through a solid-state method without the impure phase and with similar electrochemical performance to the fresh LMO.

For the hydrothermally processed materials, the quality of the recycled product, including phase purity and electrochemical capacity, was easier to control compared to the solid-state method.

The hydrothermally recycled products from aged LMO with different SoC suggested that SoC of the aged LMO didn't have an obvious effect on recycled products and they showed similar electrochemical performance to the fresh LMO. The results of hydrothermally recycled at different process parameters indicate that the quality of the recycled product is influenced most by the molar ratio of reactants, and less so by reaction temperature and reaction time.

The sensitivity difference between the two processes, we think, results from the two causes: thermal activation and amount of accessible lithium source during the reaction. The reaction activation temperature is higher in solid-state method than in hydrothermal method. Therefore, the higher temperature process in solid-state method provides activation energy for decomposition reaction of LMO when the LMO is over-lithiated or under-lithiated while the activation temperature of the hydrothermal process is not enough to trigger the decomposition reaction even if when the LMO is over-lithiated or under-lithiated. As for the accessible lithium source, given the same ratio of the aged LMO to lithium source, the amount of accessible lithium source to the aged LMO is higher in hydrothermal reaction than in solid-state reaction due to the nature of solid-liquid and solid-solid mixture. While the aged LMO in solid-state reaction has only access to inhomogeneously distributed lithium resource nearby, the aged LMO in hydrothermal reaction has access to the whole lithium source solution. Therefore, it is easier for lithium to diffuse into the spinel structure of the aged LMO during the hydrothermal reaction to support the structure before the collapse of the spinel structure.



#### 8.4.2 Results from the solid-state reaction method

In Figure 8-8 (a-c), the peak current density and shape of CV curve of intermediate products of LMO-SS recycled from aged LMO with different SoC are relative the same compared with aged LMO other than the one from aged  $\text{Li}_1\text{Mn}_2\text{O}_4$  in Figure 8 (c). Moreover, in Figure 8-7, the OCV of these intermediate products is closer to that of fresh LMO compared with before the first heat-treatment in Figure 8-6. Both pieces of evidence suggest that during the first heat-treatment, lithium ions diffuse into spinel structure while the spinel structure remains stable.

By comparing LMO-SS samples recycled from the aged LMO with different SoC in Figure 8-8 a-c, we can see that the peak current density of LMO-SS decreases as the SoC of the aged LMO decreases. The reason behind this, we think, is that at a given ratio of the aged LMO and lithium source, the level of recycled LMO over-lithiation increases as the resident lithium content in the aged LMO increases. The over-lithiated LMO is not stable during high-temperature processing and the stability decreases as the level of LMO over-lithiation increases. The over-lithiated LMO decomposes by following reaction:  $\text{Li}_{1+x}\text{Mn}_{2-x}\text{O}_4 \rightarrow z \text{Li}_2\text{MnO}_3 + (1-z) \text{Li}_{1+y}\text{Mn}_{2-y}\text{O}_4 + z/2 \text{O}_2$ , where  $y=(x-z)/(1-z)$ .<sup>99-100</sup> Since  $\text{Li}_2\text{MnO}_3$  is not electrochemically-active in voltage range below 0.8V vs MSE,<sup>101</sup> the more  $\text{Li}_2\text{MnO}_3$ , the lower the peak current density is, as the trend shown in Figure 8-8. Based on the XRD pattern, the impurity after solid-state recycling process is identified as  $\text{Li}_2\text{MnO}_3$ . However, the quantity of this impurity can't be calculated at this point.

We can also see that the twin-peak shape curve of LMO-SS in CV changes to one broad peak gradually as SoC of aged LMO decreases. The reason for this phenomenon is that additional Li ions in  $\text{Li}_{1+x}\text{Mn}_{2-x}\text{O}_4$  replace Mn ions on 16d site in a spinel structure, which discourages order-disorder phase transition by Li ions on 8a sites. As a result, the twin-peak shape diminishes into

one broad peak with increasing  $x$ .<sup>102</sup> The lower the SoC of aged LMO is, the larger  $x$  is in the  $\text{Li}_{1+x}\text{Mn}_{2-x}\text{O}_4$  for LMO-SS and the more broad peak in the CV plot due to the change of structure. The above reasoning could be examined by the extreme case with no washing between two steps of heat-treatments. In this case, extra lithium source wasn't washed away after the first heat-treatment. The aged LMO got over-lithiated during heat treatment and decomposed into  $\text{Li}_2\text{MnO}_3$  during the second heat treatment as indicated by the peaks of impure phases in Figure 8-3 (b). This sample shows the lowest peak current density and broad peak shape compared with the other LMO-SS samples as shown in Figure 8-8.

#### 8.4.3 Results from hydrothermal reaction method

In Figure 8-9, both LMO-HT(1:1, 165°C, 24hrs) samples recycled from the aged LMO with different SoC show higher peak current density than the aged LMO and twin-peak shape curve. The results suggest that under this reaction condition, the hydrothermally recycled products don't show any sign of over-lithiation as in LMO-SS and SoC of the aged LMO doesn't have an obvious effect on the LMO-HT as for LMO-SS.

As for the effect on three process parameters, the impure phase peaks appear in LMO-HT with the molar ratio of LMO to LiOH at 1:10 and at 10:1 as shown in Figure 8-5 (a). For LMO-HT with LMO:LiOH=1:10 in Figure 8-5 (c), a high concentration of LiOH could introduce impurity  $\text{Li}_2\text{MnO}_3$  during hydrothermal reaction when synthesizing  $\text{LiMn}_2\text{O}_4$  according to the previous report.<sup>103-104</sup> For LMO-HT with LMO:LiOH=10:1 in Figure 8-5 (b), both samples show peaks of impure phases that are different from those in LMO-HT with LMO:LiOH=1:10. Although peaks of impure phases are hard to identify, it is likely that the peaks come from  $\text{Mn}_3\text{O}_4$ . As for

electrochemical performance, the peak current density ratios shown in Table 8-3 indicate that LMO-HT with LMO:LiOH=1:1 show relative the same peak intensity as fresh LMO, indicating that lost capacity of aged LMO can be recovered through hydrothermal method in this case while this is not the case for LMO-HT with LiOH:LiOH 10:1 and 1:10. Moreover, the SEM images in Figure 8-1 (a,c,d) suggest that it is likely that the flake-like and stick-like shape particles in LMO-HT with LMO:LiOH=10:1 could be the result of decomposition of LMO on the surface into manganese-oxide phase since the shape of these particles is quite different from the primary particle in the bulk materials.

The above-mentioned data show that the molar ratio of reactants is more important than reaction temperature and reaction time regarding recycled product phase purity and recovery of the lost electrochemical capacity of the aged LMO. The reason could be that for the LMO-HT with LiOH:LiOH 10:1 and 1:10, some of LMO transforms or decomposes to other phases. It is likely that these impure phases aren't electrochemical-active over the scanned voltage range.<sup>100, 103-105</sup>

#### 8.4.4 Aged LMO with different SoC

The peak shifting observed in the aged LMO with higher SoC to higher  $2\theta$  in Figure 8-2 indicates that some of the lithium ions are out from spinel structure, contracting the structure. In Figure 8-6 the aged LMO with higher SoC shows higher OCV. The results from XRD patterns and OCV confirm that the aged LMO with different SoC was created by electrochemical titration. The aged LMO with different SoC retains spinel structure and shows no sign of the peaks of impure phases based on Figure 8-2. Based on Figure 8-10, we can see that the electrochemical capacity of the aged LMO is lower than the fresh LMO, indicating that aged

LMO lost electrochemical capacity during long-term cycling. In term of Li recovery efficiency, we purposely completely discharged the battery prior to opening to get as much Li into the cathode as possible. With lower SoC, we discharged the battery more fully and have more Li get back into the cathode

## 8.5 Conclusion

Comparison between these two methods suggests that the hydrothermal method is better than solid-state regarding recycled product phase purity and electrochemical capacity. The solid-state method shows recovery of lost electrochemical capacity when the molar ratio of LiOH and aged LMO is well balanced based on SoC of the aged LMO. The hydrothermally recycled product can recover lost electrochemical capacity when the molar ratio of LiOH and aged LMO is 1:1 regardless of variation of reaction temperature, reaction time and SoC of the aged LMO.

The SoC of the aged LMO has different effects on recycled products from the two recycling methods. The recycled product from the solid-state method is sensitive to SoC of the aged LMO since the LMO-SS showed different electrochemical performance in CV when SoC of the aged LMO varied. In contrast, the SoC of the aged LMO doesn't have an obvious effect on the hydrothermally recycled product since the LMO-HT shows relatively the same electrochemical performance when SoC of the aged LMO varied. The different effect on SoC on the recycled product through two methods could lie in the different reaction activation temperature and accessible lithium source during the reaction. The results suggest that hydrothermal method is a more flexible method towards the aged LMO with different SoC than solid-state method.

This study points out that the property of aged cathode materials, such as SoC, could influence recycled product through direct recycling method depending on the method used. Therefore, it is important to pair the property of aged cathode with an appropriate direct recycling method to yield a recycled product with higher quality.

## Chapter 9. Summary and Future Work

In the body of this work, we set out to understand the cause of the difference in aged cathode materials properties under different cycling conditions, arising from both cell and materials levels. Through analysis of full cell cycling data and post-mortem characterization, we understand that for the same battery system, the cell capacity could end up be anode-limited or cathode-limited, depending on how the cell is cycled. This further leads to the difference in the degree of aging in cathode in these two cases. Moreover, the inhomogeneous aging in large format cells (compared to small cells, coin cell, often examined in academic labs), such as 18650 cells, can lead to variation in the aging level of cathode materials within one cell. So, it is clear that the cause of differences in cathode materials could range from cycling conditions to electrode inhomogeneity. This indicates that when it comes to practical application, it is unavoidable for the cathode recycling manufacturer to get aged cathode materials with different properties.

To overcome inconsistency in aged cathode materials, we investigate the effect of various direct recycling process parameters and its relationship with specific aged cathode properties, including the level of residual Lithium content, the thickness of SEI and the surface reconstruction layer. An optimized direct recycling process has been created which is capable of dealing with the difference in above-mentioned properties of cathode materials and producing the consistent recycled product.

For future work, several topics worth further investigation. Other aged cathode properties in layered cathode materials, including the dissolution of metal-ion and cracking, should be investigated to understand the effects of these properties on the recycled product and direct recycling process parameters that can address these differences to get the consistent recycled product. This would help the cathode direct recycling community have more a complete understanding of what we can/can't deal with in the aged cathode materials.

Another aspect is that nowadays, the evolution of new cathode materials is occurring rapidly. There is a huge demand for higher energy density Li-ion batteries, this trend will continue for a relatively long time. Under these circumstance, the recycled cathode materials via direct recycling, which is essentially putting it back to where it was when produced years ago, is likely to be outmoded in terms of capacity, stability, etc. As such, the recycled product is like to have advantage of lower cost based on the calculation of product cost and disadvantage of performance competitiveness as compared to the state of the art cathode materials. For example, the cathode materials that is ready for recycling long is  $\text{Li}(\text{Ni}_{0.33}\text{Co}_{0.33}\text{Mn}_{0.33})\text{O}_2$  (NCM111) while the up-to-date cathode materials is  $\text{Li}(\text{Ni}_{0.8}\text{Co}_{0.1}\text{Mn}_{0.1})\text{O}_2$  (NCM811). One interesting question we can ask is can we not only put the aged cathode back to where it was but also makes it better. In other words, can we directly recycle the aged NCM111 while simultaneously changing its composition to NCM811?

# Disclaimer

Sections of this document have been previously found in the following papers, either as is or reworked to fit the form of this thesis. Some of other published works that come from collaboration with other groups are also listed here, though not fitted the scope of this thesis.

- **Han Wang**, Sven Burke, Rui Yuan, Jay F. Whitacre " Direct recycling of cathode: from inhomogeneous aged cathode to consistent recycled product". **[first Author] [Draft Done]**

**(Chapter 7)**

- **Han Wang**, Jay F. Whitacre " Inhomogeneous aging of cathode materials in commercial 18650 lithium ion battery cells ." Journal of Energy Storage **[first Author] [Under review]**

**(Chapter 5)**

- Yuan, Rui, **Han Wang**, Mingkang Sun, Jay Whitacre, Krzysztof Matyjaszewski, and Tomasz Kowalewski. "Copolymer - Derived N/B Co - Doped Nanocarbons with Controlled Porosity and Highly Active Surface." Journal of Polymer Science 58, no. 1 (2020): 225-232. **[Co-first Author]**

- Li, Sipei, **Han Wang**, Julia Cuthbert, Tong Liu, Jay F. Whitacre, and Krzysztof Matyjaszewski. "A Semiliquid Lithium Metal Anode." Joule (2019). **[Co-first Author]**

- **Han Wang**, Frisco S, Gottlieb E, Yuan R, Whitacre JF. Capacity degradation in commercial Li-ion cells: The effects of charge protocol and temperature. Journal of Power Sources. 2019 Jun 30;426:67-73 **[First Author] (Chapter 4)**

- Yuan, Rui, **Han Wang**, Mingkang Sun, Krishnan Damodaran, Eric Gottlieb, Maciej Kopec, Karoline Eckhart et al. "Well-Defined N/S Co-Doped Nanocarbons from Sulfurized PAN-b-PBA



Block Copolymers: Structure and Supercapacitor Performance." ACS Applied Nano Materials (2019). [**Co-first Author**]

• Li, Sipei, **Han Wang**, Wei Wu, Francesca Lorandi, Jay F. Whitacre, and Krzysztof Matyjaszewski. "Solvent-Processed Metallic Lithium Microparticles for Lithium Metal Batteries." ACS Applied Energy Materials (2019). [**Co-first Author**]

• **Han Wang**, and Jay F. Whitacre. "Direct Recycling of Aged  $\text{LiMn}_2\text{O}_4$  Cathode Materials used in Aqueous Lithium-ion Batteries: Processes and Sensitivities." Energy Technology 6.12 (2018): 2429-2437. [**First Author**] (**Chapter 8**)

• Sipei Li, Alexander I Mohamed, Vikram Pande, **Han Wang**, Julia Cuthbert, Xiangcheng Pan, Hongkun He, Zongyu Wang, Venkatasubramanian Viswanathan, Jay F Whitacre, Krzysztof Matyjaszewski. "Single-Ion Homopolymer Electrolytes with High Transference Number Prepared by Click Chemistry and Photoinduced Metal-Free Atom-Transfer Radical Polymerization." ACS Energy Letters 3.1 (2017): 20-27. [**Second Author**]

# References

1. Wang, H.; Frisco, S.; Gottlieb, E.; Yuan, R.; Whitacre, J. F., Capacity degradation in commercial Li-ion cells: The effects of charge protocol and temperature. *J Power Sources* **2019**, *426*, 67-73.
2. Ciez, R. E.; Whitacre, J. F., Examining different recycling processes for lithium-ion batteries. *Nat Sustain* **2019**, *2* (2), 148-156.
3. Gaines, L.; Richa, K.; Spangenberg, J., Key issues for Li-ion battery recycling. *Mrs Energy Sustain* **2018**, *5*.
4. Gaines, L., Lithium-ion battery recycling processes: Research towards a sustainable course. *Sustain Mater Techno* **2018**, *17*.
5. Bernardes, A. M.; Espinosa, D. C. R.; Tenorio, J. A. S., Recycling of batteries: a review of current processes and technologies. *J Power Sources* **2004**, *130* (1-2), 291-298.
6. Georgi-Maschler, T.; Friedrich, B.; Weyhe, R.; Heegn, H.; Rutz, M., Development of a recycling process for Li-ion batteries. *J Power Sources* **2012**, *207*, 173-182.
7. Xu, J.; Thomas, H.; Francis, R. W.; Lum, K. R.; Wang, J.; Liang, B., A review of processes and technologies for the recycling of lithium-ion secondary batteries. *J Power Sources* **2008**, *177* (2), 512-527.
8. Ganter, M. J.; Landi, B. J.; Babbitt, C. W.; Anctil, A.; Gaustad, G., Cathode refunctionalization as a lithium ion battery recycling alternative. *J Power Sources* **2014**, *256*, 274-280.
9. Song, X.; Hu, T.; Liang, C.; Long, H.; Zhou, L.; Song, W.; You, L.; Wu, Z.; Liu, J., Direct regeneration of cathode materials from spent lithium iron phosphate batteries using a solid phase sintering method. *RSC Advances* **2017**, *7* (8), 4783-4790.
10. Sita, L. E.; da Silva, S. P.; da Silva, P. R. C.; Scarminio, J., Re-synthesis of LiCoO<sub>2</sub> extracted from spent Li-ion batteries with low and high state of health. *Materials Chemistry and Physics* **2017**, *194*, 97-104.
11. Zhang, Z.; He, W.; Li, G.; Xia, J.; Hu, H.; Huang, J.; Zhang, S., Recovery of lithium cobalt oxide material from the cathode of spent lithium-ion batteries. *ECS Electrochemistry Letters* **2014**, *3* (6), A58-A61.
12. Chen, S.; He, T.; Lu, Y.; Su, Y.; Tian, J.; Li, N.; Chen, G.; Bao, L.; Wu, F., Renovation of LiCoO<sub>2</sub> with outstanding cycling stability by thermal treatment with Li<sub>2</sub>CO<sub>3</sub> from spent Li-ion batteries. *Journal of Energy Storage* **2016**, *8*, 262-273.
13. Krueger, S.; Kloepsch, R.; Li, J.; Nowak, S.; Passerini, S.; Winter, M., How do reactions at the anode/electrolyte interface determine the cathode performance in lithium-ion batteries? *J Electrochem Soc* **2013**, *160* (4), A542-A548.
14. Zhang, S. S., The effect of the charging protocol on the cycle life of a Li-ion battery. *J Power Sources* **2006**, *161* (2), 1385-1391.
15. Waldmann, T.; Kasper, M.; Wohlfahrt-Mehrens, M., Optimization of Charging Strategy by Prevention of Lithium Deposition on Anodes in high-energy Lithium-ion Batteries - Electrochemical Experiments. *Electrochim Acta* **2015**, *178*, 525-532.
16. Wang, H.; Whitacre, J. F., Direct Recycling of Aged LiMn<sub>2</sub>O<sub>4</sub> Cathode Materials used in Aqueous Lithium-ion Batteries: Processes and Sensitivities. *Energy Technol-Ger.*
17. Xu, K., Electrolytes and Interphases in Li-Ion Batteries and Beyond. *Chemical Reviews* **2014**, *114* (23), 11503-11618.

18. Kim, J.; Hong, Y. S.; Ryu, K. S.; Kim, M. G.; Cho, J., Washing effect of a  $\text{LiNi}_{0.83}\text{Co}_{0.15}\text{Al}_{0.02}\text{O}_2$  cathode in water. *Electrochim Solid St* **2006**, 9 (1), A19-A23.
19. Xiong, X. H.; Wang, Z. X.; Yue, P.; Guo, H. J.; Wu, F. X.; Wang, J. X.; Li, X. H., Washing effects on electrochemical performance and storage characteristics of  $\text{LiNi}_{0.8}\text{Co}_{0.1}\text{Mn}_{0.1}\text{O}_2$  as cathode material for lithium-ion batteries. *J Power Sources* **2013**, 222, 318-325.
20. Verma, P.; Maire, P.; Novak, P., A review of the features and analyses of the solid electrolyte interphase in Li-ion batteries. *Electrochim Acta* **2010**, 55 (22), 6332-6341.
21. Lin, F.; Markus, I. M.; Doeffer, M. M.; Xin, H. L. L., Chemical and Structural Stability of Lithium-Ion Battery Electrode Materials under Electron Beam. *Sci Rep-Uk* **2014**, 4.
22. Myung, S. T.; Maglia, F.; Park, K. J.; Yoon, C. S.; Lamp, P.; Kim, S. J.; Sun, Y. K., Nickel-Rich Layered Cathode Materials for Automotive Lithium-Ion Batteries: Achievements and Perspectives. *Acs Energy Lett* **2017**, 2 (1), 196-223.
23. Zheng, J.; Yan, P.; Zhang, J.; Engelhard, M. H.; Zhu, Z.; Polzin, B. J.; Trask, S.; Xiao, J.; Wang, C.; Zhang, J., Suppressed oxygen extraction and degradation of  $\text{LiNi}_x\text{Mn}_y\text{Co}_z\text{O}_2$  cathodes at high charge cut-off voltages. *Nano Research* **2017**, 10 (12), 4221-4231.
24. Omar, N.; Daowd, M.; Bossche, P. v. d.; Hegazy, O.; Smekens, J.; Coosemans, T.; Mierlo, J. v., Rechargeable energy storage systems for plug-in hybrid electric vehicles—Assessment of electrical characteristics. *Energies* **2012**, 5 (8), 2952-2988.
25. Vetter, J.; Novak, P.; Wagner, M. R.; Veit, C.; Moller, K. C.; Besenhard, J. O.; Winter, M.; Wohlfahrt-Mehrens, M.; Vogler, C.; Hammouche, A., Ageing mechanisms in lithium-ion batteries. *J Power Sources* **2005**, 147 (1-2), 269-281.
26. Kabir, M. M.; Demirocak, D. E., Degradation mechanisms in Li-ion batteries: a state-of-the-art review. *International Journal of Energy Research* **2017**, 41 (14), 1963-1986.
27. Abarbanel, D.; Nelson, K.; Dahn, J., Exploring Impedance Growth in High Voltage NMC/Graphite Li-Ion Cells Using a Transmission Line Model. *J Electrochem Soc* **2016**, 163 (3), A522-A529.
28. Peled, E.; Golodnitsky, D.; Ardel, G., Advanced model for solid electrolyte interphase electrodes in liquid and polymer electrolytes. *J Electrochem Soc* **1997**, 144 (8), L208-L210.
29. Agubra, V.; Fergus, J., Lithium ion battery anode aging mechanisms. *Materials* **2013**, 6 (4), 1310-1325.
30. Broussely, M.; Biensan, P.; Bonhomme, F.; Blanchard, P.; Herreyre, S.; Nechev, K.; Staniewicz, R., Main aging mechanisms in Li ion batteries. *J Power Sources* **2005**, 146 (1-2), 90-96.
31. Waldmann, T.; Hogg, B. I.; Wohlfahrt-Mehrens, M., Li plating as unwanted side reaction in commercial Li-ion cells - A review. *J Power Sources* **2018**, 384, 107-124.
32. Liu, Q. Q.; Du, C. Y.; Shen, B.; Zuo, P. J.; Cheng, X. Q.; Ma, Y. L.; Yin, G. P.; Gao, Y. Z., Understanding undesirable anode lithium plating issues in lithium-ion batteries. *Rsc Advances* **2016**, 6 (91), 88683-88700.
33. Li, Z.; Huang, J.; Liaw, B. Y.; Metzler, V.; Zhang, J. B., A review of lithium deposition in lithium-ion and lithium metal secondary batteries. *J Power Sources* **2014**, 254, 168-182.
34. Petzl, M.; Kasper, M.; Danzer, M. A., Lithium plating in a commercial lithium-ion battery A low-temperature aging study. *J Power Sources* **2015**, 275, 799-807.
35. Burns, J. C.; Stevens, D. A.; Dahn, J. R., In-Situ Detection of Lithium Plating Using High Precision Coulometry. *J Electrochem Soc* **2015**, 162 (6), A959-A964.

36. Waldmann, T.; Hogg, B. I.; Kasper, M.; Grolleau, S.; Couceiro, C. G.; Trad, K.; Matadi, B. P.; Wohlfahrt-Mehrens, M., Interplay of Operational Parameters on Lithium Deposition in Lithium-Ion Cells: Systematic Measurements with Reconstructed 3-Electrode Pouch Full Cells. *J Electrochem Soc* **2016**, *163* (7), A1232-A1238.
37. Xiong, D.; Petibon, R.; Nie, M.; Ma, L.; Xia, J.; Dahn, J. R., Interactions between Positive and Negative Electrodes in Li-Ion Cells Operated at High Temperature and High Voltage. *J Electrochem Soc* **2016**, *163* (3), A546-A551.
38. Lu, D.; Xu, M.; Zhou, L.; Garsuch, A.; Lucht, B. L., Failure mechanism of graphite/LiNi<sub>0.5</sub>Mn<sub>1.5</sub>O<sub>4</sub> cells at high voltage and elevated temperature. *J Electrochem Soc* **2013**, *160* (5), A3138-A3143.
39. Browning, K. L.; Baggetto, L.; Unocic, R. R.; Dudney, N. J.; Veith, G. M., Gas evolution from cathode materials: A pathway to solvent decomposition concomitant to SEI formation. *J Power Sources* **2013**, *239*, 341-346.
40. Li, W.; Song, B.; Manthiram, A., High-voltage positive electrode materials for lithium-ion batteries. *Chemical Society Reviews* **2017**.
41. Norberg, N. S.; Lux, S. F.; Kostecki, R., Interfacial side-reactions at a LiNi<sub>0.5</sub>Mn<sub>1.5</sub>O<sub>4</sub> electrode in organic carbonate-based electrolytes. *Electrochemistry Communications* **2013**, *34*, 29-32.
42. MahootcheianAsl, N.; Kim, J.-H.; Pieczonka, N. P.; Liu, Z.; Kim, Y., Multilayer electrolyte cell: A new tool for identifying electrochemical performances of high voltage cathode materials. *Electrochemistry Communications* **2013**, *32*, 1-4.
43. Xiong, D.; Ellis, L.; Nelson, K.; Hynes, T.; Petibon, R.; Dahn, J., Rapid Impedance Growth and Gas Production at the Li-Ion Cell Positive Electrode in the Absence of a Negative Electrode. *J Electrochem Soc* **2016**, *163* (14), A3069-A3077.
44. Xiong, D.; Ellis, L.; Petibon, R.; Hynes, T.; Dahn, J., Studies of Gas Generation, Gas Consumption and Impedance Growth in Li-Ion Cells with Carbonate or Fluorinated Electrolytes Using the Pouch Bag Method. *J Electrochem Soc* **2017**, *164* (2), A340-A347.
45. Li, S.; Chen, C.; Xia, X.; Dahn, J., The impact of electrolyte oxidation products in LiNi<sub>0.5</sub>Mn<sub>1.5</sub>O<sub>4</sub>/Li<sub>4</sub>Ti<sub>5</sub>O<sub>12</sub> cells. *J Electrochem Soc* **2013**, *160* (9), A1524-A1528.
46. Joshi, T.; Eom, K.; Yushin, G.; Fuller, T. F., Effects of dissolved transition metals on the electrochemical performance and SEI growth in lithium-ion batteries. *J Electrochem Soc* **2014**, *161* (12), A1915-A1921.
47. Gilbert, J. A.; Shkrob, I. A.; Abraham, D. P., Transition metal dissolution, ion migration, electrocatalytic reduction and capacity loss in Lithium-ion full cells. *J Electrochem Soc* **2017**, *164* (2), A389-A399.
48. Pieczonka, N. P.; Liu, Z.; Lu, P.; Olson, K. L.; Moote, J.; Powell, B. R.; Kim, J.-H., Understanding transition-metal dissolution behavior in LiNi<sub>0.5</sub>Mn<sub>1.5</sub>O<sub>4</sub> high-voltage spinel for lithium ion batteries. *The Journal of Physical Chemistry C* **2013**, *117* (31), 15947-15957.
49. Burns, J.; Kassam, A.; Sinha, N.; Downie, L.; Solnickova, L.; Way, B.; Dahn, J., Predicting and extending the lifetime of Li-ion batteries. *J Electrochem Soc* **2013**, *160* (9), A1451-A1456.
50. Swain, B., Recovery and recycling of lithium: A review. *Separation and Purification Technology* **2017**, *172*, 388-403.
51. Sverdrup, H. U.; Ragnarsdottir, K. V.; Koca, D., Integrated Modelling of the Global Cobalt Extraction, Supply, Price and Depletion of Extractable Resources Using the WORLD6 Model. *BioPhysical Economics and Resource Quality* **2017**, *2* (1), 4.

52. Larcher, D.; Tarascon, J. M., Towards greener and more sustainable batteries for electrical energy storage. *Nat Chem* **2015**, 7 (1), 19-29.
53. Chagnes, A.; Pospiech, B., A brief review on hydrometallurgical technologies for recycling spent lithium-ion batteries. *Journal of Chemical Technology and Biotechnology* **2013**, 88 (7), 1191-1199.
54. Gratz, E.; Sa, Q.; Apelian, D.; Wang, Y., A closed loop process for recycling spent lithium ion batteries. *J Power Sources* **2014**, 262, 255-262.
55. Kim, D.-S.; Sohn, J.-S.; Lee, C.-K.; Lee, J.-H.; Han, K.-S.; Lee, Y.-I., Simultaneous separation and renovation of lithium cobalt oxide from the cathode of spent lithium ion rechargeable batteries. *J Power Sources* **2004**, 132 (1), 145-149.
56. Zhang, X.; Li, L.; Fan, E.; Xue, Q.; Bian, Y.; Wu, F.; Chen, R., Toward sustainable and systematic recycling of spent rechargeable batteries. *Chemical Society Reviews* **2018**, 47 (19), 7239-7302.
57. Zhan, R.; Oldenburg, Z.; Pan, L., Recovery of active cathode materials from lithium-ion batteries using froth flotation. *Sustain Mater Techno* **2018**, 17, e00062.
58. Bang, H. J.; Joachin, H.; Yang, H.; Amine, K.; Prakash, J., Contribution of the structural changes of  $\text{LiNi}_{0.8}\text{Co}_{0.15}\text{Al}_{0.05}\text{O}_2$  cathodes on the exothermic reactions in Li-ion cells. *J Electrochem Soc* **2006**, 153 (4), A731-A737.
59. Jung, S. K.; Gwon, H.; Hong, J.; Park, K. Y.; Seo, D. H.; Kim, H.; Hyun, J.; Yang, W.; Kang, K., Understanding the Degradation Mechanisms of  $\text{LiNi}_{0.5}\text{Co}_{0.2}\text{Mn}_{0.3}\text{O}_2$  Cathode Material in Lithium Ion Batteries. *Adv Energy Mater* **2014**, 4 (1).
60. Cherkashinin, G.; Motzko, M.; Schulz, N.; Späth, T.; Jaegermann, W., Electron spectroscopy study of Li [Ni, Co, Mn] O<sub>2</sub>/electrolyte interface: electronic structure, interface composition, and device implications. *Chem Mater* **2015**, 27 (8), 2875-2887.
61. Waldmann, T.; Wilka, M.; Kasper, M.; Fleischhammer, M.; Wohlfahrt-Mehrens, M., Temperature dependent ageing mechanisms in Lithium-ion batteries - A Post-Mortem study. *J Power Sources* **2014**, 262, 129-135.
62. Pinson, M. B.; Bazant, M. Z., Theory of SEI Formation in Rechargeable Batteries: Capacity Fade, Accelerated Aging and Lifetime Prediction. *J Electrochem Soc* **2013**, 160 (2), A243-A250.
63. Sloop, S. E.; Kerr, J. B.; Kinoshita, K., The role of Li-ion battery electrolyte reactivity in performance decline and self-discharge. *J Power Sources* **2003**, 119, 330-337.
64. Guéguen, A.; Streich, D.; He, M.; Mendez, M.; Chesneau, F. F.; Novák, P.; Berg, E. J., Decomposition of LiPF<sub>6</sub> in high energy lithium-ion batteries studied with online electrochemical mass spectrometry. *J Electrochem Soc* **2016**, 163 (6), A1095-A1100.
65. Wagner, R.; Korth, M.; Streipert, B.; Kasnatscheew, J.; Gallus, D. R.; Brox, S.; Amereller, M.; Cekic-Laskovic, I.; Winter, M., Impact of selected LiPF<sub>6</sub> hydrolysis products on the high voltage stability of lithium-ion battery cells. *ACS applied materials & interfaces* **2016**, 8 (45), 30871-30878.
66. Andersson, A.; Abraham, D.; Haasch, R.; MacLaren, S.; Liu, J.; Amine, K., Surface characterization of electrodes from high power lithium-ion batteries. *J Electrochem Soc* **2002**, 149 (10), A1358-A1369.
67. Yang, X.-G.; Leng, Y.; Zhang, G.; Ge, S.; Wang, C.-Y., Modeling of lithium plating induced aging of lithium-ion batteries: Transition from linear to nonlinear aging. *J Power Sources* **2017**, 360, 28-40.

68. Li, H. Y.; Liu, A. R.; Zhang, N.; Wang, Y. Q.; Yin, S.; Wu, H. H.; Dahn, J. R., An Unavoidable Challenge for Ni-Rich Positive Electrode Materials for Lithium-Ion Batteries. *Chem Mater* **2019**, *31* (18), 7574-7583.
69. Yan, P. F.; Nie, A. M.; Zheng, J. M.; Zhou, Y. G.; Lu, D. P.; Zhang, X. F.; Xu, R.; Belharouak, I.; Zu, X. T.; Xiao, J.; Amine, K.; Liu, J.; Gao, F.; Shahbazian-Yassar, R.; Zhang, J. G.; Wang, C. M., Evolution of Lattice Structure and Chemical Composition of the Surface Reconstruction Layer in  $\text{Li}_{1.2}\text{Ni}_{0.2}\text{Mn}_{0.6}\text{O}_2$  Cathode Material for Lithium Ion Batteries. *Nano Lett* **2015**, *15* (1), 514-522.
70. Bach, T. C.; Schuster, S. F.; Fleder, E.; Muller, J.; Brand, M. J.; Lormann, H.; Jossen, A.; Sextl, G., Nonlinear aging of cylindrical lithium-ion cells linked to heterogeneous compression. *Journal of Energy Storage* **2016**, *5*, 212-223.
71. Waldmann, T.; Gorse, S.; Samtleben, T.; Schneider, G.; Knoblauch, V.; Wohlfahrt-Mehrens, M., A Mechanical Aging Mechanism in Lithium-Ion Batteries. *J Electrochem Soc* **2014**, *161* (10), A1742-A1747.
72. Pfrang, A.; Kersys, A.; Kriston, A.; Sauer, D. U.; Rahe, C.; Kabitz, S.; Figgemeier, E., Long-term cycling induced jelly roll deformation in commercial 18650 cells. *J Power Sources* **2018**, *392*, 168-175.
73. Gelb, J.; Finegan, D. P.; Brett, D. J. L.; Shearing, P. R., Multi-scale 3D investigations of a commercial 18650 Li-ion battery with correlative electron- and X-ray microscopy. *J Power Sources* **2017**, *357*, 77-86.
74. Cannarella, J.; Arnold, C. B., Stress evolution and capacity fade in constrained lithium-ion pouch cells. *J Power Sources* **2014**, *245*, 745-751.
75. Cannarella, J.; Liu, X. Y.; Leng, C. Z.; Sinko, P. D.; Gor, G. Y.; Arnold, C. B., Mechanical Properties of a Battery Separator Under Compression and Tension. *J Electrochem Soc* **2014**, *161* (11), F3117-F3122.
76. Finegan, D. P.; Scheel, M.; Robinson, J. B.; Tjaden, B.; Hunt, I.; Mason, T. J.; Millichamp, J.; Di Michiel, M.; Offer, G. J.; Hinds, G.; Brett, D. J. L.; Shearing, P. R., In-operando high-speed tomography of lithium-ion batteries during thermal runaway. *Nat Commun* **2015**, *6*.
77. Zheng, J.; Ye, Y.; Liu, T.; Xiao, Y.; Wang, C.; Wang, F.; Pan, F., Ni/Li Disordering in Layered Transition Metal Oxide: Electrochemical Impact, Origin, and Control. *Accounts Chem Res* **2019**.
78. Duan, Y.; Yang, L.; Zhang, M.-J.; Chen, Z.; Bai, J.; Amine, K.; Pan, F.; Wang, F., Insights into Li/Ni ordering and surface reconstruction during synthesis of Ni-rich layered oxides. *J Mater Chem A* **2019**, *7* (2), 513-519.
79. Weidler, N.; Schuch, J.; Knaus, F.; Stenner, P.; Hoch, S.; Maljusch, A.; Schäfer, R.; Kaiser, B.; Jaegermann, W., X-ray Photoelectron Spectroscopic Investigation of Plasma-Enhanced Chemical Vapor Deposited  $\text{NiO}_x$ ,  $\text{NiO}_x(\text{OH})_y$ , and  $\text{CoNiO}_x(\text{OH})_y$ : Influence of the Chemical Composition on the Catalytic Activity for the Oxygen Evolution Reaction. *The Journal of Physical Chemistry C* **2017**, *121* (12), 6455-6463.
80. Andreu, N.; Flahaut, D.; Dedryvere, R.; Minvielle, M.; Martinez, H.; Gonbeau, D., XPS Investigation of Surface Reactivity of Electrode Materials: Effect of the Transition Metal. *Acs Applied Materials & Interfaces* **2015**, *7* (12), 6629-6636.
81. Li, H.; Li, J.; Zaker, N.; Zhang, N.; Botton, G.; Dahn, J., Synthesis of Single Crystal  $\text{LiNi}_{0.88}\text{Co}_{0.09}\text{Al}_{0.03}\text{O}_2$  with a Two-Step Lithiation Method. *J Electrochem Soc* **2019**, *166* (10), A1956-A1963.

82. Liu, H.; Yang, Y.; Zhang, J., Reaction mechanism and kinetics of lithium ion battery cathode material LiNiO<sub>2</sub> with CO<sub>2</sub>. *J Power Sources* **2007**, *173* (1), 556-561.
83. Huang, B.; Liu, D.; Qian, K.; Zhang, L.; Zhou, K.; Liu, Y.; Kang, F.; Li, B., A Simple Method for the Complete Performance Recovery of Degraded Ni-rich LiNi<sub>0.70</sub>Co<sub>0.15</sub>Mn<sub>0.15</sub>O<sub>2</sub> Cathode via Surface Reconstruction. *ACS applied materials & interfaces* **2019**, *11* (15), 14076-14084.
84. Liu, H.; Zhang, Z.; Gong, Z.; Yang, Y., Origin of deterioration for LiNiO<sub>2</sub> cathode material during storage in air. *Electrochemical and solid-state letters* **2004**, *7* (7), A190-A193.
85. Bang, H. J.; Joachin, H.; Yang, H.; Amine, K.; Prakash, J., Contribution of the structural changes of LiNi<sub>0.8</sub>Co<sub>0.15</sub>Al<sub>0.05</sub>O<sub>2</sub> cathodes on the exothermic reactions in Li-ion cells. *J Electrochem Soc* **2006**, *153* (4), A731-A737.
86. Belharouak, I.; Vissers, D.; Amine, K., Thermal stability of the Li(Ni<sub>0.8</sub>Co<sub>0.15</sub>Al<sub>0.05</sub>)O<sub>2</sub> cathode in the presence of cell components. *J Electrochem Soc* **2006**, *153* (11), A2030-A2035.
87. Li, H. Y.; Zhang, N.; Li, J.; Dahn, J. R., Updating the Structure and Electrochemistry of Li<sub>x</sub>NiO<sub>2</sub> for 0 ≤ x ≤ 1. *J Electrochem Soc* **2018**, *165* (13), A2985-A2993.
88. Shi, Y.; Zhang, M. H.; Meng, Y. S.; Chen, Z., Ambient-Pressure Relithiation of Degraded Li<sub>x</sub>Ni<sub>0.5</sub>Co<sub>0.2</sub>Mn<sub>0.3</sub>O<sub>2</sub> (0 < x < 1) via Eutectic Solutions for Direct Regeneration of Lithium-Ion Battery Cathodes. *Adv Energy Mater* **2019**, *9* (20).
89. Nayak, P. K.; Erickson, E. M.; Schipper, F.; Penki, T. R.; Munichandraiah, N.; Adelhelm, P.; Sclar, H.; Amalraj, F.; Markovsky, B.; Aurbach, D., Review on Challenges and Recent Advances in the Electrochemical Performance of High Capacity Li- and Mn-Rich Cathode Materials for Li-Ion Batteries. *Adv Energy Mater* **2018**, *8* (8).
90. Zheng, J. M.; Myeong, S. J.; Cho, W. R.; Yan, P. F.; Xiao, J.; Wang, C. M.; Cho, J.; Zhang, J. G., Li- and Mn-Rich Cathode Materials: Challenges to Commercialization. *Adv Energy Mater* **2017**, *7* (6).
91. Bak, S. M.; Nam, K. W.; Chang, W.; Yu, X. Q.; Hu, E. Y.; Hwang, S.; Stach, E. A.; Kim, K. B.; Chung, K. Y.; Yang, X. Q., Correlating Structural Changes and Gas Evolution during the Thermal Decomposition of Charged Li<sub>x</sub>Ni<sub>0.8</sub>Co<sub>0.15</sub>Al<sub>0.05</sub>O<sub>2</sub> Cathode Materials. *Chem Mater* **2013**, *25* (3), 337-351.
92. Mukherjee, P.; Faenza, N. V.; Pereira, N.; Ciston, J.; Piper, L. F. J.; Amatucci, G. G.; Cosandey, F., Surface Structural and Chemical Evolution of Layered LiNi<sub>0.8</sub>Co<sub>0.15</sub>Al<sub>0.05</sub>O<sub>2</sub> (NCA) under High Voltage and Elevated Temperature Conditions. *Chem Mater* **2018**, *30* (23), 8431-8445.
93. Zhang, M. J.; Teng, G. F.; Chen-Wiegart, Y. C. K.; Duan, Y. D.; Ko, J. Y. P.; Zheng, J. X.; Thieme, J.; Dooryhee, E.; Chen, Z. H.; Bai, J. M.; Amine, K.; Pan, F.; Wang, F., Cationic Ordering Coupled to Reconstruction of Basic Building Units during Synthesis of High-Ni Layered Oxides. *Journal of the American Chemical Society* **2018**, *140* (39), 12484-12492.
94. Wang, D. W.; Kou, R. H.; Ren, Y.; Sun, C. J.; Zhao, H.; Zhang, M. J.; Li, Y.; Huq, A.; Ko, J. Y. P.; Pan, F.; Sun, Y. K.; Yang, Y.; Amine, K.; Bai, J. M.; Chen, Z. H.; Wang, F., Synthetic Control of Kinetic Reaction Pathway and Cationic Ordering in High-Ni Layered Oxide Cathodes. *Advanced Materials* **2017**, *29* (39).
95. Li, J.; Zhang, N.; Li, H. Y.; Liu, A. R.; Wang, Y. Q.; Yin, S.; Wu, H. H.; Dahn, J. R., Impact of the Synthesis Conditions on the Performance of LiNi<sub>x</sub>CoyAlzO<sub>2</sub> with High Ni and Low Co Content. *J Electrochem Soc* **2018**, *165* (14), A3544-A3557.

96. Gauthier, M.; Carney, T. J.; Grimaud, A.; Giordano, L.; Pour, N.; Chang, H. H.; Fenning, D. P.; Lux, S. F.; Paschos, O.; Bauer, C.; Magia, F.; Lupart, S.; Lamp, P.; Shao-Horn, Y., Electrode-Electrolyte Interface in Li-Ion Batteries: Current Understanding and New Insights. *J Phys Chem Lett* **2015**, *6* (22), 4653-4672.
97. Whitacre, J.; Shanbhag, S.; Mohamed, A.; Polonsky, A.; Carlisle, K.; Gulakowski, J.; Wu, W.; Smith, C.; Cooney, L.; Blackwood, D., A polyionic, large-format energy storage device using an aqueous electrolyte and thick-format composite  $\text{NaTi}_2(\text{PO}_4)_3$ /activated carbon negative electrodes. *Energy Technol-Ger* **2015**, *3* (1), 20-31.
98. Yang, X.; Tang, W.; Kanoh, H.; Ooi, K., Synthesis of lithium manganese oxide in different lithium-containing fluxes. *Journal of Materials Chemistry* **1999**, *9* (10), 2683-2690.
99. Komaba, S.; Yabuuchi, N.; Ikemoto, S., High-temperature X-ray diffraction study of crystallization and phase segregation on spinel-type lithium manganese oxides. *J Solid State Chem* **2010**, *183* (1), 234-241.
100. Zhang, Y. C.; Wang, H.; Xu, H. Y.; Wang, B.; Yan, H.; Ahniyaz, A.; Yoshimura, M., Low-temperature hydrothermal synthesis of spinel-type lithium manganese oxide nanocrystallites. *Solid State Ionics* **2003**, *158* (1-2), 113-117.
101. Liu, G.; Zhang, S., One-step Synthesis of Low-cost and High Active  $\text{Li}_2\text{MnO}_3$  Cathode Materials. *INTERNATIONAL JOURNAL OF ELECTROCHEMICAL SCIENCE* **2016**, *11* (7), 5545-5551.
102. Gao, Y.; Reimers, J. N.; Dahn, J. R., Changes in the voltage profile of  $\text{Li}/\text{Li}_{1+x}\text{Mn}_{2-x}\text{O}_4$  cells as a function of x. *Phys Rev B* **1996**, *54* (6), 3878-3883.
103. Jiang, C.; Dou, S.; Liu, H.-K.; Ichihara, M.; Zhou, H., Synthesis of spinel  $\text{LiMn}_2\text{O}_4$  nanoparticles through one-step hydrothermal reaction. *J Power Sources* **2007**, *172* (1), 410-415.
104. Kanasaku, T.; Amezawa, K.; Yamamoto, N., Hydrothermal synthesis and electrochemical properties of Li-Mn-spinel. *Solid State Ionics* **2000**, *133* (1-2), 51-56.
105. Wu, H. M.; Tu, J. P.; Yuan, Y. F.; Chen, X. T.; Xiang, J. Y.; Zhao, X. B.; Cao, G. S., One-step synthesis  $\text{LiMn}_2\text{O}_4$  cathode by a hydrothermal method. *J Power Sources* **2006**, *161* (2), 1260-1263.